Modeling Nonlinear Optical Response in 2D Materials from Nonequilibrium Quantum Dynamics

DISSERTATION ZUR
ERLANGUNG DES DOKTORGRADES
AN DER FAKULTÄT FÜR MATHEMATIK, INFORMATIK UND
NATURWISSENSCHAFTEN, FACHBEREICH PHYSIK,
DER UNIVERSITÄT HAMBURG

WENWEN MAO

(Universität Hamburg)

HAMBURG
2024

Gutachter/innen der Dissertation:	Prof. Dr. Angel Rubio Prof. Dr. Alexander Lichtenstein
Zusammensetzung der Prüfungskommission:	Prof. Dr. Angel Rubio Prof. Dr. Alexander Lichtchstein Auß. Prof. Dr. Shunsuke A. Sato Prof. Dr. Peter Schmelcher Prof. Dr. Henning Moritz
Vorsitzende/r der Prüfungskommission:	Prof. Dr. Peter Schmelcher
Datum der Disputation:	04.09.2024
Vorsitzender Fach-Promotionsausschusses Physik:	Prof. Dr. Markus Drescher
Leiter des Fachbereichs Physik:	Prof. Dr. Wolfgang J. Parak
Dekan der Fakultät MIN:	Prof. Dr. -Ing. Norbert Ritter

Eidesstattliche Versicherung / Declaration on oath

Hiermit versichere ich an Eides statt, die vorliegende Dissertationsschrift selbst verfasst und keine anderen als die angegebenen Hilfsmittel und Quellen benutzt zu haben.
Sofern im Zuge der Erstellung der vorliegenden Dissertationsschrift generative Künstliche Intelligenz (gKI) basierte elektronische Hilfsmittel verwendet wurden, versichere ich, dass meine eigene Leistung im Vordergrund stand und dass eine vollständige Dokumentation aller verwendeten Hilfsmittel gemäß der Guten wissenschaftlichen Praxis vorliegt. Ich trage die Verantwortung für eventuell durch die gKI generierte fehlerhafte oder verzerrte Inhalte, fehlerhafte Referenzen, Verstöße gegen das Datenschutz- und Urheberrecht oder Plagiate.

Wenwen Mao
August 1, 2024

This page is intentionally left blank.

Acknowledgements

Completing this thesis and attaining my PhD would have been impossible without the tremendous support of numerous individuals, whose guidance, encouragement, and patience have been invaluable to me.

First and foremost, I extend my deepest appreciation to Prof. Dr. Angel Rubio for his exceptional supervision and unwavering patience throughout my doctoral journey. His passion for research and compassionate approach to mentorship not only enriched my scientific understanding but also left a profound impact on my approach to life. I am equally grateful to my co-supervisor Prof. Dr. Shunsuke Sato for his remarkable guidance and close mentorship. Prof. Sato's extraordinary physical intuition has continually astonished me, and many ideas within this thesis are a testament to his profound influence. His patience and steadfast support during challenging moments were instrumental in my journey to completing my PhD. I am profoundly grateful to my supervisors, for their unwavering support, invaluable guidance, and insightful feedback throughout every stage of this research endeavor. Their expertise and encouragement have been instrumental in shaping this thesis. I am especially grateful for his invaluable assistance during the final stages of thesis writing.

I am indebted to the experimental cooperators Prof.Hideki Hirori and Dr. Kotaro Nakagawa from Kyoto University for his insightful discussions and suggestions during the HHG spectra project, which greatly enriched my understanding of the subject. Their proficiency in nonlinear opotical spectspecific specific experimental technique or methodology was instrumental in obtaining crucial data and insights. Special thanks are due to Prof. Dr. Kazuhiro Yabana for his invaluable insights and discussions, the visiting during my travels in Yabana's group in Tsukuba University, Japan provided cherished memories. Also thanks Prof. Peizhen Tang and Prof. Shin Dongbin for their detailed guidance and thank them for their explanation, support and guidance in the solid systems' computing techniques.

I am grateful to the staff and resources of Max Planck Institute for the Structure and Dynamics of Matter (MPSD), whose facilities and assistance have facilitated the smooth progress of my research. Also to training opportunities from the International Max Planck Research School for Ultrafast Imaging & Structural

Dynamics (IMPRS) fellowship.

To all my friends and colleagues who have supported and encouraged me along this journey, I extend my heartfelt gratitude. Your camaraderie and friendship have been a source of strength and inspiration. Above all, I owe an immense debt of gratitude to my family for their unwavering support and love throughout the years of my PhD. Their care and encouragement sustained me through the challenges, and I am forever grateful for their presence in my life.

Contents

Abstract

Modeling Nonlinear Optical Response in 2D Materials from Nonequilibrium Quantum Dynamics

by

Wenwen Mao

der Fakultät für Mathematik, Informatik und Naturwissenschaften, Fachbereich Physik
Universität Hamburg

This thesis investigates the nonlinear optical response in 2D materials through a comprehensive examination of nonequilibrium quantum dynamics with in house developed tight binding model able to capture electron dynamics of open quantum systems. The first study explores the injection of nonlinear current in monolayer hexagonal boron nitride under two-color linearly-polarized laser fields, unveiling the breakdown of time-reversal symmetry and the emergence of ballistic current by solving time-dependent Schrödinger equation. In the second investigation, terahertz-induced high-order harmonic generation (HHG) and nonlinear electric transport in graphene are scrutinized, revealing the accurate modeling of electron dynamics through a nonequilibrium steady-state approach. Additionally, the third work delves into the enhancement of HHG in graphene by mid-infrared and terahertz fields with a joined theoretical and experiemntal study, attributing the phenomenon to a coherent coupling between MIR- and THz-induced transitions. We stress the validity of the theoretical framework developed in this thesis in the analysis of nonlinear optical phenomena in materials, especially in microscopic pictures and dissipative non-equilibrium analysis; opening a new way for theoretical prediction. By synthesizing these findings, this thesis advances our understanding of nonlinear optical phenomena in 2D materials and underscores the significance of nonequilibrium quantum dynamics in modeling such intricate behaviors. Further extensions of this work to other low dimensional phenomena in quantum materials are also highlighted in this report.

This page is intentionally left blank.

Abstraktum

Diese Dissertation untersucht die nichtlineare optische Reaktion in 2D-Materialien durch eine umfassende Untersuchung der Nichtgleichgewichtsquantendynamik mit einem intern entwickelten Tight-Binding Modell, das in der Lage ist, die Elektronendynamik offener Quantensysteme zu erfassen. Die erste Studie untersucht die Injektion von nichtlinearem Strom in einschichtiges hexagonales Bornitrid unter zweifarbigen linear polarisierten Laserfeldern und zeigt den Zusammenbruch der Zeitumkehrsymmetrie und die Entstehung ballistischen Stroms durch Lösung der zeitabhängigen Schrödinger-Gleichung. Die zweite Untersuchung befasst sich mit der Terahertz-induzierten Erzeugung von Harmonischen höherer Ordnung (HHG) und dem nichtlinearen elektrischen Transport in Graphen und zeigt die genaue Modellierung der Elektronendynamik durch einen Nichtgleichgewichts-Steady-State-Ansatz. Darüber hinaus befasst sich die dritte Arbeit mit der Verbesserung von HHG in Graphen durch mittlere Infrarot- und Terahertz-Felder mit einer gemeinsamen theoretischen und experimentellen Studie, die das Phänomen auf eine kohärente Kopplung zwischen MIR- und THz-induzierten Übergängen zurückführt. Wir betonen die Gültigkeit des in dieser Arbeit entwickelten theoretischen Rahmens bei der Analyse nichtlinearer optischer Phänomene in Materialien, insbesondere in mikroskopischen Theorien und dissipativer Nichtgleichgewichtsanalyse, die einen neuen Weg für theoretische Vorhersagen eröffnen. Durch die Synthese dieser Erkenntnisse erweitert diese Arbeit unser Verständnis nichtlinearer optischer Phänomene in 2D-Materialien und unterstreicht die Bedeutung der Nichtgleichgewichtsquantendynamik bei der Modellierung solch komplexer Verhaltensweisen. Weitere Erweiterungen dieser Arbeit auf andere niederdimensionale Phänomene in Quantenmaterialien werden in diesem Bericht ebenfalls hervorgehoben.

This page is intentionally left blank.

List of Figures

List of Publications

- **Wenwen Mao**, Angel Rubio, Shunsuke A. Sato. Nonlinear current injection in hexagonal boron nitride using linearly polarized light in a deeply off-resonant regime. (2024) *Advanced Optical Materials, p. 2400651*
- **Wenwen Mao**, Angel Rubio, Shunsuke A. Sato. Enhancement of high-order harmonic generation in graphene by mid-infrared and terahertz fields. (2024) *Phys. Rev. B* 109 (4), 045421
- Kotaro Nakagawa, **Wenwen Mao**, Shunsuke A. Sato, Hideki Hirori, Hot electron effect on high order harmonic generation from graphene modulated by THz electric pulse fields. (2024) *APL Photonics 9, 076107*
- **Wenwen Mao**, Angel Rubio, Shunsuke A. Sato. THz-induced high-order harmonic generation and nonlinear transport in graphene. (2022) *Phys. Rev. B* **106**, 024313
- Ofer Neufeld, **Wenwen Mao**, Hannes Hübener, Nicolas Tancogne-Dejean, Shunsuke A. Sato, Umberto De Giovannini, and Angel Rubio. Time- and angle-resolved photoelectron spectroscopy of strong-field light-dressed solids: Prevalence of the adiabatic band picture. (2022) *Phys. Rev. Research* **4**, 033101

This page is intentionally left blank.

List of Abbreviations

h-BN	Hexagonal boron nitride. 11–14, 33, 38, 101
HHG	High-Order Harmonic Generation. 1, 6, 7, 21, 58–60, 67, 73, 79–84, 91
LCAO	Linear Combination of Atomic Orbitals. 15
QuI	Quantum Interference. 5, 35
QuIC	Quantum Interference Control. 37, 38, 44–46, 48, 51, 53
SBE	Semiconductor Bloch equations. 9
TDDFT	Time-dependent Density-functional Theory. 9, 104, 105
TDSE	Time-dependent Schrödinger equation. 8, 9, 20, 21, 28, 38, 59, 60

This page is intentionally left blank.

Chapter 1

INTRODUCTION

In the conventional understanding of linear optics, the response of a material to an incident electromagnetic wave is linearly proportional to the strength of the electric field. However, when the intensity of the incident light becomes strong enough, the nonlinear optical response becomes significant. This regime reveals a rich variety of phenomena, including the photoncarrier injection, phase modulation, and harmonic generation. After the first observation of nonlinear optical phenomena by Franken [1], based on recent advancements in laser technology, groundbreaking research in the field of nonlinear optics have been driven [2–4], have conducted in a new era of intense light generation. These developments have paved the way for in-depth exploration of light-matter interactions in highly nonlinear regimes both in atomic and condensed matter phases. One of the most captivating nonlinear optical phenomena made accessible by these advances is High-order Harmonic Generation (HHG), a process characterized by its extreme photon upconversion and remarkable nonlinear characteristics.

This thesis aims to provide a comprehensive overview of the nonlinear response phenomenons including photocarrier injection and high-order harmonic generation from a theoretical point of view linked to the microscopic modeling of the electron dynamics in those 2D quantum materials. We will explore the theoretical foundations of light induced time-dependent quantum dynamics evolution in solid systems, including the quantum mechanical description of the light-matter ineraction process and the role of excited electron dynamics. By investigating photocarrier injection and HHG, we seek to deepen our understanding of

the nonlinear optical response of materials and unlock the potential for applications in fields such as ultrafast spectroscopy, attosecond science, and advanced imaging techniques.

1.1 Nonlinear Optical Response

In studies of optical response theory within solid systems, the dielectric function serves as an centered concept, the dielectric function characterizes how the material's polarization, induced by the external field, evolves with the field's frequency and intensity. Mathematically, the dielectric function connects the material's polarization density to the electric field through Maxwell's equations, forming the basis for understanding its optical properties. Linear response theory, predicated on the assumption of weak perturbations, asserts that the induced polarization is directly proportional to the strength of the applied field. Linear response theory is most applicable when the perturbations are weak. In other words, the system's behavior is approximately linear in the vicinity of its equilibrium or initial state. In such cases. the system's behavior is described by linear susceptibility ($\chi^{(1)}$).

The electric susceptibility ($\chi^{(1)}$) describes the response of a material to an applied electric field (**E**). The relationship between the induced polarization (**P**) and the applied electric field can be expressed as:

$$\mathbf{P^{(1)}}(\mathbf{t}) = \epsilon_0 \int_0^\infty \mathbf{R}^{(1)} \cdot \mathbf{E}(t-\tau) d\tau \tag{1.1}$$

Where:

- **P** is the induced polarization vector,
- $\mathbf{R}^{(1)}$ is the linear response function, electric susceptibility tensor, and
- **E** is the applied electric field vector.

Equation. (1.1) can be transformed to the frequency domain by intoducing the Fourier trasnform of electric field:

$$E(\omega) = \int_{-\infty'}^{\infty} E(t) \cdot e^{i\omega t} dt.$$

$$E(t) = \frac{1}{2\pi}\int_{-\infty'}^{\infty} E(\omega)\cdot e^{-i\omega t}d\omega.$$

By introducing above Fourier transform, we have:

$$\mathbf{P}^{(1)}(t) = \epsilon_0 \int_{-\infty}^{\infty}\frac{d\omega}{2\pi}\int_{0}^{\infty}\mathbf{R}^{(1)}e^{i\omega\tau}\cdot\mathbf{E}(\omega)e^{-i\omega t}d\tau$$

we intoduce an explicit expression for the linear susceptibility is:

$$\chi^{(1)}(\omega;\omega) = \int_{0}^{\infty}\mathbf{R}^{(1)}(\tau)\cdot e^{i\omega\tau}d\tau.$$

By noting that the equality must be maintained for each frequency ω, we recover the usual frequency domain description of linear response:

$$\mathbf{P}^{(1)}(\omega) = \epsilon_0\chi^{(1)}(\omega;\omega)\cdot\mathbf{E}(\omega) \tag{1.2}$$

In nonlinear response, the relationship can be described by analogous procedures. We can express the nonlinear polarization $P_i(t)$ as a convolution integral involving the electric field $E_j(t)$ and the time-dependent response function $\chi^{(2)}_{ijk}(t-t_1, t-t_2)$ for the second-order nonlinear process:

$$P_i(t) = \epsilon_0\sum_{j=1}^{3}\sum_{k=1}^{3}\int_{-\infty}^{t}\int_{-\infty}^{t}\chi^{(2)}_{ijk}(t-t_1,t-t_2)E_j(t_1)E_k(t_2)dt_1dt_2$$

We should make clear that the first order liner effect as one connects materials properties linearly changing with applied field and should not apply in general for describing strong non linear phenomena im materials where one has to go beyond the description to nonlinear response theory. When considering the time-domain response of a material to an external perturbation, one deals frequency-dependent susceptibilities. These susceptibilities can be expressed in terms of tensor notation and integrated over frequency to account for the material's response over a range of frequencies. In the frequency domain, the induced polarization (P) can be expressed in terms of the applied electric field (E) and the susceptibility tensor as:

$$P_i(\omega) = \epsilon_0\sum_{j=1}^{3}\sum_{k=1}^{3}\int\int\chi^{(2)}_{ijk}(\omega,\omega_1,\omega_2)E_j(\omega_1)E_k(\omega_2)\,d\omega_1\,d\omega_2$$

Where:

- $P_i(\omega)$ is the induced polarization component at frequency ω along direction i,
- $\chi^{(2)}_{ijk}(\omega, \omega_1, \omega_2)$ is the frequency-dependent second-order susceptibility tensor,
- $E_j(\omega_1)$ and $E_k(\omega_2)$ are the components of the applied electric field at frequencies ω_1 and ω_2 respectively, and
- The integral is taken over all possible frequencies.

In summary, the nonlinear response of a material to external perturbations can be described using tensor notation, incorporating frequency or time integrals to capture the material's response over a range of frequencies or times. The high-order susceptibility tensor ($\chi^{(n)}$) plays a crucial role in characterizing this nonlinear response. Frequency and Intensity-dependent absorption is a key feature of nonlinear response and is often exploited in applications such as laser-induced material processing.

1.2 Photocarrier Injection

Photocarrier injection is a phenomenon in semiconductor physics and optoelectronics where photoexcited carriers (electrons and holes) are injected into a semiconductor material due to the absorption of photons. When light is incident on a semiconductor material, it generates electron-hole pairs, creating an excess of carriers within the material. If the semiconductor is part of an electronic circuit, or if photocarriers have a mean velocity or a bias voltage is applied, the current may be observed with a circuit. These excess carriers can contribute to the flow of electrical current. The injected currents have complex components, including a shif current and injection current. The injection current persists even after the laser pulse has ended and it arises from the breaking of time-reversal symmetry through elliptically or circularly polarized light, as well as the breaking of intrinsic spatial inversion symmetry. The injection current is a manifestation of quantum interference between various excitation pathways, leading to a polar

distribution of electrons or holes in momentum space. Shift current, also known as displacement current, refers to a nonlinear optical response observed in materials with broken inversion symmetry when subjected to an oscillating electric field. Shift current arises due to the displacement of charge within the material in response to the changing electric field, rather than the flow of charge carriers as in conventional currents.

For the photovoltaic injection in bulk systems, the second-order nonlinear optical effect, as explored in [5], has garnered considerable attention for its potential in achieving highly efficient light-to-current conversion. Investigations into shift-current, detailed in references [6–9], exemplify the significance of this phenomenon.

Another noteworthy aspect of second-order nonlinear current is the ”injection current”[5, 10–13]. This current can be induced by the breaking of time-reversal symmetry through elliptically or circularly polarized light, in addition to the breaking of intrinsic spatial inversion symmetry. The injection current results from the population imbalance induced by quantum interference (QuI) between various excitation paths, arising from the interference between absorption pathways associated with orthogonal components of polarization. Consequently, this leads to a polar distribution of electrons or holes in momentum space, generating a current injection that temporally aligns with optical intensity. Remarkably, the non-oscillating current induced by quantum interference may persist even after the perturbing laser irradiation stops.

It is noteworthy that, unlike the shift-current occurs solely during laser irradiation, the injection current exhibits persistence even after the conclusion of laser irradiation. This enduring quality underscores the unique and sustained contribution of the injection current in the context of nonlinear optical effects.

Going, beyond second-order nonlinear effects, researchers have investigated into the realm of photovoltaic effects induced by intense few-cycle laser pulses [14–19]. Notably, such laser pulses possess the capability to extrinsically break spatial inversion symmetry. In addition to this, the presence of a strong field introduces highly nonlinear excitation channels, including pathways such as tunneling excitation. The combination of extrinsic spatial inversion symmetry breaking and

intense nonlinear interactions between light and matter opens the possibility for an intense few-cycle laser pulse to induce a direct current (dc-current) even in a material with intrinsic inversion symmetry.

The uniqueness of the photovoltaic effect with a few-cycle pulse lies in its dependence on breaking the inversion symmetry of the incident light fields. This intrinsic connection allows for the manipulation of the induced current by controlling both the intensity and carrier-envelope phase of the pulse [14, 17]. The exploration of these intense few-cycle laser pulses not only expands the understanding of nonlinear optical phenomena but also unveils avenues for precise control and manipulation of induced currents through tailored light-matter interactions.

In recent research, an effective method for manipulating valley population has surfaced, centered around the interplay of two circularly polarized lights with different frequencies, denoted as ω and 2ω. This investigation is particularly fitting in the context of two-dimensional systems [20, 21]. Individually, each circularly polarized light breaks time-reversal symmetry, and when combined, the fields exhibit the added capability of breaking spatial inversion symmetry. This coupled contravention upon time-reversal and spatial inversion symmetries gives rise to a population imbalance in momentum space upon laser excitation. This, in turn, apperas as a sustained charge flow persisting even after the laser irradiation. Notably, this methodology has extended beyond theoretical exploration, with numerical studies incorporating first-principles calculations applied to bulk solids [22]. The multifaceted approach of combining circularly polarized lights at different frequencies not only enriches our understanding of valley population dynamics but also holds promise for diverse technological applications in the realm of materials and quantum control phenomena.

1.3 High-order Harmonic Generation

Traditional hgh-order harmonic generation (HHG) is a phenomenon where intense laser light interacts with a gas, causing the generation of very high-frequency

light waves. This process typically occurs when a strong laser field ionizes a material, causing electrons to be ripped away from atoms. These electrons then undergo complex dynamics, involving acceleration, coherent motion, and recombination with their parent ions. Through this intricate dance, the electrons emit high-energy photons with frequencies much higher than that of the incident laser, often extending into the extreme ultraviolet (XUV) and X-ray regions of the electromagnetic spectrum [23].

Since first observed in 1987 using rare gases as target specimens [24, 25], gas-phase HHG has been intensively utilized to generate ultrashort attosecond light pulses [26–28] for investigating ultrafast dynamics in matter in the time domain which is a typical time scale for the motion of electrons.[29–32]. HHG provides a unique window into electron dynamics and allows us to investigate processes occurring on attosecond timescales. The emitted harmonics carry valuable information about the electronic structure, band gaps, and transient states of the material, offering a powerful tool for probing and controlling ultrafast processes. In recent years, there have been significant advancements in experimental techniques for studying high-order harmonic generation. The use of intense femtosecond laser pulses, pulse shaping methods, and advanced detection schemes have enabled precise control and characterization of the generated harmonics. These experimental advances have led to breakthroughs in attosecond science, providing tools for investigating ultrafast phenomena in a wide range of atoms [30, 33, 34], molecules [35–37], and solids [31, 32, 38–40]. The HHG in solid-state systems was first observed in ZnO in 2011 in mid-infrared (MIR) laser field [41], and it has since garnered significant attention, both from a fundamental research perspective and due to its technological potential, as evidenced by recent studies in solids [42–46].

1.4 Review on Theoretical Models

The generation of nonlinear optical response in solids involves complex quantum mechanical processes and intricate interplays between the laser field and the electronic structure of atoms. The fundamental processes involved in HHG

in a gaseous medium can be understood within the framework of the well-known three-step model [47, 48]. This semi-classical framework delineates the gas HHG process through three stages, see Figure. (1.1):

- 1. Ionization/Tunneling: Initially, an electron is ionized by the intense laser field and electrons are stripped away from the atom due to the strong electric field of the laser.
- 2. Acceleration: Subsequently, the strong laser field imparts energy to the liberated electron kinetic energy, propelling its acceleration away from the ionized molecule.
- 3. Recombination: In the final step, the oscillatory force of the laser field drives the electron back toward the ionized parent molecule. During this process, the electron undergoes recombination with the molecule, releasing the surplus kinetic energy acquired in the second step in the form of a high-energy photon.

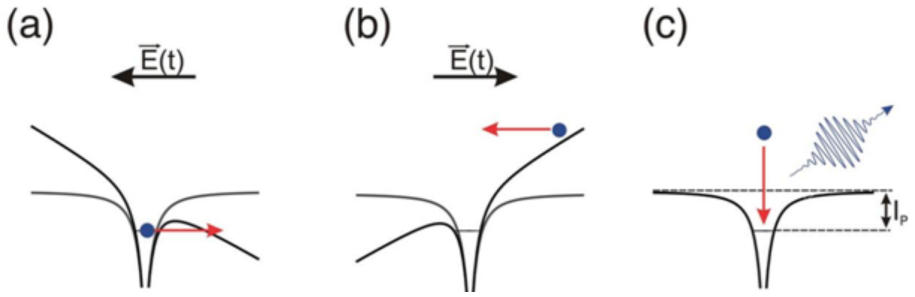

Figure 1.1: Three step model: (a) Ionization/Tunneling (b) Accelaeration (c) Recombination

However, this model is not directly applicable to solid-state HHG due to differences in density, structure, band structure, Coulomb interactions, and surface effects between gases and solids. Solid-state HHG involves more complex mechanisms, including interactions with the crystalline lattice and surface effects, requiring sophisticated theoretical models for accurate description.

The understanding and control of HHG have been greatly advanced by the development of sophisticated theoretical models, the primary and widely used numerical methods are based on time-dependent Schrödinger equation (TDSE)

, semiconductor Bloch equations (SBE) and time-dependent density-functional theory (TDDFT). We won't go in detailed about the theoretical foundations, but just summarize current status and some challenges of present numerical simulations which are yet to be improved or solved, for detailed mechanisms and numerical implementations, please refer to the basic references where all those methods are disucssed at lenght.

- The time-dependent-Schrödinger equation (TDSE) model [49–57], utilizing both Bloch state basis and Houston state basis, is proficient in examining electronic dynamics within periodic potentials. Nonetheless, simulating the HHG of real solid materials proves challenging, primarily due to the method's reliance on idealized model potentials.
- The semiconductor Bloch equations (SBE) [58–68], improving it from a two-band model to a multiband model allows for a more comprehensive study of real systems, effectively capturing the main features of High-Order Harmonic Generation (HHG) in solids. This enhancement involves incorporating accurate energy bands and transition dipole moments derived from first-principles calculations. Future endeavors should focus on obtaining the correct phase of transition dipole elements. However, a significant challenge persists as current first-principles codes often yield random phases for transition dipole moments.
- The time-dependent density-functional theory (TDDFT) model [69–75] appears to be the ideal approach for straightforwardly studying High-Order Harmonic Generation (HHG) in solids within real coordinate space. However, its main drawback lies in its significant computational time requirements. Additionally, directly and intuitively analyzing the physical processes or mechanisms within the solid-state energy band picture can pose challenges within the TDDFT framework.

Furthermore, properly incorporating Berry curvature in models and understanding its role in solid High-Order Harmonic Generation (HHG) requires more attention in future theoretical simulations. Despite lingering open questions in this evolving field, it's hoped that this review can offer valuable reference points, and

ongoing efforts from the relevant community will gradually illuminate the intricacies of solid HHG studies.

1.5 Structure of the Thesis

This thesis is organized as follows: Chapter. 2 first introduces the crystallographic discription for typical hexagonal lattice we are studying, then we study the light-induced electron dynamics in 2D materials based on the tight-binding model by time-dependent Schrodinger Equation and quantum master equation, to account for dissipative phenomena that plays a fundamental role in the laser induced electron dyanmics that we will describe in detail in the follwoing chapters of this thesis. In Chapter. 3 we investigate light-induced electron dynamics in monolayer hexagonal boron nitride under the influence of two-color linearly-polarized laser fields at frequencies ω and 2ω, by solving the time-dependent Schrödinger equation with a tight-binding model. We start from time-dependent perturbative analysis in the weak field regime, then we expand our results to third-order nonlinear regime and deeply off-resonant highly-nonlinear regime. In Chapter. 4, we study THz-induced HHG in graphene with the method described by quantum master equation. The microscopic mechanism of HHG with the quasi-static approximation and the population distribution in the Brillouin zone is described in detail together with its numerical implementation in Chapter. 5. We further elucidate the role of the nonequilibrium nature of THz-induced electron dynamics by comparing the nonequilibrium picture in the present work and the thermodynamic picture in the previous work [76]. We explore the possibility of using a THz field to enhance MIR-induced HHG in graphene based on the knowledge gained from Chapter. 4. We investigate the dynamics under MIR and THz fields and evaluate the emitted harmonic spectra. As a result of the analysis, we find that cou- pling via the induced coherence by THz and MIR fields plays an essential role in enhancing MIR-induced HHG, clarifying the importance of the field-induced coherence beyond the simple population effect. Finally, the conclusion and perspectvies of this thesis is summarized in in Chapter. 6

Chapter 2

THEORETICAL FOUNDATIONS

In recent years, 2D materials have emerged as a fascinating class of materials with unique properties and promising applications in various fields ranging from electronics and photonics to energy and biotechnology. These materials, which exhibit extraordinary properties due to their ultrathin nature, are reshaping the landscape of materials science and engineering. Among the diverse array of 2D materials, graphene, transition metal dichalcogenides (TMDs), hexagonal boron nitride (h-BN), and other emerging candidates stand out for their exceptional characteristics and potential applications. We introduce 2D materials with a typical hexagonal lattice nanostructure and their crystallography properties in this chapter. We then introduce the tight-binding approach, which is basic for understanding the electronic properties of materials, with a particular focus on the nearest neighbor tight-binding model. We also discuss the electron dynamics in 2D materials, including the time-dependent Schrödinger equation and quantum master equation which are fundamental for studying the nonlinear optical response in this thesis. We introduce several typical 2D materials:

Graphene: a single layer of carbon atoms arranged in a honeycomb lattice, is the archetype of 2D materials. Graphene exhibits mechanical strength, electrical conductivity, and thermal conductivity. Its unique electronic band structure and optical properties make it a versatile material for various applications in electronics, such as high-speed transistors and flexible displays, as well as in energy storage, sensors, and biomedical devices.

Hexagonal Boron Nitride (h-BN): a structural analog of graphene, consists of alternating boron and nitrogen atoms arranged in a hexagonal lattice. h-BN exhibits excellent thermal and chemical stability, as well as a large bandgap, making it an insulating material. Its flat and atomically smooth surface makes it an ideal substrate for 2D materials and a protective coating in electronic devices. It is widely used as a dielectric material in transistors, tunneling barriers in spintronics.

Transition Metal Dichalcogenides (TMDs): a class of 2D materials composed of transition metal atoms sandwiched between two layers of chalcogen atoms (e.g., sulfur, selenium, or tellurium). TMDs exhibit intriguing electronic, optical, and mechanical properties, which can be tuned by varying the composition and layer thickness. They often possess a direct bandgap, making them suitable for optoelectronic applications. They are used in field-effect transistors, photodetectors, light-emitting diodes (LEDs), and other optoelectronic devices. They also hold promise in catalysis, sensing, and flexible electronics.

Other Emerging 2D Materials like Black Phosphorus: a layered semiconductor, offers tunable bandgap and high carrier mobility, making it suitable for electronic and optoelectronic applications. MXenes are a family of 2D transition metal carbides, nitrides, and carbonitrides with metallic conductivity and excellent mechanical properties, holding promise in energy storage, catalysis, and electromagnetic shielding. Perovskite Nanosheets: Perovskite nanosheets exhibit remarkable photophysical properties and are being explored for applications in solar cells, photodetectors, and light-emitting devices.

In summary, 2D materials, including graphene, TMDs, h-BN, and other emerging candidates, offer a rich platform for exploring novel physical phenomena and developing advanced technologies with unprecedented performance and functionality. Their diverse properties and potential applications make them a vibrant area of research in materials science and engineering. The inclusion of artificial 2D materials based on moiré superlattices underscores the dynamic nature of this field and the potential for groundbreaking discoveries [77].

2.1 Crystallography Properties

Hexagonal lattice nanostructures are fundamental building blocks in the realm of 2D materials, encompassing a diverse range of materials with hexagonal symmetry. From natural materials like graphene and h-BN to artificial structures based on moiré physics [77], the crystallographic properties of hexagonal lattices underpin the rich and varied behavior observed in 2D materials, offering ample opportunities for scientific exploration and technological innovation. As a fundamental Bravais lattice, it manifests as a distinctive geometric arrangement prevalent across a spectrum of materials, owing to its highly efficient packing characteristics. This lattice's spatial configuration profoundly influences the mechanical, electrical, and thermal properties of materials. Understanding lattice structures is crucial for deciphering material behavior across diverse conditions, spanning from semimetals to topological insulators. This significance is particularly noteworthy in the realm of two-dimensional materials. We have selected graphene, exemplifying a semimetal, and hexagonal boron nitride (h-BN), recognized as an insulator, for our discussion on nonlinear optical response on 2D materials.

Graphene's lattice structure is hexagonal lattice nanostructure for carbon al-

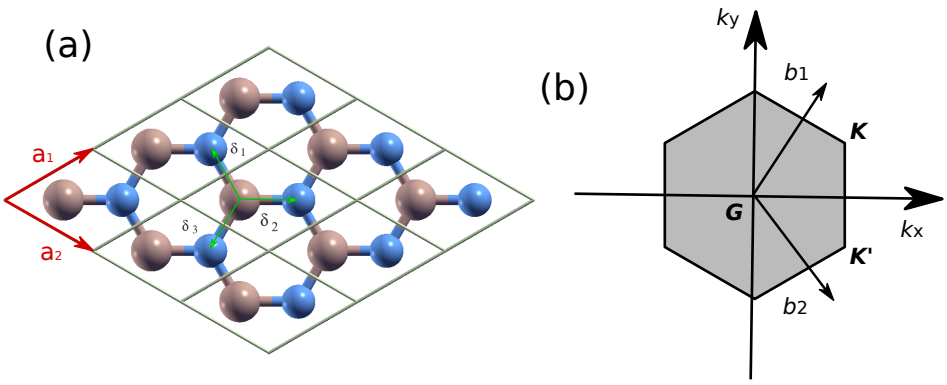

Figure 2.1: (a) Hexagonal lattice,the two triangular sublattices are shown in two different colors. (b) Brillouin zone in momentum space.

lotrope, showed in Figure 2.1 (a). Carbon atoms lie in a single layer, forming an exceptional two-dimensional material. The unique atomic-scale hexagonal lattice structure involves each carbon atom intricately bonding through σ-bonds

with its three nearest neighbors and a delocalized π-bond. This precise arrangement plays a important role in the formation of Dirac cone, making monolayer graphene an outstanding conductor of electricity, and finding applications in electronic devices, sensors, and various fields [78].

Similar to graphene, h-BN also features a hexagonal lattice structure, but with alternating boron and nitrogen atoms forming the hexagons, making it a wide-gap insulator due to inversion symmetry breaking, which is used as a dielectric material in electronics, a substrate for graphene-based devices, and as a solid lubricant. We define the basis of hexagonal lattice primitive vectors $E = (\vec{a}_1, \vec{a}_2)$ as shown in Fig 2.1 (a):

$$\vec{a}_1 = a \begin{pmatrix} \frac{\sqrt{3}}{2} \\ \frac{1}{2} \end{pmatrix}, \vec{a}_2 = a \begin{pmatrix} \frac{\sqrt{3}}{2} \\ -\frac{1}{2} \end{pmatrix}$$

where a is the lattice constant, for graphene $a = 1.42\mathring{A}$ [78], and for h-BN $a = 2.5\mathring{A}$ [79]. Generate only A sites while sites in B sublattice are generated by $n_1\vec{a}_1 + n_2\vec{a}_2 + \vec{\delta}$, where $\vec{\delta}$ has to be chosen as one of the three nearest-neighbor vectors,

$$\vec{\delta}_1 = a \begin{pmatrix} -\frac{1}{2\sqrt{3}} \\ \frac{1}{2} \end{pmatrix}, \vec{\delta}_2 = a \begin{pmatrix} \frac{1}{\sqrt{3}} \\ 0 \end{pmatrix}, \vec{\delta}_3 = a \begin{pmatrix} -\frac{1}{2\sqrt{3}} \\ -\frac{1}{2} \end{pmatrix}$$

The reciprocal basis $B = (b_1, b_2, b_3)$ is generated using the formula:

$$\overrightarrow{b_k} = \frac{2\pi \cdot \overrightarrow{a_i} \times \overrightarrow{a_j}}{V}$$

i, j, k are circular permutations, V $= \overrightarrow{a_1} \cdot (\overrightarrow{a_2} \times \overrightarrow{a_3})$, presents the mix product between the three vectors, i.e. the volume of the unitary cell. By assuming the lattice primitive vector in the vertical direction of the two-dimensional material plane is infinit, $\overrightarrow{a_3} \to \infty$, we get the 2D reciprocal vectors as shown in Fig2.1 (b):

$$\vec{b}_1 = k_D \begin{pmatrix} \frac{1}{2} \\ \frac{\sqrt{3}}{2} \end{pmatrix}, \vec{b}_2 = k_D \begin{pmatrix} \frac{1}{2} \\ -\frac{\sqrt{3}}{2} \end{pmatrix}$$

with $k_D = \frac{4\pi}{\sqrt{3}a}$. The corresponding Brillouin zone is depicted together with the two high-symmetry points K and K′ Fig 2.1 (b). Two inequivalent corners of the

Brillouin zone K and K' can be chosen as follows:

$$K = k_D\left(\frac{1}{2}, \frac{1}{2\sqrt{3}}\right), \quad K' = k_D\left(\frac{1}{2}, -\frac{1}{2\sqrt{3}}\right)$$

2.2 Tight-binding Approach

In this section, we delve into the fundamental principles of the tight-binding approach, with a particular focus on the nearest neighbor tight-binding model. This approach is essential for understanding the electronic properties of materials and is a crucial component of graphene's electronic structure analysis. In solid-state physics, the tight-binding model is a theoretical framework used to describe the electronic structure of crystalline materials. It treats each atomic orbital as a basis function and describes the electronic wavefunction as an expansion in terms of these basis functions. One common approach is to expand the wavefunction using Linear Combination of Atomic Orbitals (LCAO). In this method, the wavefunction on position r in the crystal lattice is expressed as a linear combination of atomic orbitals centered on individual atoms:

$$\phi_\beta(\mathbf{r}) = \sum_{\mathbf{R}_\alpha} b_\beta\left(\mathbf{R}_\alpha\right) \varphi_\beta\left(\mathbf{r} - \mathbf{R}_\alpha\right) \tag{2.1}$$

Here, b are coefficients for the linear combination, β is the general atomic orbitals index, φ_β are the atomic orbitals which are eigenfunctions of the Hamiltonian H_α of a single isolated atom α. The Bloch theorem states that the wave function in a crystal can change under translation only by a phase factor:

$$\phi\left(\mathbf{r} + \mathbf{R}_\alpha\right) = e^{i\mathbf{k}\cdot\mathbf{R}_\alpha}\psi(\mathbf{r}) \tag{2.2}$$

The foundation of the tight-binding approach is rooted in the Bloch theorem, which is satisfied by the tight-binding function by combining Eq. (2.1) and Eq. (2.3):

$$\Phi_{\alpha,\beta}(\mathbf{r}, \mathbf{k}) = \frac{1}{\sqrt{N}} \sum_{\mathbf{R}} e^{i\mathbf{k}\cdot\mathbf{R}} \phi_{\alpha,\beta}\left(\mathbf{r} - \mathbf{R}_{\alpha,\beta}\right), \alpha = A \text{ or } B \tag{2.3}$$

For simplicity, we only consider the contribution from the outermost valence band electron's orbital and omit β in the following discussion. N represents the

number of unit cells, and $\phi_\alpha(\mathbf{r}-\mathbf{R}_\alpha)$ denotes the orbital function of an electron at cell $\mathbf{R}$ in sublattice α. In the context of a honeycomb lattice, we focus on the nearest neighbor approximation. This approximation asserts that an atom in sublattice A only interacts with its three closest neighbor atoms in sublattice B. This simplification is particularly useful for understanding the interactions between electrons bound to non-equivalent atoms.

The Hamiltonian for this nearest-neighbor interaction is expressed as:

$$\hat{H}_{AB} = \frac{1}{N}\sum_{\mathbf{R}_A}\sum_{\mathbf{R}_B} e^{i\mathbf{k}(\mathbf{R}_B-\mathbf{R}_A)} \left\langle \phi_A\left(\mathbf{r}-\mathbf{R_A}\right)|\hat{H}|\phi_B\left(\mathbf{r}-\mathbf{R}_B\right)\right\rangle \tag{2.4}$$

Due to the translational invariance in a Bravais lattice, the summation over each atom in a sublattice occurs N times, simplifying the expression to:

$$\hat{H}_{AB} = \sum_{\mathbf{R}_A} e^{i\mathbf{k}(\mathbf{R}_B-\mathbf{R}_A)} \left\langle \phi_A\left(\mathbf{r}-\mathbf{R_A}\right)|\hat{H}|\phi_B\left(\mathbf{r}-\mathbf{R}_B\right)\right\rangle \tag{2.5}$$

We transform the Hamiltonian of real space into the momentum space representation, and then the tight-binding Hamiltonian under the matrix representation is:

$$\hat{H} = \begin{pmatrix} \epsilon_A & t_0 f(\mathbf{k}) \\ t_0 f(\mathbf{k})^* & \epsilon_B \end{pmatrix} \tag{2.6}$$

Here ϵ_A and ϵ_B are the on-site energies of electrons on the nearest neighbor atoms, t_0 presents the hopping parameter:

$$t_0 = \left\langle \phi_A\left(\mathbf{r}-\mathbf{R_A}\right)|\hat{H}|\phi_B\left(\mathbf{r}-\mathbf{R}_A-\vec{\delta}_i\right)\right\rangle \quad (i=1,2,3)$$

For typical hexagonal lattice under our discussion, the three nearest neighbor hoping strength here are identical here due to the hexagonal lattice symmetry. For graphene, we set ϵ_A and ϵ_B to 0, and $t_0 = 2.8\ eV$ in accordance with the previous work [78]. For h-BN ϵ_{B} and ϵ_{N} denote the on-site energies for boron and nitrogen sites, respectively.

$$\hat{H}(\mathbf{k}) = \begin{pmatrix} \epsilon_{\mathrm{B}} & t_0 f(\mathbf{k}) \\ t_0 f(\mathbf{k})^* & \epsilon_{\mathrm{N}} \end{pmatrix}, \tag{2.7}$$

We set ϵ_{B} to 3.34 eV and ϵ_{N} to $-2.56\ eV$ and t_0 to $2.6\ eV$ computed with the first-principles calculations [80], the band gap $E_g = \epsilon_b - \epsilon_n$ equals 5.9 eV.

The off-diagonal terms of the tight-binding Hamiltonian 2.6:

$$\begin{aligned} f(\mathbf{k}) &= e^{i\mathbf{k}\vec{\delta}_1} + e^{i\mathbf{k}\vec{\delta}_2} + e^{i\mathbf{k}\vec{\delta}_3} \\ &= e^{-\frac{iak_x}{\sqrt{3}}} + 2e^{\frac{iak_x}{2\sqrt{3}}} \cos\left(\frac{a}{2}k_y\right) \end{aligned} \tag{2.8}$$

Solving the stationary Schrödinger equation using matrix diagonalization:

$$\hat{H}_{\mathbf{k}}|\phi_{b\mathbf{k}}\rangle = \epsilon_{b\mathbf{k}}|\phi_b\rangle, \tag{2.9}$$

we get the eigenenergy of Hamiltonian from 2.6, where b is a band index, $|\phi_{b\mathbf{k}}\rangle$ is an eigenstate, and $\epsilon_{b\mathbf{k}}$ corresponds to the eigenenergy. As the Hamiltonian is a 2-by-2 matrix in this work, the band index b denotes either a conduction ($b = c$) or valence ($b = v$) state.

$$\epsilon_{b\mathbf{k}} = E_0 \pm \frac{1}{2}\sqrt{E_g^2 + 4t_0^2|f|^2} \tag{2.10}$$

$E_0 = \frac{\epsilon_A + \epsilon_B}{2}$ and $E_g = \epsilon_b - \epsilon_n$ is the energy gap. For graphene, $\epsilon_A = \epsilon_B = 0$ the band gap equals 0. Their corresponding eigenvectors are:

$$|\phi_b\rangle = \begin{pmatrix} \frac{E_g \pm \sqrt{E_g^2 + 4t_0^2|f|^2}}{2t_0 f^*} \\ 1 \end{pmatrix} \tag{2.11}$$

Tight-binding model is an approximation to the first principles models that can be drerived from ab-initio DFT calculations and used to improve computational effeciency through Wannierization. Wannierization facilitates the transformation of electronic wavefunctions from a basis of Bloch states to localized Wannier functions. Wannier functions provide a clearer physical interpretation of the electronic structure compared to Bloch states. Each Wannier function corresponds to an electron localized around a particular atomic site within the crystal lattice. This localization allows for a more intuitive understanding of electronic properties, such as onsite energy, bonding, hopping, and interactions, in terms of localized atomic-like orbitals. Wannierization can help educe

the size of the Hilbert space, as the model focuses on the interactions between a limited number of localized orbitals rather than considering the entire Brillouin zone; provide a systematic method for constructing the tight-binding Hamiltonian; allow for the localization of these interaction terms around specific lattice sites, making the tight-binding model more physically intuitive and interpretable; moreover, enable the incorporation of additional physical effects, such as electron-electron interactions, spin-orbit coupling, and lattice distortions, into the tight-binding model.

In 2D materials, quantum effects become prominent due to the reduced dimensionality, leading to the emergence of novel electronic states and phenomena. Understanding how topological obstruction influences the electronic structure of 2D materials sheds light on the quantum behavior that governs their properties. For 2D systems, the quantity of topological index as a surface integral over the Brillouin Zone is defined as the Chern number:

$$W_n = \frac{1}{2\pi} \iint_{BZ} d^2k \cdot \vec{\Omega}_n \tag{2.12}$$

Quantized Hall conductance σ_{xy} can be calculated using the Chern number and the TKNN formula[81]:

$$\sigma_{xy} = \frac{e^2}{h} W_n \tag{2.13}$$

$\vec{\Omega}_n$ is the Berry curvature, which is defined as the curl(rotor) of the Berry connection or the Berry vector potential $\mathcal{A}(k) = \left\langle n(k) \left| i\nabla_k \right| n(k) \right\rangle$[82]. Barry phase γ_n is expressed as a closed path $\mathcal{C}$ integral in the k-space $\gamma_n = \oint_{\mathcal{C}} dk \cdot \mathcal{A}_n(k) = \int_{\mathcal{S}} dk \cdot \vec{\Omega}_n(k)$. $n(k)$ denotes the n^{th} eigenstate of the Bloch Hamiltonian $H(k)$ for general systems. The Berry curvature $\vec{\Omega}_n$ is an intrinsic property of the band structure because it only depends on the wave function, which can be nonzero in crystals with broken time-reversal or inversion symmetry.[83]

$$\vec{\Omega}_n(k) = \nabla_k \times \mathcal{A}(k) \tag{2.14}$$

Using $\langle n|\partial H/\partial k|n'\rangle = \langle \partial n/\partial k \mid n' \rangle (E_n - E_{n'})$ for $n' \neq n$, the Berry curvature

can be also written as a summation over the eigenstates:

$$\vec{\Omega}_n(k) = \mathrm{Im} \sum_{n' \neq n} \frac{\left\langle n(k) \left| \nabla_k H(k) \right| n'(k) \right\rangle \times \left\langle n'(k) \left| \nabla_k H(k) \right| n(k) \right\rangle}{\left(E_{n'}(k) - E_n(k) \right)^2} \tag{2.15}$$

which is useful to calculate the numerically the integral.

Hereafter, for two-band tight-binding model, $n(k)$ is the instantaneous eigenstates of the time-dependent Hamiltonian H from Eq. (2.20) under the vector potential $\mathbf{A}(\mathbf{t})$. $n(k)$ equals to $\phi_{v,k+\mathbf{A}(t)}$ and $\phi_{c,k+\mathbf{A}(t)}$ for the valence band and the conduction band. One get the Berry curvature for conduction band of 2D-systems:

$$\vec{\Omega}_{c,k_x k_y}(k) = i \frac{\left\langle \phi_c(k) \left| \partial H(k)/\partial k_x \right| \phi_v(k) \right\rangle \left\langle \phi_v(k) \left| \partial H(k)/\partial k_y \right| \phi_c(k) \right\rangle - (k_y \leftrightarrow k_x)}{\left(\epsilon_c(k) - \epsilon_v(k) \right)^2} \tag{2.16}$$

Normally, for monolayer graphene, inversion symmetry hodes $\Omega_n(-k) = \Omega_n(k)$. Also, the Berry curvature and momentum change sign under time-reversal, so that the Berry curvature at one momentum becomes opposite to the Berry curvature at opposite momentum $\Omega_n(-k) = -\Omega_n(k)$, so $\Omega_n(k) = 0$ and $\sigma_{xy} = 0$. [83]. For non-centrosymmetric crystals, for instance monolayer hBN, inversion symmetry is broken but time reversal symmetry holds, we have $\Omega_n(k) \neq 0$ and $\sigma_{xy} = 0$. And if only time reversal symmetry broken but inversion symmetry holds, for instance magnetic materials, we have $\Omega_n(k) \neq 0$ and $\sigma_{xy} \neq 0$.

For graphene/hBN:

$$\frac{\partial H}{\partial k} = \begin{pmatrix} 0 & t_0 \frac{\partial f(k+\mathbf{A})}{\partial k} \\ t_0 \frac{\partial f^*(k+\mathbf{A})}{\partial k} & 0 \end{pmatrix}, \tag{2.17}$$

$$\frac{\partial f(k+\mathbf{A})}{\partial k} = i\vec{\delta}_1 e^{i(k+\mathbf{A})\cdot\vec{\delta}_1} + i\vec{\delta}_2 e^{i(k+\mathbf{A})\cdot\vec{\delta}_2} + i\vec{\delta}_3 e^{i(k+\mathbf{A})\cdot\vec{\delta}_3} \tag{2.18}$$

Exploring the theoretical foundations of light-induced topological phase transitions in 2D systems presents interests for research. However, in this thesis, our focus will be specifically on studing the properties and dynamics of nonlinear ex-

cited states. While the broader theoretical framework of light-induced topological phase transitions merits attention, our emphasis on nonlinear excited states allows for a deeper understanding of the complex interactions and phenomena that arise in 2D materials under optical excitation. By narrowing our scope in this manner, we aim to provide a comprehensive analysis of the nonlinear dynamics within the context of the broader field of topological photonics, shedding light on the intricate interplay between light, topology, and material properties.

2.3 Electron Dynamics

Consider the crystal under the homoheneous electric field **E**, the wavelength of the fields is much longer than the spatial scale of the electron dynamics, so-callsed long wavelength approximation, or dipole approximation. The electric field enter the solid system through a uniform vector potential $\mathbf{A}(t)$ under Peierls substitution[84]. The time-dependent Hamiltonian is written as

$$\hat{H}(t) = \frac{[\hat{\mathbf{p}} + e\mathbf{A}(t)]^2}{2m} + V(\mathbf{r}) \tag{2.19}$$

Transforming to the **k** -space representation, we have

$$\hat{H}(\mathbf{k}, t) = \hat{H}\left(\mathbf{k} + \frac{e}{\hbar}\mathbf{A}(t)\right) \tag{2.20}$$

where **k** denotes the Bloch wavevector, The vector potential $\mathbf{A}(t)$ is related to the applied electric field $\mathbf{E}(t)$ as $\mathbf{E}(t) = -d\mathbf{A}(t)/dt$, and it is included in the Hamiltonian as the wavevector shift $\mathbf{k} \to \mathbf{k} + e\mathbf{A}(t)/\hbar$ via the Peierls substitution [84].

TDSE allows for the direct simulation of the dynamics of photoexcited carriers in the presence of external fields, accounting for their interaction with the lattice and other carriers. However, the nonlinear optical response processes involve the dealing with open quantum systems involves accounting for the interactions between the system of interest and its surrounding environment, which leads to decoherence and dissipation. Instead of working with pure quantum states,

open quantum systems are described using density matrices. The density matrix incorporates both the system's state and the effects of its interaction with the environment, allowing for the representation of mixed states and accounting for decoherence. The dynamics of open quantum systems are typically governed by master equations. These equations describe the time evolution of the density matrix and capture the effects of dissipation and decoherence induced by the environment. HHG induced by intensied THz or MIR laser has strong relaxation which can not be ignored so we introduce quantum master equation for HHG progress under intensed long-term pulse. This allows for the study of HHG phenomena and the prediction of experimental observables in more realistic conditions.

2.3.1 Time-dependent Schrödinger Equation

The light-induced electron dynamics can be described by solving the following TDSE at each **k**-point:

$$i\hbar\frac{d}{dt}|\psi_{\mathbf{k}}(t)\rangle = \hat{H}\left(\mathbf{k}+\frac{e\mathbf{A}(t)}{\hbar}\right)|\psi_{\mathbf{k}}(t)\rangle, \tag{2.21}$$

$|\psi_{\mathbf{k}}(t)\rangle$ is a single-particle electroinc wavefunction at **k**. Solving this time-dependent Schrödinger equation (TDSE) is an initial value problem. In two-band systems, usually the ground state $|\psi_{\mathbf{k}}(0)\rangle$ is used as the initial state occupied at the valence band. Various numerical methods can be chosen for doing the time propagation, here we split the propagation into short-time propagation using the composition property rely on a sufficiently small Δt, $t' = t + \Delta t$,:

$$|\psi_{\mathbf{k}}(t')\rangle = \hat{T}\exp\left[-i\int_t^{t'} d\tau\hat{H}(\tau)\right]\left|\psi_{\mathbf{k}+\mathbf{A}(t)}\right\rangle \tag{2.22}$$

which means:

$$|\psi_{\mathbf{k}}(t')\rangle = \hat{T}\left\{\sum_{n=0}^{\infty}\frac{(-i)^n}{n!}\int_t^{t'}\mathrm{d}\tau_1\ldots\int_t^{t'}\mathrm{d}\tau_n\hat{H}(\tau_1)\ldots\hat{H}(\tau_n)\right\}\left|\psi_{\mathbf{k}+\mathbf{A}(t)}\right\rangle \tag{2.23}$$

If the Hamiltonian commutes with itself at different times:

$$|\psi_{\mathbf{k}}(t')\rangle = \hat{T}\exp\left\{-\mathrm{i}\,(t'-t)\,\hat{H}\right\}|\psi_{\mathbf{k}}(t)\rangle \tag{2.24}$$

Since Δt is sufficiently small, the exponential mid-point propagator:

$$\hat{T}\exp\left[-i\int_{t}^{t'}d\tau\hat{H}(\tau)\right] \approx \exp\{-\mathrm{i}\Delta t\hat{H}(t+\Delta t/2)\} \tag{2.25}$$

We approximate the exponential using a Taylor expansion to infinit-order:

$$\exp\{A\} = \sum_{k=0}^{\infty}\frac{1}{k!}A^{k} \tag{2.26}$$

in the real implementation, we expanded to the fourth-order. Once the time-evolution of the wavefunctions, $|\psi_{\mathbf{k}}(t)\rangle$ is computed, the current induced in the matter can be further evaluated with

$$\mathbf{J}_{\mathbf{k}}(t) = \frac{1}{(2\pi)^2}\int_{BZ}d\mathbf{k}\langle\psi_{\mathbf{k}}(t)|\hat{\mathbf{J}}_{\mathbf{k}}(t)|\psi_{\mathbf{k}}(t)\rangle. \tag{2.27}$$

Here, $\hat{\mathbf{J}}_{\mathbf{k}}(t)$ is the current operator, and it is defined as

$$\hat{\mathbf{J}}_{\mathbf{k}}(t) = \frac{\partial}{\partial\mathbf{k}}\hat{H}\left(\mathbf{k}+\frac{e\mathbf{A}(t)}{\hbar}\right) = -t_0\begin{pmatrix} 0 & \frac{\partial f(\mathbf{k}+\mathbf{A})}{\partial\mathbf{A}} \\ \frac{\partial f^{*}(\mathbf{k}+\mathbf{A})}{\partial\mathbf{A}} & 0 \end{pmatrix}, \tag{2.28}$$

where $\frac{\partial f(\mathbf{k})}{\partial\mathbf{k}}$ is given by

$$\frac{\partial f(\mathbf{k})}{\partial\mathbf{k}} = i\vec{\delta}_1 e^{i\mathbf{k}\cdot\vec{\delta}_1} + i\vec{\delta}_2 e^{i\mathbf{k}\cdot\vec{\delta}_2} + i\vec{\delta}_3 e^{i\mathbf{k}\cdot\vec{\delta}_3}. \tag{2.29}$$

We can also analyze the population distribution of photocarriers induced by the laser fields. To achieve this, we compute the conduction population distribution by projecting onto the eigenstates of the Hamiltonian defined as:

$$\hat{H}_k|\phi_{bk}\rangle = \epsilon_{bk}|\phi_{bk}\rangle, \tag{2.30}$$

where b is a band index, $|\phi_{bk}\rangle$ is an eigenstate, and ϵ_{bk} corresponds to the eigenvalue. $|u^{H}_{b\mathbf{k}}(t)\rangle$ are also defined as Houston states [85, 86], are characterized as

eigenstates of the instantaneous Hamiltonian, expressed as instantaneous adiabatic eigenstates, which will be also discussed in the later sections in relaxation approximation in Eq. (2.33) and in Appendix. A for adiabatic expansion.

As the Hamiltonian is a 2-by-2 matrix in this work, the band index b denotes either a conduction ($b = c$) or valence ($b = v$) state.

Using eigenstates defined with Eq. (2.30), the conduction population distribution n_{ck} after the laser irradiation can be evaluated as:

$$n_{ck} = \left|\langle \phi_{ck} | \psi_k(t_F) \right|^2, \tag{2.31}$$

where t can be an instantaneous time during or after the laser field. By imposing the normalization of $|\phi_{bk}\rangle$ and $|\psi_k(t)\rangle$, the computed conduction population satisfies $0 \leq n_{ck} \leq 1$. It is important to note that, in the present theoretical setup, the conduction population is a constant of motion after laser irradiation since any relaxation processes are not considered.

2.3.2 Quantum Master Equation

In contrast to closed quantum systems, which can be adequately described by the Schrödinger equation, the quantum master equation is typically used in the context of the time evolution of an open quantum system, where the system of interest is susceptible to exchanges of energy, particles with its external environment. To expound processes such as relaxation, dephasing, and thermalization of the nonlinear response experiments, the quantum master equation is predominantly employed which is salient in the realm of open quantum systems.
We describe the light-induced electron dynamics in graphene with the following quantum master equation [87–90]:

$$\frac{\mathrm{d}}{\mathrm{d}t}\rho_{\mathbf{k}}(t) = \frac{1}{i\hbar}\left[\hat{H}_{\mathbf{k}+e\mathbf{A}(t)/\hbar}, \rho_{\mathbf{k}}(t)\right] + \hat{D}\left[\rho_{\mathbf{k}}(t)\right], \tag{2.32}$$

$\rho_{\mathbf{k}}(t)$ is the reduced density matrix at $\mathbf{k}$. The quantum master equation delineates the dynamical evolution of the density matrix associated with the quantum system, which encompasses both pure and mixed quantum states. To elucidate the impact of dissipation, we formulate the relaxation operator, denoted

as $\hat{D}\left[\rho_{\mathbf{k}}(t)\right]$, within the framework of Eq.(2.32) employing the relaxation time approximation[91] and employing the Houston basis [85, 86]:

$$\hat{H}_{\mathbf{k}+e\mathbf{A}(t)/\hbar}|u^H_{b\mathbf{k}}(t)\rangle = \epsilon_{b,\mathbf{k}+e\mathbf{A}(t)/\hbar}|u^H_{b\mathbf{k}}(t)\rangle \tag{2.33}$$

The expansion of the reduced density matrix can then be carried out using the Houston states.

$$\rho_{\mathbf{k}}(t) = \sum_{bb'} \rho_{bb',\mathbf{k}}(t)|u^H_{b\mathbf{k}}(t)\rangle\langle u^H_{b'\mathbf{k}}(t)|, \tag{2.34}$$

where $\rho_{bb',\mathbf{k}}(t)$ are the expansion coefficients. On the basis of the Houston state expansion, we define the relaxation operator [87, 88, 92] as

$$\hat{D}\left[\rho_{\mathbf{k}}(t)\right] = -\sum_{b} \frac{\rho_{bb,\mathbf{k}}(t) - f^{FD}\left(\epsilon_{b,\mathbf{k}+e\mathbf{A}(t)/\hbar}, T_e, \mu\right)}{T_1}|u^H_{b\mathbf{k}}(t)\rangle\langle u^H_{b\mathbf{k}}(t)| \tag{2.35}$$

$$-\sum_{b\neq b'} \frac{\rho_{bb',\mathbf{k}}(t)}{T_2}|u^H_{b\mathbf{k}}(t)\rangle\langle u^H_{b'\mathbf{k}}(t)|, \tag{2.36}$$

T_1 is the longitudinal relaxation time, T_2 is the transverse relaxation time, and $f^{\mathrm{FD}}(\epsilon)$ is the Fermi–Dirac distribution:

$$f^{\mathrm{FD}}(\epsilon, T_e, \mu) = \frac{1}{e^{(\epsilon-\mu)/k_B T_e}+1}. \tag{2.37}$$

When $t = 0$, the eletron system are identical fermions in thermodynamic equilibrium, the average number of fermions in a single-particle state is given by the Fermi–Dirac distribution. μ is the chemical potential, and T_e is the electron temperature.

In the following discussion, we set the longitudinal relaxation time T_1 to 100 fs and the transverse relaxation time T_2 to 20 fs in accordance with the previous works [87–90]. The electron temperature T_e is set to 300 K unless stated otherwise. The chemical potential μ is treated as a tunable parameter to study the effect of doping.

We directly solve the quantum master equation, Eq. (2.32), in the time domain by employing the Runge-Kutta method without any approximation. The electric current is obtained by employing the time-dependent density matrix $\rho_{\mathbf{k}}(t)$, which

evolves according to Eq. (2.32):

$$\mathbf{J}(t) = \frac{2}{(2\pi)^2} \int d\mathbf{k} \mathrm{Tr} \left[\hat{\mathbf{J}}_{\mathbf{k}}(t) \rho_{\mathbf{k}}(t) \right], \tag{2.38}$$

where $\hat{\mathbf{J}}_{\mathbf{k}}(t)$ is the current operator defined as

$$\hat{\mathbf{J}}_{\mathbf{k}}(t) = -\frac{\partial H(\mathbf{k} + e\mathbf{A}(t)/\hbar)}{\partial \mathbf{A}(t)}. \tag{2.39}$$

The intraband component of the current is the dominant component for nonlinear current contribute HHG progress which will be discussed in the Chapter 4, we can get the intraband current by:

$$\mathbf{J}_{\mathbf{k}}^{\text{intra}}(t) = \sum_{b=v,c} \frac{(-2)}{(2\pi)^2} \frac{e}{\hbar} \times \int d\mathbf{k} \frac{\partial \epsilon_{b,\mathbf{k}+e\mathbf{A}(t)/\hbar}}{\partial \mathbf{k}} n_{b,\mathbf{k}+e\mathbf{A}(t)/\hbar},$$

where the band population $n_{b,\mathbf{k}+e\mathbf{A}(t)/\hbar}$ is defined with the Houston states of the Hamiltonian $|u^H_{b,\mathbf{k}}(t)\rangle$ computed from Eq 2.33, which can be useful for the microscopic analysis in the folowing chapters:

$$n_{b,\mathbf{k}+e\mathbf{A}(t)/\hbar}(t) = \langle u^H_{b,\mathbf{k}}(t) | \rho_{\mathbf{k}}(t) | u^H_{b,\mathbf{k}}(t) \rangle \tag{2.40}$$

This page is intentionally left blank.

Chapter 3

PHOTOVOLTAIC EFFECTS INDUCED BY CO-LINEAR POLARIZED LIGHT

The discussion and results presented in this chapter ar an adaptation of the article by Ref[Wenwen Mao *et al.*, Nonlinear current injection in hexagonal boron nitride using linearly polarized light in a deeply off-resonant regime. (2024) *Advanced Optical Materials*, (Under Review)]

Photovoltaic effect involves the generation of electric current in response to incident light in photovoltaic materials. To describe and analyze this phenomenon, one must consider the absorption of light as we introduced in Section. (1.2) in introduction, including generation and recombination of charge carriers, establishment of built-in potential and electric field, extraction of charge carriers. The conduction band population distribution plays a crucial role in the operation of photovoltaic devices by influencing the movement of charge carriers and the efficiency of light-to-electricity conversion. When photons with energy greater than the bandgap of the semiconductor material are absorbed, electrons in the valence band are excited to the conduction band, creating electron-hole pairs. These photogenerated electrons contribute to the population of the conduction band. All these terms provide a comprehensive framework for understanding the operation and optimization of photovoltaic devices.

Addressing the photovoltaic effect within the perturbative regime has garnered significant attention, particularly in the exploration of dc current injection

using two-color linearly polarized light [93–99]. Early investigations have underscored the complex interaction between a fundamental frequency, denoted as ω, and its second harmonic, 2ω [93–95]. A notable study by Jimenez-Galan et al. [20] utilized deeply off-resonant bi-circular laser fields with ω and 2ω to generate a substantial population imbalance in the Brillouin zone. However, it is worth noting that, in principle, linearly polarized light with two frequencies is sufficient to break time-reversal symmetry.

In this chapter, we first theoretically explore the phenomenon of dc-current injection and the generation of population imbalance through the application of two-color linearly polarized laser fields with frequencies ω and 2ω based on time-dependent perturbation analysis. Then we look into light-induced electron dynamics in a typical two-dimensional insulator, h-BN, based on a simple tight-binding approximation in a perturbative resonant regime using the TDSE introduced in Chapter. (2).

In our quantum dynamics simulations, we further uncover that ballistic current can be induced even in the deeply off-resonant regime with two-color linearly polarized light. Consequently, efficient injection of dc-current and the creation of a substantial population imbalance can be realized by employing two-color linearly polarized laser fields with frequencies ω and 2ω, without relying on the ellipticity of light. These findings offer a potential pathway for achieving ultrafast and efficient control of electron population in matter using multi-color linearly polarized light, opening new avenues for exploring the frontiers of quantum dynamics and optoelectronic applications.

3.1 Time-dependent Perturbative Analysis

Time-dependent perturbation theory provides a form for describing the response of quantum systems to time-varying external fields, makes it well-suited for analyzing the interaction of materials with intense electromagnetic radiation. Exploring the photovoltaic effect within the perturbative regime has led to a notable focus on elucidating the injection of dc-current through the use of two-color linearly polarized light [93–99]. Here, we investigate the nonlinear photocarrier

injection process via the time-dependent perturbation analysis. Under adiabatic basis (also named as Houston basis Eq. (2.30) and Eq. (2.33)) representation described in Appendix A, one can rewrite the equation of motion for the coefficient vector $c_{\mathbf{k}}(t)$ after expansion as

$$i\frac{d}{dt}\mathbf{c}_{\mathbf{k}}(t) = \mathcal{H}(t)\mathbf{c}_{\mathbf{k}}(t). \tag{3.1}$$

$$\mathcal{H}(t) = i\mathbf{E}(t)\cdot\begin{pmatrix} 0 & M_{12} \\ M_{21} & 0 \end{pmatrix} \tag{3.2}$$

$$M_{12} = e^{-i\int_0^t dt'\Delta\epsilon_{cv,\mathbf{k}+\mathbf{A}(t')}+i\Delta\phi^g_{cv,\mathbf{k}}(t)}\left\langle u_{v,\mathbf{k}+\mathbf{A}(t)}\middle|\frac{\partial u_{c,\mathbf{k}+\mathbf{A}(t)}}{\partial\mathbf{k}}\right\rangle \tag{3.3}$$

$$M_{21} = e^{-i\int_0^t dt'\Delta\epsilon_{vc,\mathbf{k}+\mathbf{A}(t')}+i\Delta\phi^g_{vc,\mathbf{k}}(t)}\left\langle u_{c,\mathbf{k}+\mathbf{A}(t)}\middle|\frac{\partial u_{v,\mathbf{k}+\mathbf{A}(t)}}{\partial\mathbf{k}}\right\rangle \tag{3.4}$$

$\mathbf{c}_{\mathbf{k}}(t) = \begin{pmatrix} c_{v,\mathbf{k}}(t) \\ c_{c,\mathbf{k}}(t) \end{pmatrix}$ is the coefficient vector, $\Delta\epsilon_{bb',\mathbf{k}+\mathbf{A}(t)}$ is defined by the difference of the single-particle energies as $\epsilon_{b,\mathbf{k}+\mathbf{A}(t)} - \epsilon_{b',\mathbf{k}+\mathbf{A}(t)}$. $|u^H_{bk}(t)\rangle$ is the Houston states are eigenstates of the instantaneous Hamiltonian: $H_{k+eA(t)/\hbar}|u^H_{bk}(t)\rangle = \epsilon_{b,k+eA(t)/\hbar}|u^H_{bk}(t)\rangle$, For simplicity, here assume that the contribution from the geometric phases, $\Delta\phi^g_{cv,\mathbf{k}}(t)$ is zero. Then expand the Hamiltonian in Eq. (3.1) up to the second order of the field $\mathbf{A}(t)$ as

$$\mathcal{H}(t) \approx \mathcal{H}^{(1)}(t) + \mathcal{H}^{(2)}_{dyn}(t) + \mathcal{H}^{(2)}_{dip}(t), \tag{3.5}$$

$$\mathcal{H}^{(1)}(t) = i\mathbf{E}(t)\cdot\begin{pmatrix} 0 & e^{-i\Delta\epsilon_{cv,\mathbf{k}}t}\left\langle u_{v,\mathbf{k}}\middle|\frac{\partial u_{c,\mathbf{k}}}{\partial\mathbf{k}}\right\rangle \\ e^{-i\Delta\epsilon_{vc,\mathbf{k}}t}\left\langle u_{c,\mathbf{k}}\middle|\frac{\partial u_{v,\mathbf{k}}}{\partial\mathbf{k}}\right\rangle & 0 \end{pmatrix}, \tag{3.6}$$

$\mathcal{H}^{(2)}_{dyn}(t)$ originates from the modification of the dynamical phase factor:

$$e^{-i\int_0^t dt' \Delta\epsilon_{vc,\mathbf{k}+\mathbf{A}(t')}} \tag{3.7}$$

$\mathcal{H}^{(2)}_{dyn}(t)$ is given by:

$$\mathcal{H}^{(2)}_{dyn}(t) = \mathbf{E}(t) \cdot \begin{pmatrix} 0 & M_{dyn,12} \\ M_{dyn,21} & 0 \end{pmatrix}, \tag{3.8}$$

$$M_{dyn,12} = \frac{\partial \Delta\epsilon_{cv,\mathbf{k}}}{\partial \mathbf{k}} \cdot \left(\int_0^t dt' \mathbf{A}(t') \right) e^{-i\Delta\epsilon_{cv,\mathbf{k}}t} \left\langle u_{v,\mathbf{k}} \middle| \frac{\partial u_{c,\mathbf{k}}}{\partial \mathbf{k}} \right\rangle \tag{3.9}$$

$$M_{dyn,21} = \frac{\partial \Delta\epsilon_{vc,\mathbf{k}}}{\partial \mathbf{k}} \cdot \left(\int_0^t dt' \mathbf{A}(t') \right) e^{-i\Delta\epsilon_{vc,\mathbf{k}}t} \left\langle u_{c,\mathbf{k}} \middle| \frac{\partial u_{v,\mathbf{k}}}{\partial \mathbf{k}} \right\rangle \tag{3.10}$$

and $\mathcal{H}^{(2)}_{dip}(t)$ originates from the modification of the dipole matrix elements:

$$i \left\langle u_{v,\mathbf{k}+\mathbf{A}(t)} \middle| \frac{\partial u_{c,\mathbf{k}+\mathbf{A}(t)}}{\partial \mathbf{k}} \right\rangle \tag{3.11}$$

$\mathcal{H}^{(2)}_{dip}(t)$ is given by:

$$\mathcal{H}^{(2)}_{dip}(t) = \begin{pmatrix} 0 & M_{dip,12} \\ M_{dip,12} & 0 \end{pmatrix}. \tag{3.12}$$

$$M_{dip,12} = e^{-i\Delta\epsilon_{cv,\mathbf{k}}t} \mathbf{A}(t) \cdot \frac{\partial \left\langle u_{v,\mathbf{k}} \middle| i\mathbf{E}(t) \cdot \frac{\partial u_{c,\mathbf{k}}}{\partial \mathbf{k}} \right\rangle}{\partial \mathbf{k}} \tag{3.13}$$

$$M_{dip,21} = e^{-i\Delta\epsilon_{vc,\mathbf{k}}t} \mathbf{A}(t) \cdot \frac{\partial \left\langle u_{c,\mathbf{k}} \middle| i\mathbf{E}(t) \cdot \frac{\partial u_{v,\mathbf{k}}}{\partial \mathbf{k}} \right\rangle}{\partial \mathbf{k}} \tag{3.14}$$

Hereafter, we analyze the photocarrier injection process based on this perturbative expansion of the Hamiltonian. Use perturbation expansion of Eq. (3.1):

$$i\frac{d}{dt}(\mathbf{c}^{(0)}_{\mathbf{k}}(t) + \mathbf{c}^{(1)}_{\mathbf{k}}(t) + \mathbf{c}^{(2)}_{\mathbf{k}}(t)) = (\mathcal{H}^{(0)}_{\mathbf{k}} + \mathcal{H}^{(1)}_{\mathbf{k}}(t) + \mathcal{H}^{(2)}_{\mathbf{k}}(t))(\mathbf{c}^{(0)}_{\mathbf{k}}(t) + \mathbf{c}^{(1)}_{\mathbf{k}}(t) + \mathbf{c}^{(2)}_{\mathbf{k}}(t)) \tag{3.15}$$

Under initial condition $\mathcal{H}^{(0)}_{\mathbf{k}}(t=0)=0$, $\mathbf{c}^{(0)}_{\mathbf{k}}(t=0)=\begin{pmatrix}1\\0\end{pmatrix}$, the first ($c^{(1)}_{c,\mathbf{k}}(t)$) and second-order coefficient vectors ($c^{(2)}_{c,\mathbf{k},dyn}(t)$, $c^{(2)}_{c,\mathbf{k},dip}(t)$) for the conduction band can be written as:

$$c^{(1)}_{c,\mathbf{k}}(t)=\left\langle u_{c,\mathbf{k}}\middle|\frac{\partial u_{v,\mathbf{k}}}{\partial\mathbf{k}}\right\rangle\int_0^t dt' e^{-i\Delta\epsilon_{vc,\mathbf{k}}t'}\mathbf{E}_1(t') \tag{3.16}$$

$$c^{(2)}_{c,\mathbf{k},dyn}(t)=\frac{1}{i}\frac{\partial\Delta\epsilon_{vc,\mathbf{k}}}{\partial\mathbf{k}}\left\langle u_{c,\mathbf{k}}\middle|\frac{\partial u_{v,\mathbf{k}}}{\partial\mathbf{k}}\right\rangle\int_0^t dt' e^{-i\Delta\epsilon_{vc,\mathbf{k}}t'}\mathbf{E}_2(t')\int_0^{t'} dt''\mathbf{A}_2(t'') \tag{3.17}$$

$$c^{(2)}_{c,\mathbf{k},dip}(t)=\frac{\partial\left\langle u_{c,\mathbf{k}}\middle|\frac{\partial u_{v,\mathbf{k}}}{\partial\mathbf{k}}\right\rangle}{\partial\mathbf{k}}\int_0^t dt' e^{-i\Delta\epsilon_{vc,\mathbf{k}}t'}\mathbf{E}_2(t')\mathbf{A}_2(t') \tag{3.18}$$

Under two-color linearly polarized light, here we consider the perturbation by the external linearly polarized vector potential for $\vec{e}$-direction, assuming T_0 is much larger than the width of the gaussian, and the gaussian can be approximately zero.

$$f(t)=e^{-\frac{(t-T_0)^2}{2\sigma^2}} \tag{3.19}$$

$$\mathbf{A}_1(t)=A_1\vec{e}\cos[2\omega(t-T_0)+\phi]e^{-\frac{(t-T_0)^2}{2\sigma^2}}, \tag{3.20}$$

$$\mathbf{A}_2(t)=A_2\vec{e}\cos[\omega(t-T_0)]e^{-\frac{(t-T_0)^2}{2\sigma^2}} \tag{3.21}$$

w is the carrier frequency of the field, $\vec{e}$ represents a unit vector along the polarization direction of the laser field We assume $\sigma\gg 0$ to make the approximation the Gaussian term is a constant:

$$\int_0^{t'} A_2\vec{e}\cos[\omega(t-T_0)]e^{-\frac{(t-T_0)^2}{2\sigma^2}}dt=\frac{A_2\vec{e}}{\omega}\sin[\omega(t'-T_0)]e^{-\frac{(t'-T_0)^2}{2\sigma^2}} \tag{3.22}$$

The corresponding external dipolar electric field $\mathbf{E}(t)=-d\mathbf{A}(t)/dt$ can be written as the following pulsed form:

$$\mathbf{E}_1(t) = 2\omega A_1 \vec{e}\sin[2\omega(t-T_0)+\phi]e^{-\frac{(t-T_0)^2}{2\sigma^2}}, \tag{3.23}$$

$$\mathbf{E}_2(t) = \omega A_2 \vec{e}\sin[\omega(t-T_0)]e^{-\frac{(t-T_0)^2}{2\sigma^2}} \tag{3.24}$$

Now, let's express this in terms of the first-order coefficient vector is:

$$\begin{aligned} c^{(1)}_{c,\mathbf{k}}(t) &= \left\langle u_{c,\mathbf{k}}\middle|\frac{\partial u_{v,\mathbf{k}}}{\partial \mathbf{k}}\right\rangle \int_0^t dt' e^{-i\Delta\epsilon_{vc,\mathbf{k}}t'} 2\omega A_1 \vec{e}\cdot\sin[2\omega(t'-T_0)+\phi]e^{-\frac{(t'-T_0)^2}{2\sigma^2}} \\ &= \frac{A_1\vec{e}\omega}{i}\left\langle u_{c,\mathbf{k}}\middle|\frac{\partial u_{v,\mathbf{k}}}{\partial \mathbf{k}}\right\rangle \int_0^t dt' e^{-i\Delta\epsilon_{vc,\mathbf{k}}t'-\frac{(t'-T_0)^2}{2\sigma^2}}\cdot(e^{i[2\omega(t'-T_0)+\phi]}-e^{-i[2\omega(t'-T_0)+\phi]}) \end{aligned} \tag{3.25}$$

We consider the population distribution after the laser pulse, so we replace the integra $\int_0^t$ by $\int_{-\infty}^{\infty}$. Under the Gaussian integral,

$$\int_{-\infty}^{\infty} e^{-x^2}\,dx = \sqrt{\pi} \tag{3.26}$$

we get:

$$c^{(1)}_{c,\mathbf{k}}(t) = \frac{A_1\vec{e}\omega\cdot\sigma\sqrt{2\pi}}{i}\left\langle u_{c,\mathbf{k}}\middle|\frac{\partial u_{v,\mathbf{k}}}{\partial \mathbf{k}}\right\rangle \cdot e^{-i\Delta\epsilon_{vc,\mathbf{k}}T_0}[e^{-\frac{1}{2}(\Delta\epsilon_{vc,\mathbf{k}}-2\omega)^2\sigma^2-i\phi}-e^{-\frac{1}{2}(\Delta\epsilon_{vc,\mathbf{k}}+2\omega)^2\sigma^2+i\phi}] \tag{3.27}$$

Similarly to the first-order perturbation coefficient vector's derivation, the second-order coefficient $c^{(2)}_{c,\mathbf{k}}(t)$ can be written as:

$$\begin{aligned} c^{(2)}_{c,\mathbf{k},dyn}(t) =& \frac{(A_2\vec{e})^2\cdot\sigma\sqrt{\pi}}{2i}\frac{\partial\Delta\epsilon_{vc,\mathbf{k}}}{\partial\mathbf{k}}\left\langle u_{c,\mathbf{k}}\middle|\frac{\partial u_{v,\mathbf{k}}}{\partial \mathbf{k}}\right\rangle \cdot e^{-i\Delta\epsilon_{vc,\mathbf{k}}T_0} \\ &\cdot[e^{-\frac{\sigma^2}{4}\Delta\epsilon^2_{vc,\mathbf{k}}}-\frac{1}{2}(e^{-\frac{\sigma^2}{4}(\Delta\epsilon_{vc,\mathbf{k}}-2\omega)^2}+e^{-\frac{\sigma^2}{4}(\Delta\epsilon_{vc,\mathbf{k}}+2\omega)^2})] \end{aligned} \tag{3.28}$$

$$c^{(2)}_{c,\mathbf{k},dip}(t) = \frac{(A_2\vec{e})^2\omega\cdot\sigma\sqrt{\pi}}{4i}\cdot\frac{\partial\left\langle u_{c,\mathbf{k}}\middle|\frac{\partial u_{v,\mathbf{k}}}{\partial \mathbf{k}}\right\rangle}{\partial\mathbf{k}}\cdot e^{-i\Delta\epsilon_{vc,\mathbf{k}}T_0}[e^{-\frac{\sigma^2}{4}(\Delta\epsilon_{vc,\mathbf{k}}-2\omega)^2}-e^{-\frac{\sigma^2}{4}(\Delta\epsilon_{vc,\mathbf{k}}+2\omega)^2})] \tag{3.29}$$

This completes the derivation of the population of the conduction band after the

laser pulse:

$$\begin{aligned}|c_{c,\mathbf{k}}(t)|^2 = &|c^{(1)}_{c,\mathbf{k}}(t)|^2 + |c^{(2)}_{c,\mathbf{k},dyn}(t)|^2 + |c^{(2)}_{c,\mathbf{k},dip}(t)|^2 \\ &+ c^{(1)}_{c,\mathbf{k}}(t)^* c^{(2)}_{c,\mathbf{k},dyn}(t) + c.c. \\ &+ c^{(1)}_{c,\mathbf{k}}(t)^* c^{(2)}_{c,\mathbf{k},dip}(t) + c.c. \\ &+ c^{(2)}_{c,\mathbf{k},dyn}(t)^* c^{(2)}_{c,\mathbf{k},dip}(t) + c.c.\end{aligned} \tag{3.30}$$

$c.c.$ represents complex conjugate. We consider a prototypical two-dimensional insulator, monolayer hexagonal boron-nitride (h-BN). For the 2-band h-BN-tight-binding model, the inversion symmetric is broken

$$u_{\mathbf{k}}(-\vec{r}) \neq u_{-\mathbf{k}}(\vec{r}) \tag{3.31}$$

We apply the time-reversal relation for the derivation:

$$u^*_{\mathbf{k}}(\vec{r}) = u_{-\mathbf{k}}(\vec{r}) \tag{3.32}$$

To compare the $|c_{c,-\mathbf{k}}(t)|^2$, the absolute value of the coefficient becomes:

$$\begin{aligned}|c^{(1)}_{c,\mathbf{k}}(t)|^2 = &|\frac{A_1\vec{e}\omega\cdot\sigma\sqrt{2\pi}}{i}\left\langle u_{c,\mathbf{k}}\middle|\frac{\partial u_{v,\mathbf{k}}}{\partial\mathbf{k}}\right\rangle|^2 \\ &\cdot[e^{-(\Delta\epsilon_{vc,\mathbf{k}}-2\omega)^2\sigma^2} + e^{-(\Delta\epsilon_{vc,\mathbf{k}}+2\omega)^2\sigma^2} - 2e^{-\frac{1}{2}((\Delta\epsilon_{vc,\mathbf{k}}-2\omega)^2\sigma^2+(\Delta\epsilon_{vc,\mathbf{k}}+2\omega)^2\sigma^2)}\cos(2\phi)] \\ &= |c^{(1)}_{c,-\mathbf{k}}(t)|^2\end{aligned} \tag{3.33}$$

$$\begin{aligned}|c^{(2)}_{c,\mathbf{k},dyn}(t)|^2 = &|\frac{(A_2\vec{e})^2\cdot\sigma\sqrt{\pi}}{2}\frac{\partial\Delta\epsilon_{vc,\mathbf{k}}}{\partial\mathbf{k}}\left\langle u_{c,\mathbf{k}}\middle|\frac{\partial u_{v,\mathbf{k}}}{\partial\mathbf{k}}\right\rangle \\ &\cdot[e^{-\frac{\sigma^2}{4}\Delta\epsilon^2_{vc,\mathbf{k}}} - \frac{1}{2}(e^{-\frac{\sigma^2}{4}(\Delta\epsilon_{vc,\mathbf{k}}-2\omega)^2} + e^{-\frac{\sigma^2}{4}(\Delta\epsilon_{vc,\mathbf{k}}+2\omega)^2})]|^2 \\ &= |c^{(2)}_{c,-\mathbf{k},dyn}(t)|^2\end{aligned} \tag{3.34}$$

$$\begin{aligned}|c^{(2)}_{c,\mathbf{k},dip}(t)|^2 = &|\frac{(A_2\vec{e})^2\omega\cdot\sigma\sqrt{\pi}}{4}\cdot\frac{\partial\left\langle u_{c,\mathbf{k}}\middle|\frac{\partial u_{v,\mathbf{k}}}{\partial\mathbf{k}}\right\rangle}{\partial\mathbf{k}}[e^{-\frac{\sigma^2}{4}(\Delta\epsilon_{vc,\mathbf{k}}-2\omega)^2} - e^{-\frac{\sigma^2}{4}(\Delta\epsilon_{vc,\mathbf{k}}+2\omega)^2})]|^2 \\ &= |c^{(2)}_{c,-\mathbf{k},dip}(t)|^2\end{aligned} \tag{3.35}$$

The interference terms are:

$$\begin{aligned} c^{(1)}_{c,\mathbf{k}}(t)^* c^{(2)}_{c,\mathbf{k},dyn}(t) + c.c. = \sqrt{2}A_1 A_2^2 \vec{e}\omega \cdot \sigma^2 \pi \frac{\partial \Delta\epsilon_{vc,\mathbf{k}}}{\partial \mathbf{k}} | \left\langle u_{c,\mathbf{k}} \middle| \frac{\partial u_{v,\mathbf{k}}}{\partial \mathbf{k}} \right\rangle |^2 \\ \cdot [e^{-\frac{\sigma^2}{4}\Delta\epsilon^2_{vc,\mathbf{k}}} - \frac{1}{2}(e^{-\frac{\sigma^2}{4}(\Delta\epsilon_{vc,\mathbf{k}}-2\omega)^2} + e^{-\frac{\sigma^2}{4}(\Delta\epsilon_{vc,\mathbf{k}}+2\omega)^2})] \\ \cdot [e^{-\frac{1}{2}(\Delta\epsilon_{vc,\mathbf{k}}-2\omega)^2\sigma^2} - e^{-\frac{1}{2}(\Delta\epsilon_{vc,\mathbf{k}}+2\omega)^2\sigma^2}] \cos\phi \\ = -(c^{(1)}_{c,-\mathbf{k}}(t)^* c^{(2)}_{c,-\mathbf{k},dyn}(t) + c.c.) \end{aligned} \tag{3.36}$$

$$\begin{aligned} c^{(1)}_{c,\mathbf{k}}(t)^* c^{(2)}_{c,\mathbf{k},dip}(t) + c.c. = \frac{\sqrt{2}A_1 A_2^2 \vec{e}\omega^2 \cdot \sigma^2 \pi}{4} \cdot (e^{-\frac{\sigma^2}{4}(\Delta\epsilon_{vc,\mathbf{k}}-2\omega)^2} - e^{-\frac{\sigma^2}{4}(\Delta\epsilon_{vc,\mathbf{k}}+2\omega)^2}) \\ \cdot (\left\langle \frac{\partial u_{v,\mathbf{k}}}{\partial \mathbf{k}} | u_{c,\mathbf{k}} \right\rangle \frac{\partial \left\langle u_{c,\mathbf{k}} \middle| \frac{\partial u_{v,\mathbf{k}}}{\partial \mathbf{k}} \right\rangle}{\partial \mathbf{k}} [e^{-\frac{1}{2}(\Delta\epsilon_{vc,\mathbf{k}}-2\omega)^2\sigma^2 + i\phi} - e^{-\frac{1}{2}(\Delta\epsilon_{vc,\mathbf{k}}+2\omega)^2\sigma^2 - i\phi}] \\ + \frac{\partial \left\langle \frac{\partial u_{v,\mathbf{k}}}{\partial \mathbf{k}} \middle| u_{c,\mathbf{k}} \right\rangle}{\partial \mathbf{k}} \left\langle u_{c,\mathbf{k}} | \frac{\partial u_{v,\mathbf{k}}}{\partial \mathbf{k}} \right\rangle [e^{-\frac{1}{2}(\Delta\epsilon_{vc,\mathbf{k}}-2\omega)^2\sigma^2 - i\phi} - e^{-\frac{1}{2}(\Delta\epsilon_{vc,\mathbf{k}}+2\omega)^2\sigma^2 + i\phi}]) \end{aligned} \tag{3.37}$$

Here under the time-reversal relation, $u^*_{\mathbf{k}}(\vec{r}) = u_{-\mathbf{k}}(\vec{r})$, so for $-\mathbf{k}$, we have:

$$\left\langle \frac{\partial u_{v,-\mathbf{k}}}{\partial(-\mathbf{k})} | u_{c,-\mathbf{k}} \right\rangle \frac{\partial \left\langle u_{c,-\mathbf{k}} \middle| \frac{\partial u_{v,-\mathbf{k}}}{\partial(-\mathbf{k})} \right\rangle}{\partial -\mathbf{k}} = \left\langle \frac{\partial u^*_{v,\mathbf{k}}}{\partial(-\mathbf{k})} | u^*_{c,\mathbf{k}} \right\rangle \frac{\partial \left\langle u^*_{c,\mathbf{k}} \middle| \frac{\partial u^*_{v,\mathbf{k}}}{\partial(-\mathbf{k})} \right\rangle}{\partial(-\mathbf{k})} \tag{3.38}$$

$$= -\left\langle u_{c,\mathbf{k}} | \frac{\partial u_{v,\mathbf{k}}}{\partial \mathbf{k}} \right\rangle \frac{\partial \left\langle \frac{\partial u_{v,\mathbf{k}}}{\partial \mathbf{k}} \middle| u_{c,\mathbf{k}} \right\rangle}{\partial \mathbf{k}} \tag{3.39}$$

The interference terms for central symmetry point $-\mathbf{k}$ can be written as:

$$\begin{aligned} c^{(1)}_{c,-\mathbf{k}}(t)^* c^{(2)}_{c,-\mathbf{k},dip}(t) + c.c. = \frac{\sqrt{2}A_1 A_2^2 \vec{e}\omega^2 \cdot \sigma^2 \pi}{4} \cdot (e^{-\frac{\sigma^2}{4}(\Delta\epsilon_{vc,\mathbf{k}}-2\omega)^2} - e^{-\frac{\sigma^2}{4}(\Delta\epsilon_{vc,\mathbf{k}}+2\omega)^2}) \\ \cdot (-\left\langle u_{c,\mathbf{k}} | \frac{\partial u_{v,\mathbf{k}}}{\partial \mathbf{k}} \right\rangle \frac{\partial \left\langle \frac{\partial u_{v,\mathbf{k}}}{\partial \mathbf{k}} \middle| u_{c,\mathbf{k}} \right\rangle}{\partial \mathbf{k}} [e^{-\frac{1}{2}(\Delta\epsilon_{vc,\mathbf{k}}-2\omega)^2\sigma^2 + i\phi} - e^{-\frac{1}{2}(\Delta\epsilon_{vc,\mathbf{k}}+2\omega)^2\sigma^2 - i\phi}] \\ - \frac{\partial \left\langle u_{c,\mathbf{k}} \middle| \frac{\partial u_{v,\mathbf{k}}}{\partial \mathbf{k}} \right\rangle}{\partial \mathbf{k}} \left\langle \frac{\partial u_{v,\mathbf{k}}}{\partial \mathbf{k}} | u_{c,\mathbf{k}} \right\rangle [e^{-\frac{1}{2}(\Delta\epsilon_{vc,\mathbf{k}}-2\omega)^2\sigma^2 - i\phi} - e^{-\frac{1}{2}(\Delta\epsilon_{vc,\mathbf{k}}+2\omega)^2\sigma^2 + i\phi}]) \end{aligned} \tag{3.40}$$

$$
\begin{aligned}
c^{(2)}_{c,\mathbf{k},dyn}(t)^* c^{(2)}_{c,\mathbf{k},dip}(t) + c.c. = & \frac{(A_2\vec{e})^4\omega\cdot\sigma^2\pi}{8}\cdot[e^{-\frac{\sigma^2}{4}(\Delta\epsilon_{vc,\mathbf{k}}-2\omega)^2} - e^{-\frac{\sigma^2}{4}(\Delta\epsilon_{vc,\mathbf{k}}+2\omega)^2})] \\
& \cdot[e^{-\frac{\sigma^2}{4}\Delta\epsilon^2_{vc,\mathbf{k}}} - \frac{1}{2}(e^{-\frac{\sigma^2}{4}(\Delta\epsilon_{vc,\mathbf{k}}-2\omega)^2} + e^{-\frac{\sigma^2}{4}(\Delta\epsilon_{vc,\mathbf{k}}+2\omega)^2})] \\
& \cdot\frac{\partial\Delta\epsilon_{vc,\mathbf{k}}}{\partial\mathbf{k}}(\left\langle\frac{\partial u_{v,\mathbf{k}}}{\partial\mathbf{k}}|u_{c,\mathbf{k}}\right\rangle\frac{\partial\left\langle u_{c,\mathbf{k}}\middle|\frac{\partial u_{v,\mathbf{k}}}{\partial\mathbf{k}}\right\rangle}{\partial\mathbf{k}} + \frac{\partial\left\langle\frac{\partial u_{v,\mathbf{k}}}{\partial\mathbf{k}}\middle|u_{c,\mathbf{k}}\right\rangle}{\partial\mathbf{k}}\left\langle u_{c,\mathbf{k}}|\frac{\partial u_{v,\mathbf{k}}}{\partial\mathbf{k}}\right\rangle)
\end{aligned}
\tag{3.41}
$$

$$
\begin{aligned}
c^{(2)}_{c,-\mathbf{k},dyn}(t)^* c^{(2)}_{c,-\mathbf{k},dip}(t) + c.c. = & \frac{(A_2\vec{e})^4\omega\cdot\sigma^2\pi}{8}\cdot[e^{-\frac{\sigma^2}{4}(\Delta\epsilon_{vc,\mathbf{k}}-2\omega)^2} - e^{-\frac{\sigma^2}{4}(\Delta\epsilon_{vc,\mathbf{k}}+2\omega)^2})] \\
& \cdot[e^{-\frac{\sigma^2}{4}\Delta\epsilon^2_{vc,\mathbf{k}}} - \frac{1}{2}(e^{-\frac{\sigma^2}{4}(\Delta\epsilon_{vc,\mathbf{k}}-2\omega)^2} + e^{-\frac{\sigma^2}{4}(\Delta\epsilon_{vc,\mathbf{k}}+2\omega)^2})] \\
& \cdot\frac{\partial\Delta\epsilon_{vc,\mathbf{k}}}{\partial\mathbf{k}}(\left\langle u_{c,\mathbf{k}}|\frac{\partial u_{v,\mathbf{k}}}{\partial\mathbf{k}}\right\rangle\frac{\partial\left\langle\frac{\partial u_{v,\mathbf{k}}}{\partial\mathbf{k}}\middle|u_{c,\mathbf{k}}\right\rangle}{\partial\mathbf{k}} + \frac{\partial\left\langle u_{c,\mathbf{k}}\middle|\frac{\partial u_{v,\mathbf{k}}}{\partial\mathbf{k}}\right\rangle}{\partial\mathbf{k}}\left\langle\frac{\partial u_{v,\mathbf{k}}}{\partial\mathbf{k}}|u_{c,\mathbf{k}}\right\rangle) \\
= & c^{(2)}_{c,\mathbf{k},dyn}(t)^* c^{(2)}_{c,\mathbf{k},dip}(t) + c.c.
\end{aligned}
\tag{3.42}
$$

To summarize the steps, the asymmetric population distribution between $\mathbf{k}$ and $-\mathbf{k}$ can be understood by the quantum interference (QuI) [100] of different excitation paths:

$$
\begin{aligned}
|c_{c,\mathbf{k}}(t)|^2 - |c_{c,-\mathbf{k}}(t)|^2 &= 2c^{(1)}_{c,\mathbf{k}}(t)^* c^{(2)}_{c,\mathbf{k},dyn}(t) + c^{(1)}_{c,\mathbf{k}}(t)^* c^{(2)}_{c,\mathbf{k},dip}(t) - c^{(1)}_{c,-\mathbf{k}}(t)^* c^{(2)}_{c,-\mathbf{k},dip}(t) + c.c. \\
&= 2\sqrt{2}A_1 A_2^2 \vec{e}\omega \cdot \sigma^2 \pi \frac{\partial \Delta\epsilon_{vc,\mathbf{k}}}{\partial \mathbf{k}} | \left\langle u_{c,\mathbf{k}} \middle| \frac{\partial u_{v,\mathbf{k}}}{\partial \mathbf{k}} \right\rangle |^2 \\
&\cdot [e^{-\frac{\sigma^2}{4}\Delta\epsilon^2_{vc,\mathbf{k}}} - \frac{1}{2}(e^{-\frac{\sigma^2}{4}(\Delta\epsilon_{vc,\mathbf{k}}-2\omega)^2} + e^{-\frac{\sigma^2}{4}(\Delta\epsilon_{vc,\mathbf{k}}+2\omega)^2})] \\
&\cdot [e^{-\frac{1}{2}(\Delta\epsilon_{vc,\mathbf{k}}-2\omega)^2\sigma^2} - e^{-\frac{1}{2}(\Delta\epsilon_{vc,\mathbf{k}}+2\omega)^2\sigma^2}] \cos\phi \\
&+ \frac{\sqrt{2}A_1 A_2^2 \vec{e}\omega^2 \cdot \sigma^2 \pi}{2} \cdot (e^{-\frac{\sigma^2}{4}(\Delta\epsilon_{vc,\mathbf{k}}-2\omega)^2} - e^{-\frac{\sigma^2}{4}(\Delta\epsilon_{vc,\mathbf{k}}+2\omega)^2}) \\
&\cdot (\left\langle u_{c,\mathbf{k}} | \frac{\partial u_{v,\mathbf{k}}}{\partial \mathbf{k}} \right\rangle \frac{\partial \left\langle \frac{\partial u_{v,\mathbf{k}}}{\partial \mathbf{k}} \middle| u_{c,\mathbf{k}} \right\rangle}{\partial \mathbf{k}} + \frac{\partial \left\langle u_{c,\mathbf{k}} \middle| \frac{\partial u_{v,\mathbf{k}}}{\partial \mathbf{k}} \right\rangle}{\partial \mathbf{k}} \left\langle \frac{\partial u_{v,\mathbf{k}}}{\partial \mathbf{k}} | u_{c,\mathbf{k}} \right\rangle) \\
&\cdot [e^{-\frac{1}{2}(\Delta\epsilon_{vc,\mathbf{k}}-2\omega)^2\sigma^2} - e^{-\frac{1}{2}(\Delta\epsilon_{vc,\mathbf{k}}+2\omega)^2\sigma^2}] \cos\phi \\
&= \sqrt{2}A_1 A_2^2 \vec{e}\omega \cdot \sigma^2 \pi [e^{-\frac{1}{2}(\Delta\epsilon_{vc,\mathbf{k}}-2\omega)^2\sigma^2} - e^{-\frac{1}{2}(\Delta\epsilon_{vc,\mathbf{k}}+2\omega)^2\sigma^2}] \\
&\cdot [\frac{\partial \Delta\epsilon_{vc,\mathbf{k}}}{\partial \mathbf{k}} | \left\langle u_{c,\mathbf{k}} \middle| \frac{\partial u_{v,\mathbf{k}}}{\partial \mathbf{k}} \right\rangle |^2 (2e^{-\frac{\sigma^2}{4}\Delta\epsilon^2_{vc,\mathbf{k}}} - e^{-\frac{\sigma^2}{4}(\Delta\epsilon_{vc,\mathbf{k}}-2\omega)^2} - e^{-\frac{\sigma^2}{4}(\Delta\epsilon_{vc,\mathbf{k}}+2\omega)^2}) \\
&+ \frac{\omega}{2}(\left\langle u_{c,\mathbf{k}} | \frac{\partial u_{v,\mathbf{k}}}{\partial \mathbf{k}} \right\rangle \frac{\partial \left\langle \frac{\partial u_{v,\mathbf{k}}}{\partial \mathbf{k}} \middle| u_{c,\mathbf{k}} \right\rangle}{\partial \mathbf{k}} + \frac{\partial \left\langle u_{c,\mathbf{k}} \middle| \frac{\partial u_{v,\mathbf{k}}}{\partial \mathbf{k}} \right\rangle}{\partial \mathbf{k}} \left\langle \frac{\partial u_{v,\mathbf{k}}}{\partial \mathbf{k}} | u_{c,\mathbf{k}} \right\rangle) \\
&\cdot (e^{-\frac{1}{4}(\Delta\epsilon_{vc,\mathbf{k}}-2\omega)^2\sigma^2} - e^{-\frac{1}{4}(\Delta\epsilon_{vc,\mathbf{k}}+2\omega)^2\sigma^2})] \cos\phi
\end{aligned}
\tag{3.43}
$$

We consider the band gap between valence and conduction bands close to twice the field's frequency:

$$
\Delta\epsilon_{vc,\mathbf{k}} + 2\omega \approx 0 \tag{3.44}
$$

Because $\sigma \gg 1/\omega$, in a nutshell, the population imbalance becomes:

$$
\begin{aligned}
|c_{c,\mathbf{k}}(t)|^2 - |c_{c,-\mathbf{k}}(t)|^2 \approx \sqrt{2}A_1 A_2^2 \vec{e}\omega \cdot \sigma^2 \pi e^{-\frac{3}{4}(\Delta\epsilon_{vc,\mathbf{k}}+2\omega)^2\sigma^2} [&\frac{\partial \Delta\epsilon_{vc,\mathbf{k}}}{\partial \mathbf{k}} | \left\langle u_{c,\mathbf{k}} \middle| \frac{\partial u_{v,\mathbf{k}}}{\partial \mathbf{k}} \right\rangle |^2 \\
&+ \frac{\omega}{2}(\left\langle u_{c,\mathbf{k}} | \frac{\partial u_{v,\mathbf{k}}}{\partial \mathbf{k}} \right\rangle \frac{\partial \left\langle \frac{\partial u_{v,\mathbf{k}}}{\partial \mathbf{k}} \middle| u_{c,\mathbf{k}} \right\rangle}{\partial \mathbf{k}} + \frac{\partial \left\langle u_{c,\mathbf{k}} \middle| \frac{\partial u_{v,\mathbf{k}}}{\partial \mathbf{k}} \right\rangle}{\partial \mathbf{k}} \left\langle \frac{\partial u_{v,\mathbf{k}}}{\partial \mathbf{k}} | u_{c,\mathbf{k}} \right\rangle)] \cos\phi
\end{aligned}
\tag{3.45}
$$

The utilization of two-color fields, such as ω and 2ω, has opened a potential to break the time-reversal symmetry of the systems, even when the combined field is linearly polarized. This symmetry breaking leads to a population imbalance

induced by laser irradiation, consequently resulting in dc-current injection. The population imbalance in this scheme is caused by quantum interference between two excitation paths: One is the two-photon absorption process with photons at the frequency ω, while the other is the one-photon absorption process with photons at the frequency 2ω. Hence, this protocol for dc-current injection is known as quantum interference control (QuIC). By manipulating the relative phase of the optical fields at frequencies ω and 2ω, QuIC can be applied to achieve control over one- and two-photon absorption processes, often referred to as ($1+2$ QuIC), we will further discuss in the next section.

We need to emphasize the population imbalance of the quantum interference induced by the coupling of two different excitation paths ($1+2$ QuIC), is different from the second order nonlinear current, so-called "injection current" [11]. The injection current occurs due to the quantum interference between absorption pathways associated with orthogonal components of the beam polarization. This leads to a polar distribution of electrons or holes in momentum space, resulting in current injection that temporally follows the optical intensity but whose decay characteristics are related to momentum scattering[11]. One may see that the non-oscillating current due to the quantum interference may exist even after the perturbation ends. Ref.[10] also discussed the interference of one-photon absorption processes associated with different linear polarizations of light for the injection current induced by the circularly polarized light. Furthermore, they discuss the interference of the one - and two-photon absorption processed with the two color laser fields.

3.2 Third-order Nonlinear Regime

From perturbation analysis in Sec 3.1, the breakdown of time-reversal symmetry can be achieved through the use of linearly polarized light featuring two distinct frequencies. This implies that the injection of dc-current and the generation of a substantial population imbalance can be efficiently realized without relying on the ellipticity of light. This principle is exemplified by employing two-color linearly polarized laser fields with frequencies ω and 2ω. In this configuration, the

intrinsic properties of linear polarization and the dual frequencies are sufficient to break time-reversal symmetry, facilitating the desired outcomes of dc-current injection and the establishment of a pronounced population imbalance. This approach provides a adjiustable and simplified means to manipulate quantum interference and achieve specific optical responses in the system without the need for elliptically polarized light.

In the simulations to be presented below, we examine the light-induced electron dynamics in a typical two-dimensional insulator, monolayer h-BN, using a simple tight-binding approximation and TDSE introduced in Chapter 2. In the quantum dynamics simulation, we employ the following expression for the vector potential of the applied two-color fields within the interval $-\frac{\tau}{2} < t < \frac{\tau}{2}$ and zero outside this range:

$$\mathbf{A}(t) = -\mathbf{e}_p \frac{E_0}{\omega} \left[\cos(\omega t) + \frac{1}{4} \cos(2\omega t + \phi) \right] \times \cos^4\left(\frac{\pi}{\tau} t\right) \tag{3.46}$$

$\mathbf{e}_p$ represents a unit vector along the polarization direction of the laser field, E_0 denotes the peak field strength, ω is the fundamental frequency, and τ is the duration of the laser field pulse. To illustrate dc current injection according to perturbation derivation in Section 3.1, we simulate electron dynamics using the vector potential from Eq. (3.49) with ω set to 3 eV for practical calculations. Note that the photon energy satisfies the condition ($\omega \leq E_g \leq 2\hbar\omega$) for the 1+2 QuIC process [94]. Furthermore, we set the laser polarization direction, $\mathbf{e}_p$, with the Γ–K direction, the pulse duration, τ, is set to 40 fs. We introduce a relative phase ϕ between the two-color fields. The relative phase governs quantum interferences among different excitation paths induced via ω and 2ω laser fields, while the global phase is utilized to extract a dc-like response from the quantum dynamics. By manipulating the relative phase ϕ in the electric field described in Eq. (3.47):

$$\mathbf{E}(t) = -\mathbf{e}_p E_0 \left[\cos(\omega t) + \frac{1}{2} \cos(2\omega t + \phi) \right]$$

one can induce a population imbalance and, consequently, a dc-current by extrinsically breaking the time-reversal symmetry by utilizing two-color fields with frequencies ω and 2ω. Figure 3.1 (a) illustrates the electric field generated by the

vector potential with a relative phase of $\phi = 0$, while Figure 3.1 (b) presents the field with a relative phase of $\phi = \pi/2$. It is evident that the field with $\phi = 0$ in Fig. 3.1 (a) breaks the time-reversal symmetry, as $\mathbf{E}(t) \neq \mathbf{E}(-t)$, while the field with $\phi = \pi/2$ in Fig. 3.1 (b) maintains the symmetry $\mathbf{E}(t) = \mathbf{E}(-t)$. Hence, the time-reversal symmetry of the Hamiltonian is broken when $\phi = 0$ and preserved when $\phi = \pi/2$. Consequently, a population imbalance and resulting dc current injection are expected when $\phi = 0$, while symmetric excitation population and the absence of net residual current are anticipated when $\phi = \pi/2$.

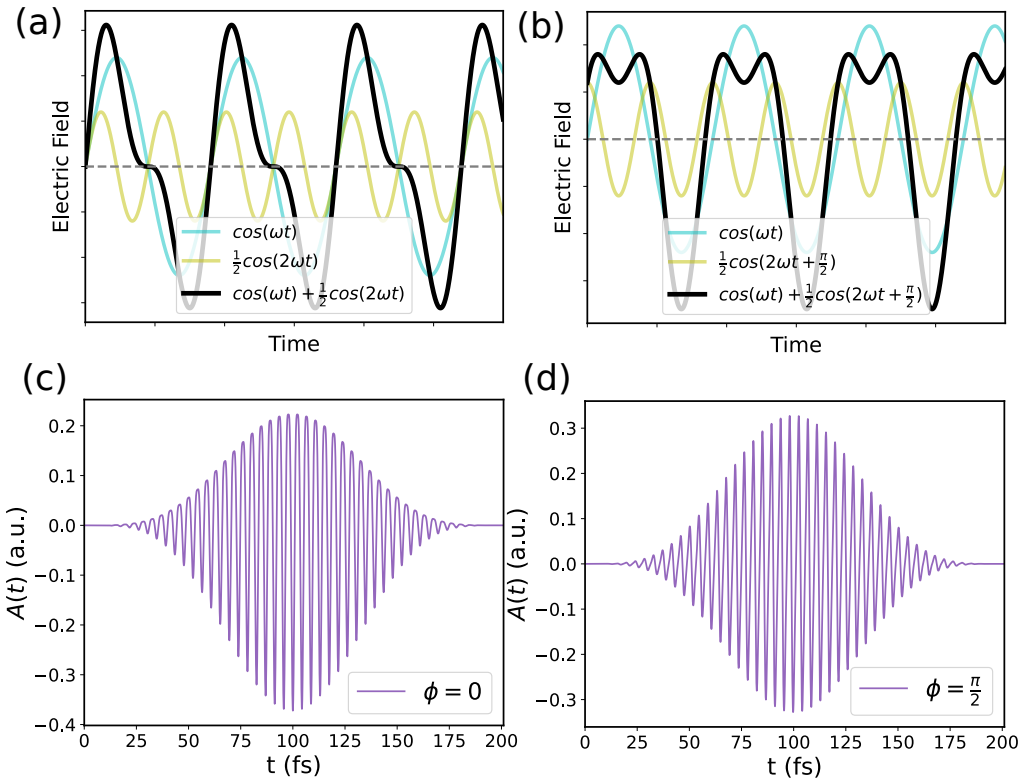

Figure 3.1: The time profiles of the electric field given by Eq. (3.47) are shown for (a) $\phi = 0$ and (b) $\phi = \pi/2$. The corresponding vector potential is shown in (c) $\phi = 0$ and (d) $\phi = \pi/2$.

To comprehensively determine the observed persistent dc-current following laser irradiation, we conduct an in-depth analysis utilizing the photo-excited conduction population $n_{c\mathbf{k}}$ computed from Eq. (2.31):

$$n_{ck} = \left|\langle \phi_{ck} | \psi_k(t_F) \right|^2, \tag{3.47}$$

where t_F is a time after the laser field ends ($t_F > \tau/2$). Employing a weak enough

laser field in the perturbation region with a strength of $E_0 = 2.57$ MV/cm and fixing the relative phase at $\phi = 0$, the resulting conduction population is illustrated in Fig. 3.2 (a). For comparative purposes, Fig. 3.2 (b) presents the conduction population $n_{c\mathbf{k}}$ computed under the same field strength ($E_0 = 2.57$ MV/cm) but with a distinct relative phase ($\phi = 0$). In both instances, the conduction populations exhibit notable excitations centered around the K- and K'-points. This observation implies that the photo-absorption process is primarily governed by a one-photon absorption at the photon energy of $2\hbar\omega$ and a two-photon absorption at the photon energy of $\hbar\omega$. The consistency in the excitation patterns further underscores the dominance of these absorption mechanisms in the system under the specified laser conditions.

While the population distributions in Fig.3.2(a) and (b) may initially appear similar, a closer examination reveals distinctions. In the case of the time-reversal symmetry-broken field ($\phi = 0$) illustrated in Fig.3.2(a), the population distribution must show an imbalance between time-reversal pairs (e.g., $\mathbf{k}$ and $-\mathbf{k}$, or K and K'). On the contrary, in the case of the time-reversal field ($\phi = \pi/2$) showed in Fig.3.2(b), the population distribution $n_{c\mathbf{k}}$ is anticipated to lack such a population imbalance. This discrepancy arises from the absence of a persistent current under these conditions. This analysis deepens our understanding of the complicated relationship between population distributions and the underlying time-reversal symmetry characteristics, providing crucial insights into the dynamic behavior of the system.

To delineate the population imbalance across the Brillouin zone, we introduce the population imbalance distribution $\Delta n_{c\mathbf{k}}$, defined as the disparity in population between the time-reversal pair k-points, expressed as:

$$\Delta n_{c\mathbf{k}} = n_{c\mathbf{k}} - n_{c,-\mathbf{k}} \tag{3.48}$$

Given the constraint $0 \leq n_{c\mathbf{k}} \leq 1$, the population imbalance distribution is bounded by $-1 \leq \Delta n_{c\mathbf{k}} \leq 1$. In situations where external fields maintain time-reversal symmetry, the populations at $\mathbf{k}$ and $-\mathbf{k}$ are equivalent, resulting in a population imbalance distribution of zero. Conversely, in instances where time-reversal symmetry is broken, non-equivalent populations can be induced at $\mathbf{k}$ and $-\mathbf{k}$,

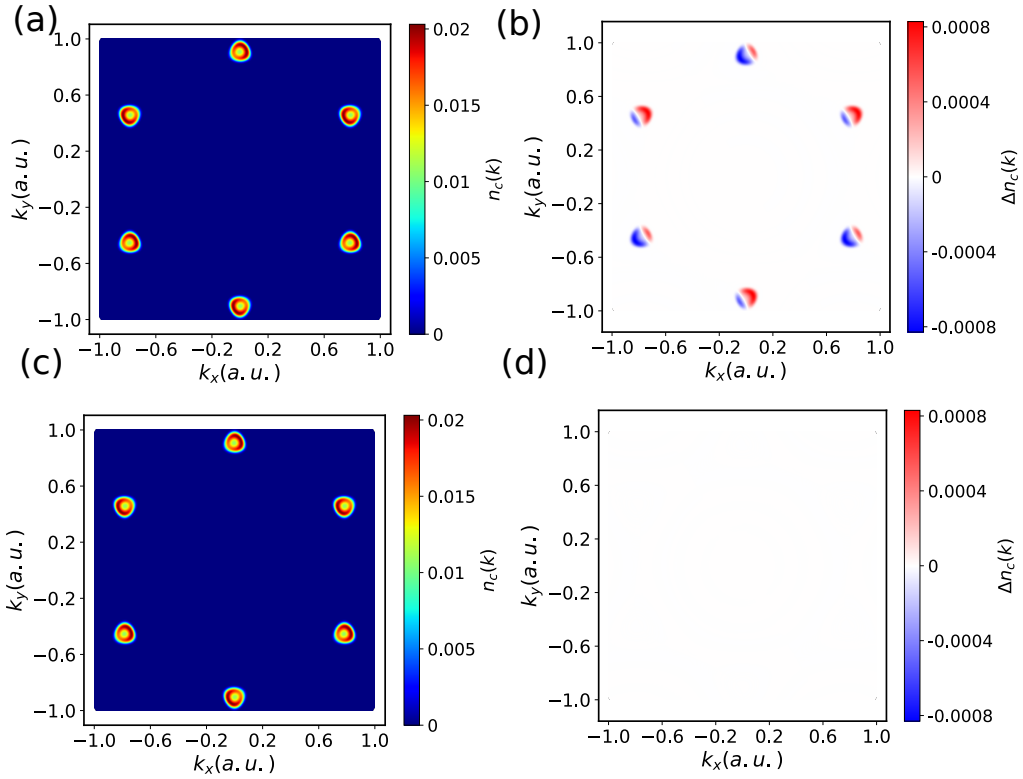

Figure 3.2: (a, b) The conduction population distribution $n_c(\mathbf{k})$ computed with (a) $\phi = 0$ and (b) $\phi = \pi/2$. (c, d) The population imbalance distribution $\Delta n_c(\mathbf{k})$ computed with (c) $\phi = 0$ and (d) $\phi = \pi/2$.

giving rise to a finite population imbalance distribution $\Delta n_{c\mathbf{k}}$. Figures 3.2(c) and (d) illustrate the population imbalance distribution, $\Delta n_{c\mathbf{k}}$, derived from the population distributions presented in Figs.3.2 (a) and (b), respectively. The figures clearly illustrate that when the external field disrupts time-reversal symmetry ($\phi = 0$), a discernible finite population imbalance is induced. In contrast, when the field preserves time-reversal symmetry ($\phi = \pi/2$), the population imbalance diminishes entirely. This comprehensive analysis of the population imbalance distribution provides a detailed insight into the complicated interplay between external field characteristics and the resulting population asymmetry within the Brillouin zone.

The temporal evolution of the corresponding electric current, denoted as $\mathbf{J}_{total}(t)$, can be computed using Eq.(2.27). This equation represents a functional dependence on the vector potential $\mathbf{A}(t)$, as illustrateed in Fig.3.3. The total current encompasses multiple components and noises, often overshadowing the relatively small value of the dc-component following the laser pulse. To examine and isolate the dc-current generated by the fields, we introduce the global phase θ into the fields as described by the Eq.(3.49), as done in our prior study[101].

$$\mathbf{A}(t) = -\mathbf{e}_p \frac{E_0}{\omega} \left[\cos(\omega t + \theta) + \frac{1}{4} \cos(2\omega t + 2\theta + \phi) \right] \times \cos^4\left(\frac{\pi}{\tau} t\right) \tag{3.49}$$

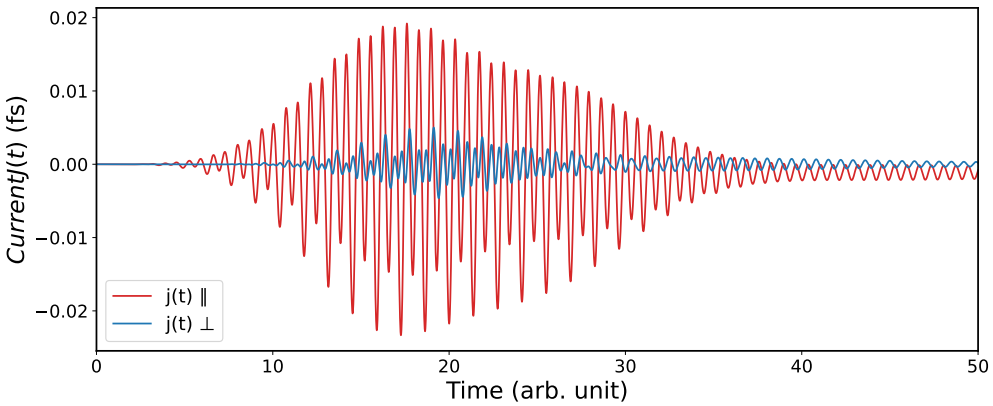

Figure 3.3
The time profiles of the current computed from Eq. (2.27) induced by the electric field given by Eq. (3.47) as shown in Fig. 3.1(a) with relative phase $\phi = 0$.

The current, expressed as a function of the global phase θ in accordance with the vector potential given by Eq.(3.49), is explicitly denoted as $\mathbf{J}(t, \theta)$. By maintain-

ing all laser parameters constant in Eq.(3.49) except for the global phase θ, we can isolate the direct current (dc)-like component of the induced current through the following integral:

$$\mathbf{J}_{\mathrm{dc}}(t) = \frac{1}{2\pi}\int_0^{2\pi} d\theta, \mathbf{J}(t,\theta). \tag{3.50}$$

In this formulation, the integral averages out the higher-frequency components, enabling the extraction of the clean dc-like slow-frequency component of the induced current.

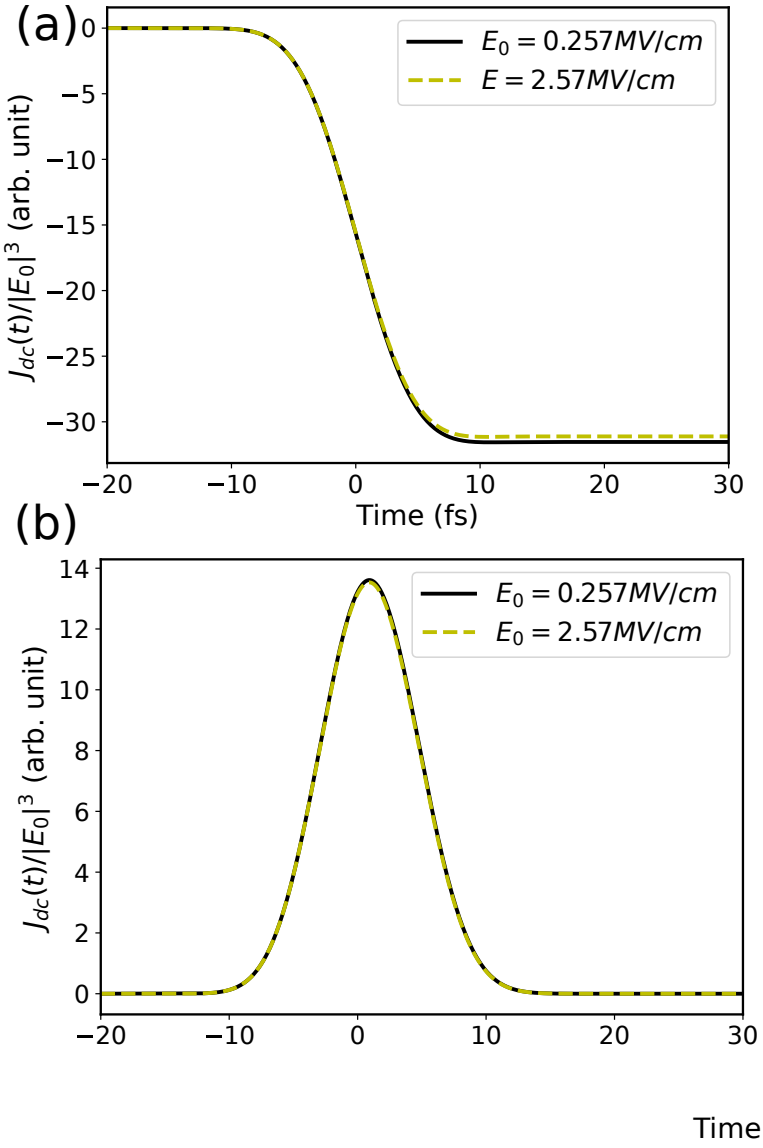

Figure 3.4: The dc components of the currents $\mathbf{J}_{\mathrm{dc}}(t)$ computed from Eq. (3.50) are shown as a function of time. The results using the relative phase of $\phi = 0$ are shown in panel (a), while those using $\phi = \pi/2$ are shown in (b)

In Figure 3.4(a), the calculated dc-current component of the scaled current,

$\mathbf{J}_{\mathrm{dc}}(t)/E_0^3$, is presented for a relative phase of $\phi = 0$, including results for various field strengths, E_0. Remarkably, the residual dc-current persists beyond the conclusion of the laser fields ($t > \tau/2$). Notably, the scaled quantity, $\mathbf{J}\mathrm{dc}(t)/E_0^3$, maintains identical behavior across different field strengths. This consistency suggests that the dc component of the induced current can be interpreted as a third-order nonlinear optical effect. This interpretation aligns with the inherent nature of the 1+2 QuIC process, which involves interference between one- and two-photon absorption processes, classifying it as a third-order nonlinear optical phenomenon. The presented results shed light on the robust and field-independent nature of the observed third-order nonlinear optical effects in the system.

In Figure 3.4(b), the dc-current component of the scaled current, $\mathbf{J}_{\mathrm{dc}}(t)/E_0^3$, is illustrateed with a relative phase of $\phi = \pi/2$. In stark contrast to the results with $\phi = 0$ shown in Fig.3.4(a), the currents in Fig.3.4 (b) do not show a persistent dc component after the conclusion of the laser irradiation. This outcome signifies that the applied field with a relative phase of $\phi = \pi/2$ does not disrupt time-reversal symmetry, and consequently, no population imbalance is induced, resulting in the absence of a sustained current. It is noteworthy that, even in the case of $\phi = \pi/2$, the dc-component of the current is induced solely during the laser irradiation, highlighting yet another instance of a third-order nonlinear optical process. This observation provides further insight into the nuanced interplay between field characteristics and the resulting dynamical responses in the system.

By manipulating the relative phase ϕ, one gains control over the extent of time-reversal symmetry breaking, thereby influencing the resulting population imbalance and dc- current injection [93]. For subsequent analysis, we systematically explore the persistent dc current by varying the relative phase ϕ. Figure 3.5 illustrates the dependence of the dc-current on the relative phase ϕ after laser irradiation, computed using a field with a strength of $E_0 = 2.57$ MV/cm. The amplitude of the induced dc current reaches its maximum when $\phi = 0$ and $\phi = \pi$, with opposite signs for these two phases. Moreover, the induced dc current exhibits continuous variation as the phase ϕ is manipulated, attaining zero when $\phi = \pi/2$ and $\phi = 3\pi/2$, corresponding to the points where the applied fields restore time-reversal symmetry. This straightforward phase dependence aligns with findings from prior works[93, 95], providing further validation of the controllable nature

of the induced dc current through manipulation of the relative phase.

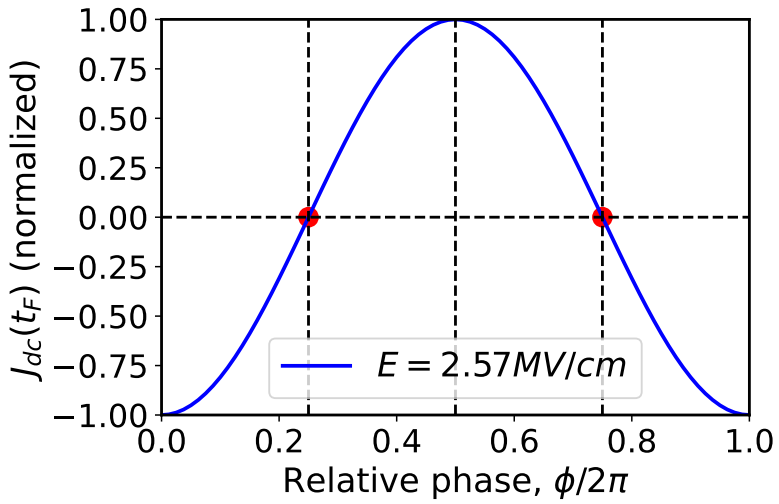

Figure 3.5: The persistent current $J_{\mathrm{dc}}(t_f)$ as a function of the relative phase, ϕ. The results are computed by setting E_0 to 2.57 MV/cm and $\hbar\omega$ to 3 eV.

QuIC processes often exhibit resonance conditions at specific photon energies. By systematically investigating the photon-energy dependence, we can identify resonant regions where the interference effects are significantly enhanced. Investigating these dependencies helps identify the primary mechanisms. To investigate this phenomenon within our theoretical framework, we systematically evaluate the direct current (dc) after laser irradiation by varying the fundamental frequency ω in Eq.(3.49). Figure3.6 (a) illustrates the resulting dc current following laser irradiation with a field strength of $E_0 = 1.03$ MV/m.

According to the expected behavior of the $1+2$ QuIC process, the dc-current decreases when the fundamental photon energy falls below half of the band gap, i.e., $\hbar\omega \leq E_g/2 = 2.95$ eV, since the fundamental photon energy $\hbar\omega$ must adhere to the condition $\hbar\omega \geq E_g/2$, where E_g signifies the band gap. In instances where the fundamental photon energy $\hbar\omega$ falls below the gap, both the $1+2$ QuIC process and the resultant dc-current vanish. This exploration not only clarify the crucial role of photon energy in the indication of the $1+2$ QuIC process but also underscores the significance of satisfying specific conditions for its occurrence and subsequent dc-current induction. This behavior aligns with the expected characteristics of the $1+2$ QuIC process and provides valuable insights into the influence of the fundamental frequency on the induced dc-current in our theo-

retical framework.

Previous results helps understand the complicated relationship between photon energy, field strength, and the nonlinear processes. It is essencial to investigate the photon energy dependence of the dc-current after laser irradiation while varying the field strength, E_0, to unravel the intricacies of this highly nonlinear optical phenomenon. Figures 3.6 (b) and (c) throughly illustrate the photon-energy dependence of the persistent current following laser irradiation, calculated for two distinct field strengths: (b) $E_0 = 51.42$ MV/cm and (c) $E_0 = 102.84$ MV/cm. In contrast to the weak field regime dominated by the $1+2$ QuIC, the direct current (dc) can be induced even under deeply off-resonant conditions, where the photon energy is smaller than half of the band gap ($\hbar\omega \leq E_g/2$), as evident in Figure3.6(b). This convincing observation suggests that potent laser fields introduce additional pathways for electron excitation that extend beyond two-photon absorption. These additional processes, involving multiple photons, contribute to the creation of a population imbalance and a dc-current, even in the deeply off-resonant regime. The interaction between laser field strength and photon energy unveiled in these results provides invaluable insights into the complex dynamics governing persistent currents in strong-field regimes.

Illustrated in Figure 3.6 (c), a noteworthy observation emerges the magnitude of the direct current (dc) after laser irradiation in the deeply off-resonant regime ($\hbar\omega \leq E_g/2$) surpasses that in the $1+2$ QuIC regime ($\hbar\omega \geq E_g/2$) as the applied field strength reaches exceptionally large values. This interesting behavior finds its explanation in the ponderomotive energy, denoted as:

$$U_p = \frac{e^2 E_0^2}{4m\pi\omega_0^2} \tag{3.51}$$

The associated light-induced intraband transitions, both of which are more substantial for lower frequency driving[102]. Consequently, the ensuing nonlinear effects and the injection of dc current become more pronounced in the deeply off-resonant regime compared to the resonant condition. Our initial investigation focused on analyzing the electric current induced by these two-color laser fields within the weak field regime. We confirmed that the dc-component of the induced current persists even after laser irradiation when the fundamental photon

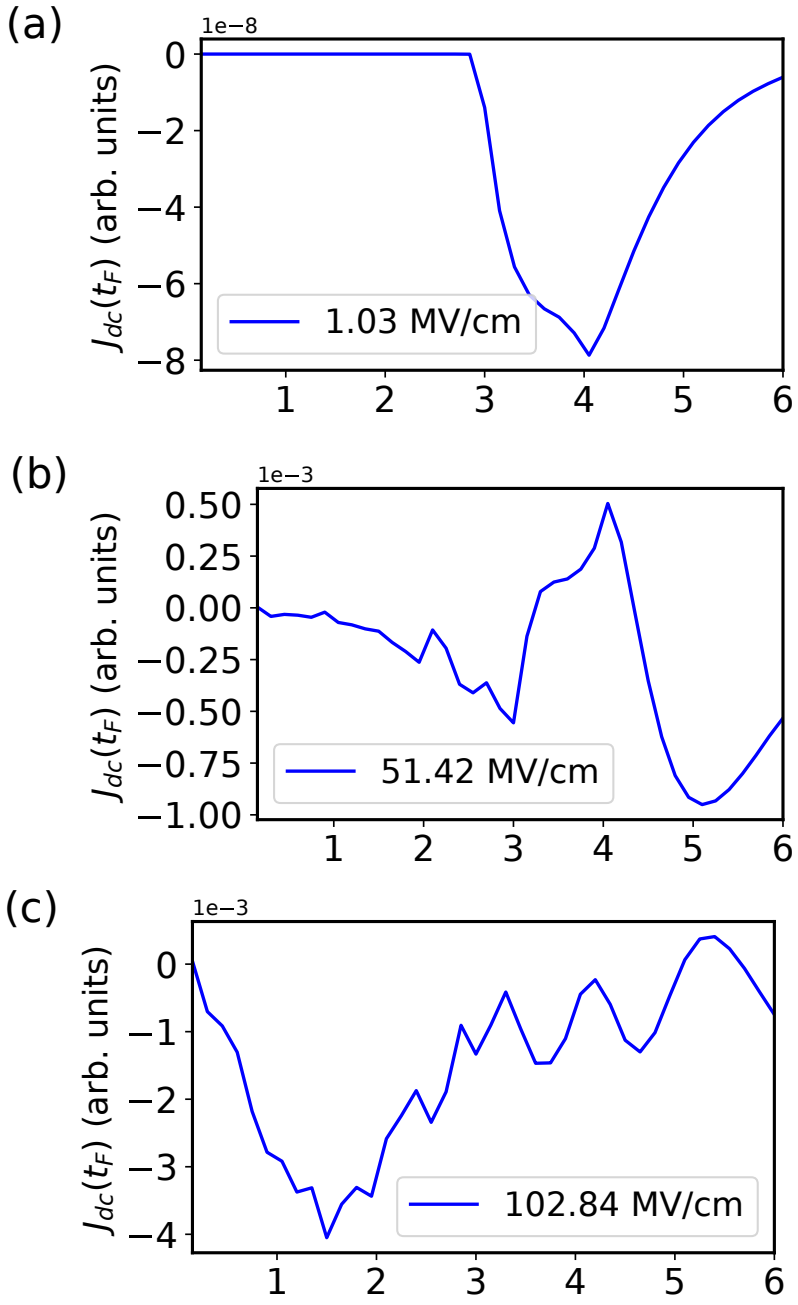

Figure 3.6: The current after the laser irradiation is shown as a function of the fundamental photon energy $\hbar\omega$. The results computed different field strengths: (a) $E_0 = 1.03$ MV/cm, (b) 51.43 MV/cm, and (c) $E_0 = 102.84$ MV/cm.

energy $\hbar\omega$ exceeds the optical gap, $E_g/2$. This ballistic current phenomenon originates from a population imbalance in the Brillouin zone, arising from quantum interference between two distinct excitation paths: one involving one-photon absorption at the photon energy of $2\hbar\omega$, and the other involving a two-photon absorption path at the photon energy of $\hbar\omega$ [93–95].

This discovery sets the stage for a more in-depth exploration of the efficiently inducing dc-current through highly nonlinear optical processes in the deeply off-resonant regime in the next section.

3.3 Deeply Off-resonant Highly-nonlinear Regime

Despite the significant interest in the nonlinear photovoltaic effect, there has been limited exploration of efficient current injection in the deeply off-resonant regime with multi-cycle light pulses, particularly using linearly polarized light. Subsequently, the scope of QuIC can be extended to involve general integer combinations, denoted as $M+N$ QuIC [97, 99]. In this extended scheme, two-color laser fields operating at frequencies ω and ω' induce M- and N-photon absorption processes, respectively. To investigate the mechanism of dc-current injection in the deeply off-resonant regime, as demonstrated in the previous section, we fix the fundamental photon energy $\hbar\omega$ in Eq. (3.49) at 1 eV. Notably, this value is much smaller than half of the band gap, $E_g/2 = 2.95$ eV, for this section.

Similarly, we start with evaluating the population imbalance induced by a strong field in the deeply off-resonant regime, we calculate the population distribution $n_{c\vec{k}}$ after irradiating the laser field with a strength of 100 MV/cm. A distinct pattern emerges in the excited carrier population distribution around the K and K' points. This pattern can be understood through the multi-photon absorption resonances of the light-induced Floquet states[103]. In Fig.3.7(a), we present the computed population distribution in the conduction band. As anticipated from the preceding discussion, the photo-carrier distribution reveals a significant population imbalance between $\mathbf{k}$ and $-\mathbf{k}$ points. To enhance clarity in visualizing the population imbalance, we compute the population imbalance

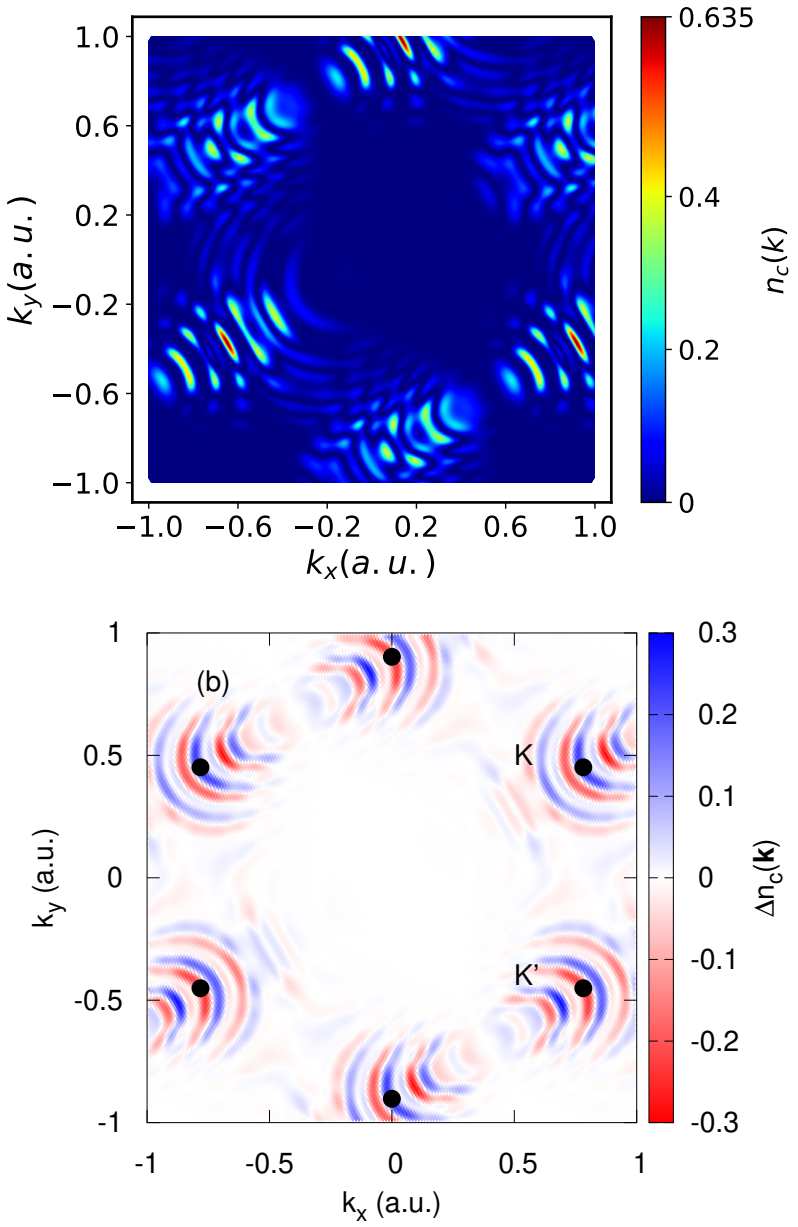

Figure 3.7: (a) The conduction population distribution $n_c(\mathbf{k})$ after the irradiation of the laser field, and (b) the population imbalance distribution $\Delta n_c(\mathbf{k})$ are shown. The results are computed by setting E_0 to 10^{10} V/m.

distribution $\Delta n_{c\mathbf{k}} = n_{c\mathbf{k}} - n_{c,-\mathbf{k}}$. Figure 3.7(b) displays the resulting population imbalance distribution $\Delta n_{c\mathbf{k}}$. Since $\Delta n_{c\mathbf{k}}$ is constrained by $-1 \leq \Delta n_{c\mathbf{k}} \leq 1$, the population imbalance between $\mathbf{k}$ and $-\mathbf{k}$ is maximized when $|\Delta n_{c\mathbf{k}}| = 1$. As observed in Fig.3.7 (b), the population imbalance distribution takes significantly large values, comparable to the maximum values (± 1), across a wide range of the Brillouin zone.

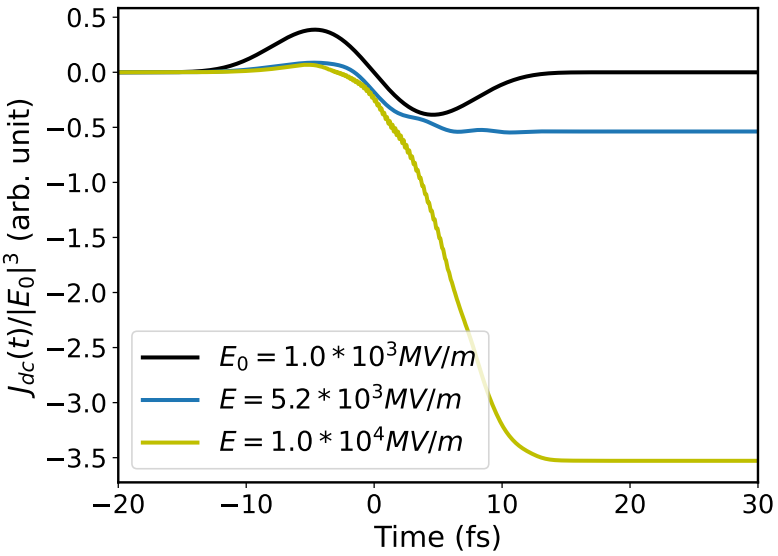

Figure 3.8: The dc components of the currents, $\mathbf{J}_{dc}(t)$, are shown as a function of time. The results are computed with the deeply off-resonant condition, $\hbar\omega = 1.0$ eV.

We calculate the population imbalance ratio r_{im} defined as the maximum absolute value of the population imbalance distribution $\Delta n_{c\mathbf{k}}$ across the Brillouin zone for further qualification. Mathematically, it is expressed as:

$$r_{im} = \frac{\int_{BZ} d\mathbf{k} \left|\Delta n_{c\mathbf{k}}\right|}{\int_{BZ} d\mathbf{k} \left(n_{c\mathbf{k}} + n_{c,-\mathbf{k}}\right)} = \frac{\int_{BZ} d\mathbf{k} \left|\Delta n_{c\mathbf{k}}\right|}{2\int_{BZ} d\mathbf{k} n_{c\mathbf{k}}}. \tag{3.52}$$

The computed imbalance ratio, r_{im}, from Figs.3.7(a) and (b) is about 0.307. Hence, more than 30% of the excited electrons contribute to the population imbalance. This implies the potential for realizing a significant population imbalance through the use of linearly polarized light alone.

In an earlier study [20], significant control over valley population was proposed using bi-circular fields with counter-rotating ω and 2ω two-color laser fields.

In contrast, in this work, we demonstrate that significant valley population can be induced without relying on circular or elliptically polarized light; rather, bi-color linearly polarized light alone can break the time-reversal symmetry and cause such population control.

We commence our analysis of population imbalance by examining the light-induced current in the time domain within the deeply off-resonant regime. In Figure 3.8, we present the dc component of the current, $\mathbf{J}_{\mathrm{dc}}(t)/E_0^3$, computed with varying field strengths, E_0. For this analysis, the relative phase ϕ is set to 0. Evidently, a third-order nonlinear response dominates the induced current in the case of weak field strength. Given that the photon energy of the second harmonic is smaller than the band-gap ($2\hbar\omega < E_g$) and the QuIC process is forbidden, the third-order current returns to zero after the laser irradiation.

However, as the field strength becomes sufficiently strong, the dc-component remains finite even after laser irradiation, as illustrateed in Fig. 3.8. This observation suggests that a higher-order nonlinear process contributes to the ballistic dc-current injection beyond the third-order nonlinear effect.

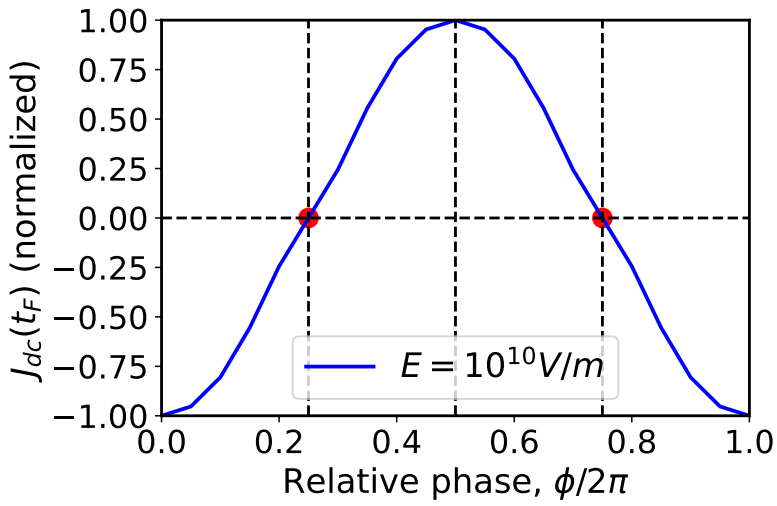

Figure 3.9: The persistent current, $J_{dc}(t_f)$, is shown as a function of the relative phase ϕ. The results are computed with the deeply off-resonant condition, $\hbar\omega = 1.0$ eV.

Next, we explore the dependence of the ballistic current induced by deeply off-resonant light on the relative phase, ϕ. Figure 3.9 illustrates the computed current as a function of the relative phase, ϕ, with calculations conducted at a

field strength of $E_0 = 1 \times 10^4$ MV/m. In accordance with the QuIC case shown in Fig.3.5, the persistent current is maximized when the relative phase is $\phi = 0$ or $\phi = \pi$, and it vanishes when the applied field exhibits time-reversal symmetry ($\phi = \pi/2$ or $\phi = 3\pi/2$). Therefore, even in the deeply off-resonant regime, the direction and magnitude of the persistent current can be controlled by manipulating the relative phase ϕ between the two-color fields at frequencies ω and 2ω.

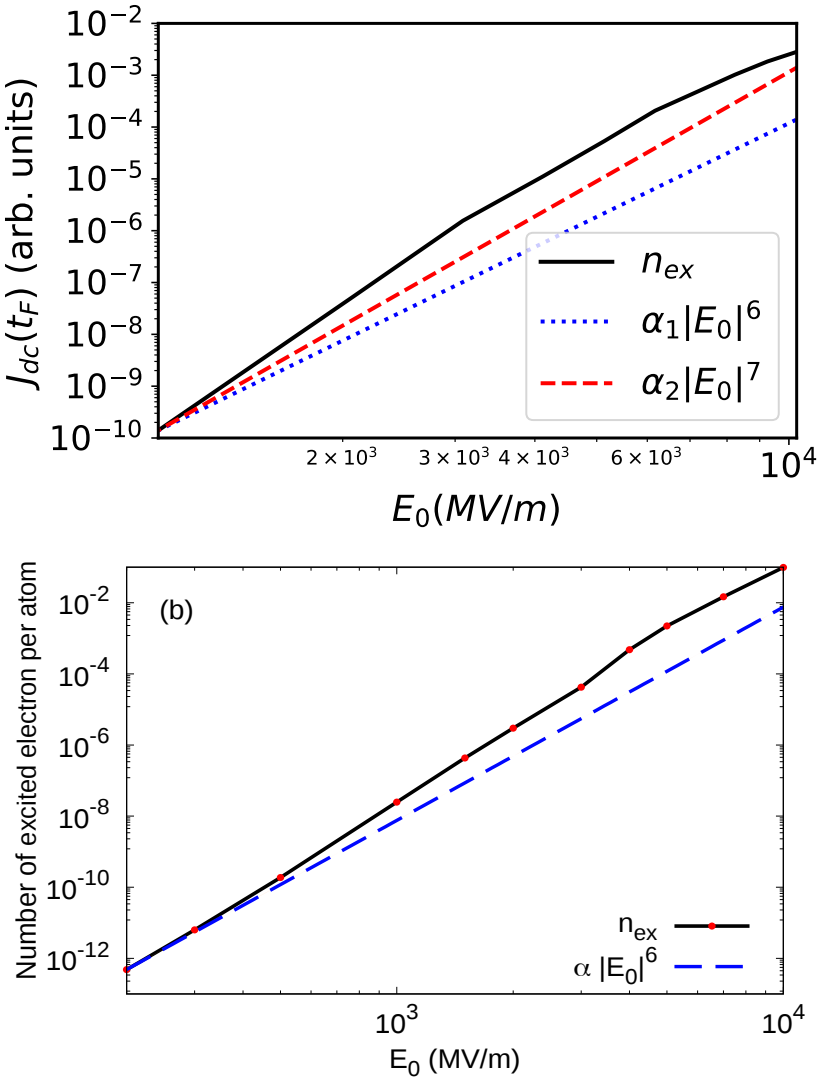

Figure 3.10: (a) The persistent current, $|J_{dc}(t_f)|$, is shown as a function of the field strength, E_0. (b) The number of conduction population after the laser irradiation is shown as a function of the field strength E_0.

To gain a more detailed understanding of the complicated mechanism behind dc current injection in the deeply off-resonant regime, we study into an analysis

of how the injected current scales with the applied field strength E_0. As illustrateed in Figure 3.10, the current amplitude after laser irradiation is plotted against the varying field strength. Notably, a reference line representing $|E_0|^7$ is included for comparison.

The compelling observation from the figure is that the induced current exhibits a clear proportionality to $|E_0|^7$ in the weak field regime. This insightful finding suggests that the seventh-order nonlinear process takes precedence in governing the dynamics of dc current injection under these conditions. This nuanced understanding provides a comprehensive insight into the complicated nonlinear optical processes that contribute to the observed dc current phenomena in the deeply off-resonant regime.

The observed scaling law of the induced dc current with the applied field strength might initially seem inconsistent with the expected behavior of a straightforward $M + N$ QuIC process. In the conventional $M + N$ QuIC situation, the M-photon absorption process is initiated by light with frequency ω, and the N-photon absorption process is generated by light with frequency 2ω, resulting in an overall $(M + N)$-th order nonlinear process. For instance, if we consider a six-photon process for multi-photon absorption with light of frequency ω and a three-photon process for light of frequency 2ω, the anticipated simple $M+N$ QuIC process corresponds to the ninth-order nonlinear process ($M + N = 6 + 3 = 9$).

However, our experimental observations reveal a scaling that indicates seventh-order nonlinearity instead. This apparent discrepancy in the observed and expected nonlinearities of the injected dc current can be rationalized by the presence of an additional excitation channel involving a four-photon absorption process. In this situation, two photons at frequency ω and the other two photons at frequency 2ω combine to excite electrons. This additional four-photon excitation channel interferes with the three-photon absorption process at the photon energy of $2\hbar\omega$, resulting in seventh-order ($7 = 3 + 4$) nonlinear current injection.

To study deeper into the nonlinearity of the light-induced electron dynamics, we performed computations to determine the number of photo-excited carriers

after laser irradiation using the expression:

$$N_{ex} = \frac{2}{A_{\mathrm{BZ}}} \int_{\mathrm{BZ}} d\mathbf{k} n_{c,\mathbf{k}}, \tag{3.53}$$

where $A_{\mathrm{BZ}} = \int_{\mathrm{BZ}} d\mathbf{k}$ represents the area of the Brillouin zone.

Figure 3.10 (b) presents the number of excited electrons as a function of the field strength, E_0, alongside a reference line proportional to $|E_0|^6$. In the weak field regime, the number of excited electrons exhibits proportionality to $|E_0|^6$, highlighting the dominance of the three-photon absorption process in the excitation mechanism. However, as the field strength increases, the deviation from the three-photon absorption line suggests the initiation of a nonperturbative mechanism in the excitation process.

In contrast to the $|E_0|^6$-dependence of the number of photo-excited carriers in the weak field regime, the injected current and the corresponding population imbalance follow a $|E_0|^7$ scaling, as illustrateed in Figure 3.10 (a). The difference in nonlinearities between the absolute photo-carrier population and the population imbalance implies that the population imbalance is negligible concerning the absolute photo-carrier population in the weak field regime. However, in a strong field regime, the relative significance of the population imbalance becomes substantial as it grows more rapidly than the absolute photo-carrier population. Therefore, the distinction in nonlinearities between the total photocarrier population and the population imbalance indicates the potential for large-amplitude valley carrier population control.

Expanding our analysis to the deeply off-resonant regime, where $\hbar\omega \ll E_g/2$, we observed an absence of population imbalance under weak field strength. However, as the field strength increased, a population imbalance in the Brillouin zone is formed, leading to the injection of the persistent dc-current after the laser irradiation. Scaling analysis of the ballistic current injection with respect to the applied field strength E_0 revealed that the population imbalance and the ballistic current result from an interference between three-photon absorption process with three photons of energy $2\hbar\omega$ and a four-photon absorption process with two photons of energy $2\hbar\omega$ and two photons of energy $\hbar\omega$. Consequently, we demonstrated that a multi-photon absorption process, incorporating photons with dif-

ferent energies, plays a pivotal role in addition to the multi-photon absorption process involving single-color photons.

In previous works [22, 88], the formation of substantial population imbalance and valley-population control has been discussed in monolayer systems such as monolayer h-BN and graphene, using bi-circular laser fields with frequencies ω and 2ω. Recently, valley-population control with bi-circular fields has been extended to multi-layer and bulk systems [104] without relying on intrinsic inversion symmetry breaking and the Berry curvature at the valleys. In contrast to these works, our study demonstrates the induction of a large population imbalance and ballistic current injection without relying on the ellipticity of light. Instead, we rely on time-reversal symmetry breaking achieved through relative phase control between two-color linearly-polarized fields at frequencies ω and 2ω. Furthermore, similar to Ref. [104], the injection mechanism with bi-color linearly polarized light does not rely on intrinsic inversion symmetry breaking, indicating an efficient dc current injection and population control with the scheme using linearly-polarized light. The potential of population control and the photovoltaic effect with linearly polarized light, in addition to circularly/elliptically polarized light, unveils novel avenues for realizing ultrafast opto-electronics, marked by precise control of current and population dynamics on the femtosecond time scale.

This page is intentionally left blank.

Chapter 4

THZ-INDUCED HHG AND NONLINEWAR CHARGE TRANSPORT

The discussion and results presented in this chapter ar an adaptation of the article Ref. ([105]) [Wenwen Mao *et al.*, THz-induced high-order harmonic generation and nonlinear transport in graphene. (2022) *Phys. Rev. B* **106**, 024313]

Recent experimental work conducted by Yoshikawa in Ref. [106] nicely show the enhancement of HHG by elliptically polarized light, strongly indicating that the solid-state HHG is completely different from the gas-phase HHG because the HHG from gas is reduced by increasing the elliptically polarized light. Later, experiments on the THz high-harmonic generation in graphene sample with electrical tunability of terahertz nonlinearity in graphene [107, 108], In their experimental setup, the gated graphene sample device, in which the graphene film acts as a channel between source and drain electrodes subjected to a constant potential difference of 0.2 mV. The graphene film is covered on top by an electrolyte subjected to a varying gating voltage to tune the Fermi level of the graphene layer [108], showing extremely efficeint HHG spectrum intensty controled by Fermi Level shifting. It would be interesting to theoretically study nonequilibrium electron dynamics to understand the mechanism of HHG in graphene in THz regime with a shifted Fermi level. However, the microscopic understanding of these HHG is not clear yet, and thus you peform the microscopic electron dynamcis simulation by considering nonequilibrium aspects of the phenomena. Meanwhile,

HHG induced by intense laser fields has strong relaxation which cannot be ignored. These all require for the study of HHG phenomena and the prediction of experimental observables in more realistic conditions, so we introduce the quantum master equation for HHG progress under intensed long-term pulses.

THz-induced transparency of graphene, an interesting nonlinear optical effect, has been explored [109–111], often analyzed through a thermodynamic model emphasizing the reduction of electric conductivity [76, 108]. Despite these advancements, a comprehensive understanding of the microscopic mechanisms controlling these nonlinear effects remains tricky. The existing studies predominantly rely on thermodynamic models, lacking a thorough exploration of nonequilibrium quantum dynamics under dissipation. This research gap highlights the need for a deeper exploration of the underlying microscopic processes to unravel the intricacies of HHG and related nonlinear optical effects in graphene.

In this chapter, we investigate into the complex details of THz-induced HHG and nonlinear electric transport in graphene. Our approach involves utilizing the quantum master equation with the relaxation time approximation to provide a comprehensive understanding of the underlying phenomena in Chapter. (2.3.2). To gain microscopic insights, we thoroughly compare the outcomes of fully dynamic calculations with those obtained through a quasi-static approximation, the electronic system is treated as a nonequilibrium steady state.

The key revelation from our investigation is that the THz-induced electron dynamics in graphene can be accurately represented by the nonequilibrium steady-state approach at each moment in time. Through a thorough population distribution analysis, we clarify that THz-induced HHG in graphene arises from the reduction of effective conductivity, attributed to a significant displacement of electrons in the Brillouin zone.

To deepen our understanding, we draw comparisons between the nonequilibrium picture presented here and a thermodynamic perspective. This comparative analysis allows us to unravel the central role of the nonequilibrium nature of electron dynamics in driving the extremely nonlinear optical and transport phenomena observed in graphene. Our study contributes valuable insights into

the complex interplay between THz fields, electron dynamics, and nonlinear behavior in graphene systems.

The comprehensive dynamical analysis derived from the quantum master equation provides a natural framework for understanding the complex nonequilibrium features inherent in field-induced phenomena. Specifically, it allows for the exploration of phenomena characterized by symmetry breaking and delayed responses, uncovering the dynamics of the system under the influence of external fields. Ongoing theoretical investigations aim to investigate deeper into these aspects, explaining the nonequilibrium behavior induced by light-matter interactions.

4.1 Fully Dynamical Simulations for THz Field

In this section, we first give a brief introduction of recent Experiments and Thermodynamic model on graphene. Next we investigate into the microscopic intricacies controlling the THz-induced HHG in graphene, the electronic structure is discriped by the tight-binding model in Chapter2. We initiate our investigation by conducting a detailed electron dynamics simulation using TDSE,Eq. (2.32). The focus of this simulation is to analyze the HHG in graphene under the influence of a linearly polarized laser pulse. To promote this analysis, we adopt a specific form for the applied vector potential, described by the equation:

$$\mathbf{A}(t) = -\frac{E_0}{\omega_0}\mathbf{e}_\mathbf{x}\sin(\omega_0 t)\cos^4\left(\frac{\pi}{T_{\text{full}}}t\right), \tag{4.1}$$

where the simulation is conducted in the domain $-T_{\text{full}}/2 < t < T_{\text{full}}/2$ and is zero outside this period. Aligning with a previous experimental setup [112], we set specific parameters for the pulse: the peak field strength E_0 is chosen as 8.5 MV/m, the mean photon energy $\hbar\omega_0$ is set to 1.2407 meV, and the pulse duration T_{full} is established as 40 ps. Notably, the direction of the electric field $\mathbf{e}_x$ is defined along the Γ–M direction.

This detailed setup enables a thorough exploration of the electron dynamics under the influence of the specified laser pulse parameters, laying the groundwork for a comprehensive analysis of high-order harmonic generation in graphene.

Following the electron dynamics simulation governed by the field in Eq. (5.3), solve the quantum master euation in Eq. (2.32) with the vector potential given above, we obtain the time-dependent density matrix. Then we proceed to compute the induced electric current, denoted as $\mathbf{J}(t)$ given by Eq. (2.38). To unveil the frequency content embedded within the current dynamics, we employ a Fourier transform applied to the current, yielding the high-order harmonics spectrum described by the expression:

$$I_{\text{HHG}}(\omega) \sim \omega^2 \left| \int_{-\infty}^{\infty} dt, J(t), e^{i\omega t} \right|^2 . \tag{4.2}$$

Here, $I_{\text{HHG}}(\omega)$ encapsulates the contribution of high-order harmonics, and the spectrum is determined by the square of the magnitude of the Fourier transform of the induced current. This approach enables us to discern and analyze the harmonic content within the electric current, providing valuable insights into the high-order harmonic generation phenomenon induced by the specified laser pulse.

Figure. 4.1.(a) we first show the computed current induced by THz field from Eq. (2.38) and the corresponding high-order harmonic spectrum $I_{\text{HHG}}(\omega)$ in Fig. 4.1.(b) to compare the results with and without dissipation. The blue curves are computed by setting T_1 and T_2 to infinity $+\infty$, so the relaxation operation term in Eq. (2.36) with approach zero, and the computed total currents from Eq. (2.38) will be equivalent to the current in Eq. (2.27) solving from TDSE in Eq. (2.21). The red curves are computed with finite $T_1 = 100fs$ and $T_2 = 20fs$ values as introduced in the master equation section 2.3.2, by setting the chemical potential $\mu = 0.17eV$. The compared results show that the total currents and HHG signal intensities are significantly suppressed with the inclusion of dissipation, due to losing energy form the system to the environment, indicating the importance of considering relaxation processes in THz-induced nonlinear phenomena in graphene.

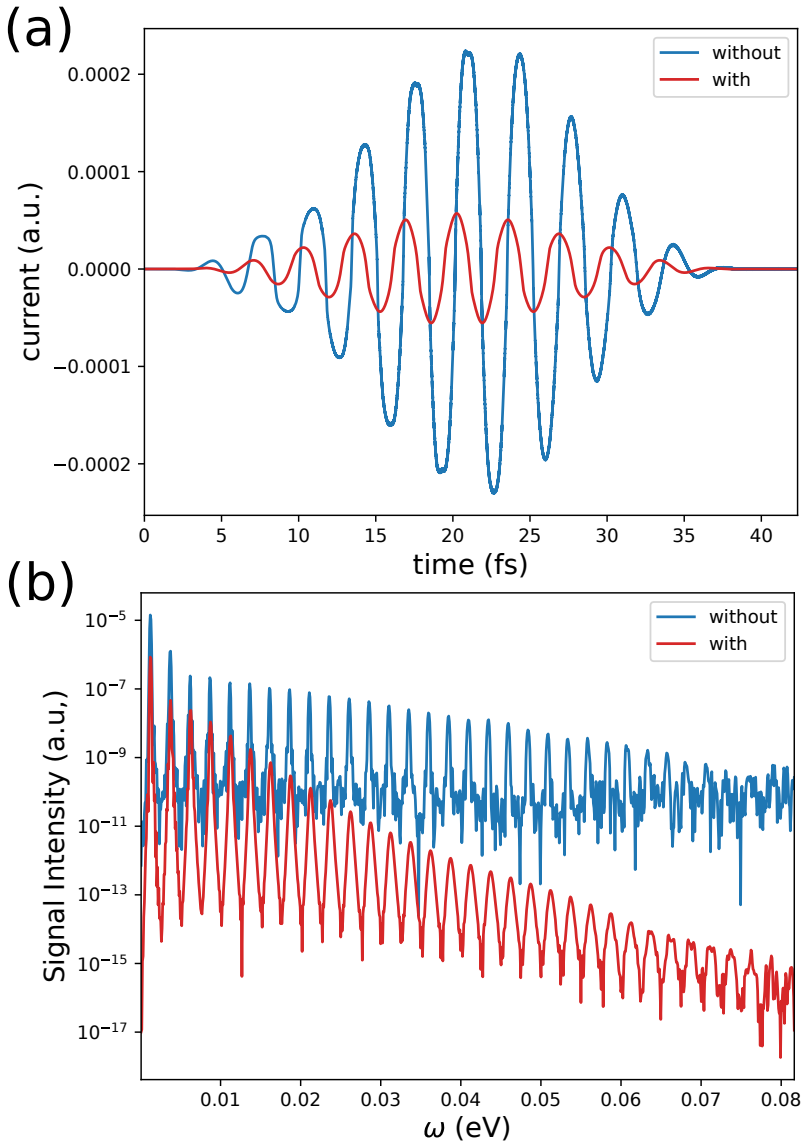

Figure 4.1: (a). Compared total currents with Eq. (2.38) with (red curve) and without (blue curve) relaxation approximation in master equation in Eq. (2.32), by setting the eletron temperature $T_e = 300K$ and Fermi level $\mu = 0.17eV$. Compared harmonic spectra $I_{\mathrm{HHG}}(\omega)$ with Eq. (4.2) from the cuurents in (a) with (red curve) and without (blue curve) relaxation approximation.

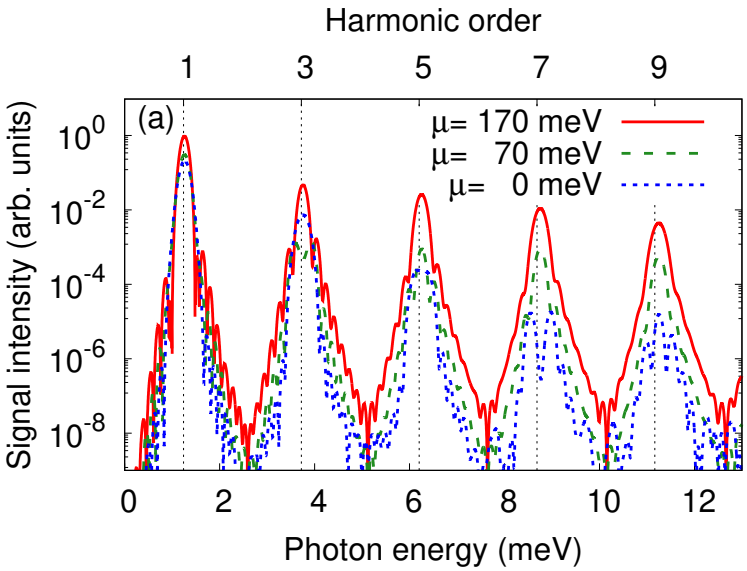

Figure 4.2: Computed harmonic spectra $I_{\mathrm{HHG}}(\omega)$ with Eq. (4.2) for different chemical potentials, $\mu = 0$, 70 and 170 meV. Figure is reproduced with permission from ref. ([113]). Copyright 2022, Phys. Rev. B.

In Figure 4.2, we present the computed HHG spectra, denoted as $I_{\mathrm{HHG}}(\omega)$, corresponding to different chemical potentials μ. Each chemical potential yields distinct harmonic peaks, and a noticeable trend emerges: the intensities of the induced harmonics systematically increase with the rise in the chemical potential. This observation combines with findings from a recent experiment [108], where an analogous increase in induced harmonic intensity was noted with an elevation in gate voltage.

The observed trends in harmonic spectra intensities presented here depending on the chemical potential increasing reproduce the results from former research, such as [76], where THz-induced high-order harmonic generation in graphene was clarifyd through a thermodynamic framework. In contrast, our current study aims to advance the understanding of these THz-induced nonlinear phenomena by considering a comprehensive microscopic perspective. Specifically, we investigate into the nonequilibrium nature of electron dynamics to process our description of light-matter interactions and provide a more interpretation of the observed trends in high-order harmonic spectra with varying chemical potentials.

Following the electron dynamics calculations under THz fields, our findings reveal that the induced harmonics experience enhancement with an increase in

chemical potential. This theoretical insight combines with recent experimental observations, where high-order harmonic generation is similarly enhanced through the application of a gate bias voltage [108].

4.2 Quasi-static Approximation

Subsequently, we introduce a quasi-static approximation to investigate the THz-induced nonperturbative electron dynamics, halping a reexamination of the nonlinear electric transport and the field-induced transparency phenomena inherent to graphene [90]. In our analysis, we make the assumption that the variation of the THz field is sufficiently slow, allowing the electronic system to be effectively characterized by a nonequilibrium steady state at each point in time. This assumption holds true under the equilibrium established between the field-induced excitation and relaxation processes. Its accuracy is particularly pronounced when the mean frequency of the THz field is significantly smaller than the essential relaxation rates, denoted as $1/T_1$ and $1/T_2$.

For practical considerations within the quasi-static approximation, we initiate our analysis by evaluating the electric current of a nonequilibrium steady state under a static electric field, represented as $\mathbf{E}(t) = E_0\mathbf{e}_x$. The corresponding expression is given by:

$$\mathbf{J}_S(E_0) = \lim_{t\to\infty} \frac{2}{(2\pi)^2} \int d\mathbf{k} \mathrm{Tr}\left[\hat{J}k(t)\rho k(t)\right]. \tag{4.3}$$

In this equation, the electron dynamics are computed under a static field, $\mathbf{A}(t) = -E_0\mathbf{e}_x t$. Over time, the electronic system obtains a nonequilibrium steady state as a result of the equilibrium between field-induced excitation and relaxation processes.

Within the quasi-static approximation, we raplace the instantaneous electric field in the induced current $\mathbf{J}(t)$ with the steady current $\mathbf{J}_S(E_0)$ from Eq. (4.3), resulting in the approximation:

$$\mathbf{J}(t) \approx \mathbf{J}_S\left(\mathbf{E}(t)\right). \tag{4.4}$$

To evaluate the validity of this approximation, we first look into the steady current in Eq.(4.3) for various field strengths. For practical computations, we analyze the electron dynamics under a static electric field, denoted as $\mathbf{E}_0 = E_0\mathbf{e}_x$. Figure4.3 illustrates the computed current as a function of time under a static field. In this simulation, the chemical potential μ is set to 170 meV, and the field strength E_0 is established at 8.5 MV/m. The initial state at $t = 0$ corresponds to the thermal equilibrium state.

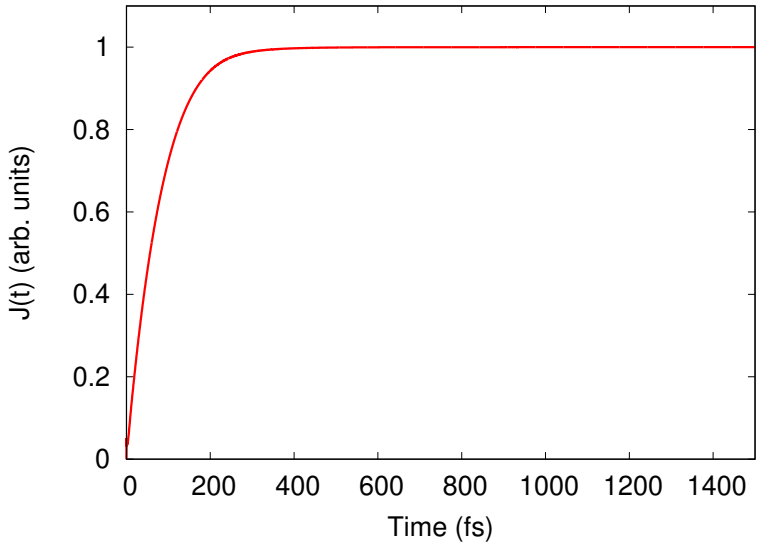

Figure 4.3: Electric current in graphene under a static electric field, $E_0 = 8.5$ MV/m. Figure is reproduced with permission from ref. ([113]). Copyright 2022, Phys. Rev. B.

As observed in Fig.4.3, the application of the electric field induces an electric current at $t = 0$, and it steadily approaches the steady-state value, denoted as $\mathbf{J}_S(E_0)$. This observation confirms that the electronic system, evolving under Eq.(2.32) with a static electric field, eventually reaches a nonequilibrium steady state after a sufficiently extended period of time propagation. This validation supports the reliability of the quasi-static approximation in capturing the nonequilibrium dynamics induced by a slowly varying electric field.

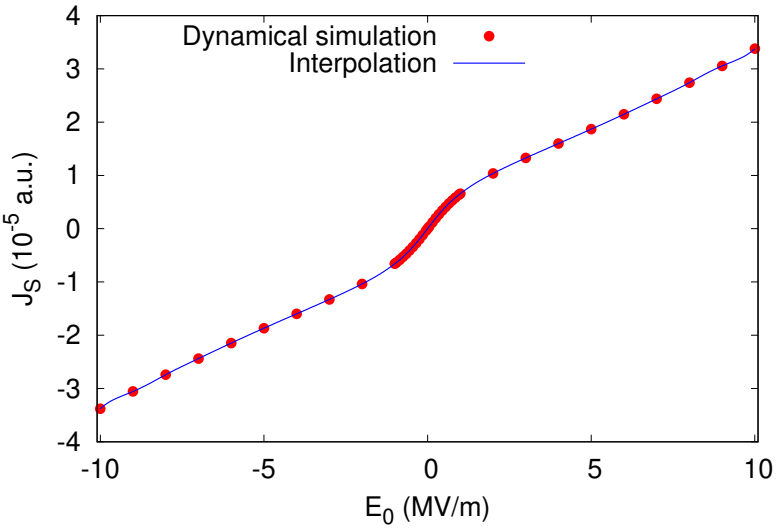

Figure 4.4: Steady current $\mathbf{J}_S(E_0)$ as a function of field strength E_0. The results of the fully dynamical calculation are showns as the red points, while the interpolated result is shown as the blue-solid line. Figure is reproduced with permission from ref. ([113]). Copyright 2022, Phys. Rev. B.

In our practical simulations, we systematically vary the field strength E_0 and evaluate the resulting values of the steady current. Denoting the kth set of employed field strength and evaluated current as E_k and $\mathbf{J}_k$ respectively, we represent the computed steady current $\mathbf{J}_k$ as red points in Figure 4.4 against the applied field strength E_k. To construct a continuous function $\mathbf{J}_S(E_0)$ from the discrete data points $E_k, \mathbf{J}_k$ in Figure 4.4, we adopt a two-step interpolation procedure.

In the first step of constructing the continuous function, we employ a polynomial regression with the following odd function:

$$\mathbf{J}_{\text{polynomials}}(E_0) = \sum j = 0^4 \mathbf{e}_x \alpha^{(2j+1)} E_0^{2j+1}, \tag{4.5}$$

where $\alpha^{(j)}$ represents optimization parameters. These parameters are fine-tuned to ensure that the polynomial function $\mathbf{J}_{\text{polynomials}}(E_0)$ effectively reproduces the discrete points $E_k, \mathbf{J}_k$ in Figure 4.4.

Moving on to the second step, we aim to process the discrepancy between the discrete points in Figure 4.4 and the polynomial function $\mathbf{J}_{\text{polynomials}}(E_0)$. To achieve this, we define the residual error of the polynomial regression as:

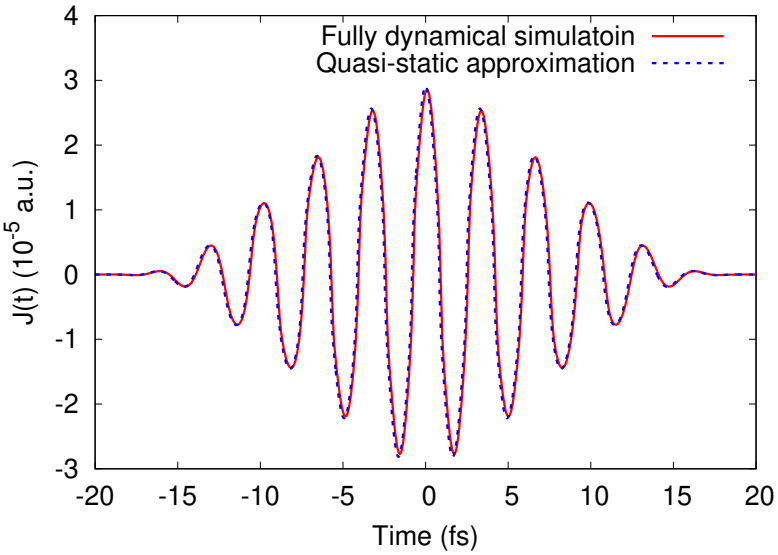

Figure 4.5: Comparison of the THz-induced current computed with the fully dynamical calculation and the quasi-static approximation. Figure is reproduced with permission from ref. ([113]). Copyright 2022, Phys. Rev. B.

$$\Delta \mathbf{J}_k = \mathbf{J}_k - \mathbf{J}_{\text{polynomials}}(E_k). \tag{4.6}$$

Subsequently, we apply spline interpolation to the data points $E_k, \Delta \mathbf{J}k$, denoting the interpolated function as $\Delta \mathbf{J}\text{spline}(E_0)$. Finally, we approximate the continuous function, $\mathbf{J}_S(E_0)$, as:

$$\mathbf{J}_S(E_0) \approx \mathbf{J}_{\text{polynomials}}(E_0) + \Delta \mathbf{J}_{\text{spline}}(E_0). \tag{4.7}$$

Utilizing the approximated function in Eq.(4.7), we evaluate the THz-induced electric current with the quasi-static approximation, Eq.(4.4). The relationship between current and field as expressed in Eq. (4.3), we approximate the field-induced current $\mathbf{J}(t)$ by the steady-state current, where the instantaneous electric field is denoted as $\mathbf{E}(t)$, leading to the approximation $\mathbf{J}(t) \approx \mathbf{J}_S(\mathbf{E}(t))$. Figure 5.2 showcases the computed current as a function of time with the quasi-static approximation. To promote comparison, the result of the fully dynamical calculation is also presented. Applying a Fourier transform to the obtained current in

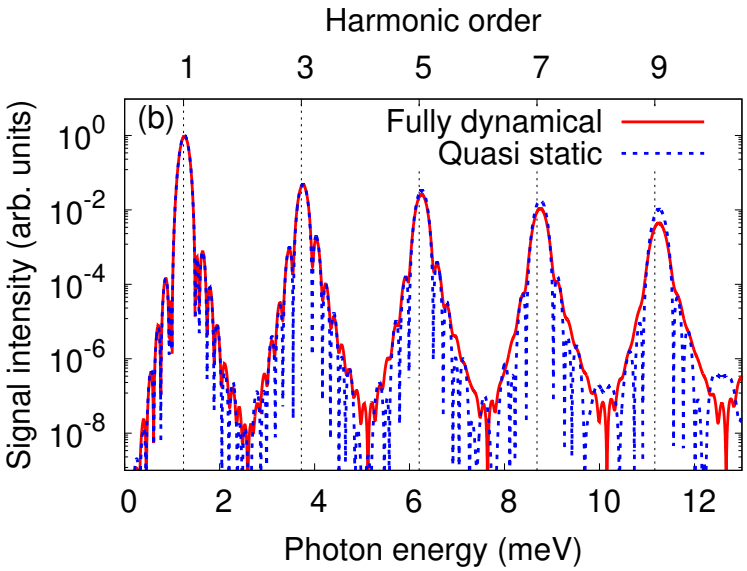

Figure 4.6: Comparison of the HHG spectra computed with the fully dynamical simulations in Sec. 4.1 and the quasi-static approximation in this section. Here, the chemical potential is set to $\mu = 170$ meV. Figure is reproduced with permission from ref. ([113]). Copyright 2022, Phys. Rev. B.

Figure 5.2 yields the HHG spectra illustrated in Figure 4.6.

4.3 Nonlinear Charge Transport in Nonequilibrium Steady-state

To provide a broader context, we compare the nonequilibrium steady-state achieved within the quasi-static framework with insights collected from a recently developed thermodynamic model [76]. This comparative analysis aims to clarify the nonequilibrium mechanisms controlling nonlinear optical and transport phenomena within graphene in the THz regime. By contrasting the quasi-static nonequilibrium picture with the thermodynamic model, we endeavor to unravel the underlying dynamics driving the complex interplay between electron behavior and external THz fields in graphene systems. We then study the nonlinear electric conductivity in a static regime in order to develop microscopic insight into the THz-induced HHG. For this purpose, we first define the intraband component of the steady-state current in Eq. (4.3).

Next, we proceed to evaluate the effective conductivities using both the to-

tal steady current $\mathbf{J}_S(E_0)$ computed from Eq. (2.38)and the intraband component $\mathbf{J}_S^{\text{intra}}(E_0)$ computed from Eq. (2.40). The effective total and intraband conductivities are computed as follows:

$$\sigma(E_0) = \frac{\mathbf{e}_x \cdot \mathbf{J}_S(E_0)}{E_0} \quad , \tag{4.8}$$

$$\sigma^{\text{intra}}(E_0) = \frac{\mathbf{e}_x \cdot \mathbf{J}_S^{\text{intra}}(E_0)}{E_0}. \tag{4.9}$$

Figure 4.7 illustrates the computed effective conductivities, $\sigma(E_0)$ and $\sigma^{\text{intra}}(E_0)$, as a function of the applied field strength E_0 for different chemical potentials μ. In this figure, the conductivities $\sigma(E_0)$ obtained from the total steady current $\mathbf{J}_S(E_0)$ align well with those derived from the intraband current $\mathbf{J}_S^{\text{intra}}(E_0)$ across all investigated field strengths E_0 and chemical potentials μ. This observation implies that the charge transport in graphene under static and THz fields is predominantly governed by the intraband current. The intraband current is described by the product of the band group velocity and the band population in the Brillouin zone.

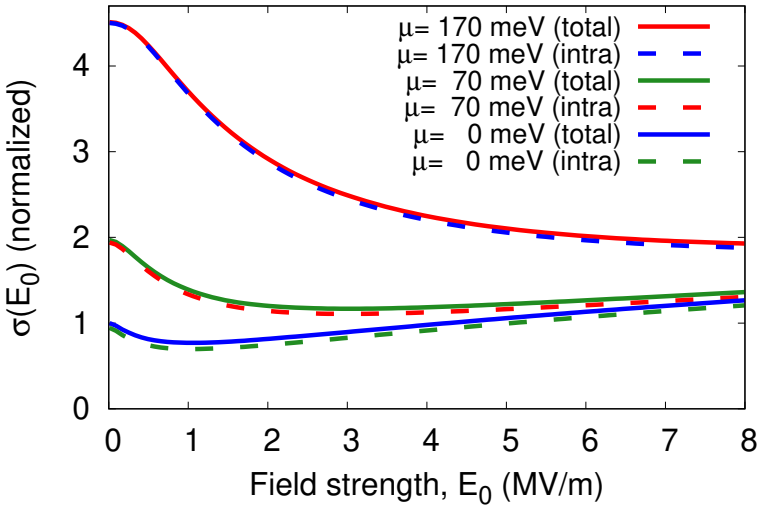

Figure 4.7: Nonlinear effective conductivities of graphene as a function of the static field strength E_0 evaluated with the total currents (solid lines) and intraband currents (dashed lines) for different values of the chemical potential, $\mu = 0$, 70 and 170 meV. Figure is reproduced with permission from ref. ([113]). Copyright 2022, Phys. Rev. B.

In Fig. 4.7, the effective conductivities, $\sigma(E_0)$, show an initial reduction across all investigated chemical potentials μ as the field strength increases from zero. This reduction in conductivity combines with the field-induced transparency phenomenon observed in graphene [90], as the conductivity $\sigma(E_0)$ is directly related to photo absorption via Joule heating, given by:

$$E_{\text{Joule}} = \mathbf{E}_0 \cdot \mathbf{J}_S(E_0) = \sigma(E_0)E_0^2 \tag{4.10}$$

As the field strength continues to increase, graphene with relatively small chemical potentials (e.g., $\mu = 0$ or 70 meV) shows an increase in conductivity, while graphene with a relatively large chemical potential (e.g., $\mu = 170$ meV) continues to show a reduction in conductivity. These trends are consistent with a previous theoretical study on nonlinear transport in graphene using the linear band approximation [90]:

$$H_{\mathbf{k}} = v_F \left(\sigma_x k_x + \sigma_y k_y\right) \tag{4.11}$$

Given that the present work employs a more comprehensive electronic structure throughout the full Brillouin zone based on the tight-binding model, it serves as a validation of the low-energy Hamiltonian approximation for the graphene bandstructure used in the previous work. In the previous study [90], the decrease in effective conductivity was attributed to the dispersion of the population imbalance in the Brillouin zone, while the increase in conductivity was linked to additional carrier injection through the Zener tunneling mechanism. These interpretations naturally apply to the results obtained in the present study, further confirming the robustness and applicability of the previously proposed mechanisms.

Given the ability of the quasi-static approximation in accurately describing THz-induced electron dynamics, the interpretation of THz-induced High-Order Harmonic Generation (HHG) finds its foundation in the effective conductivities, as illustrated in Fig. 4.7. The conductivity $\sigma(E_0)$ remain saturated by the field strength E_0, the induced current maintains linear proportionality to the field strength, thereby preventing the generation of harmonics. Consequently, within the quasi-static framework, the emergence of harmonics arises from the nonlinearity inherent in the current $\mathbf{J}_S(E_0)$ and the field-strength-dependent conductiv-

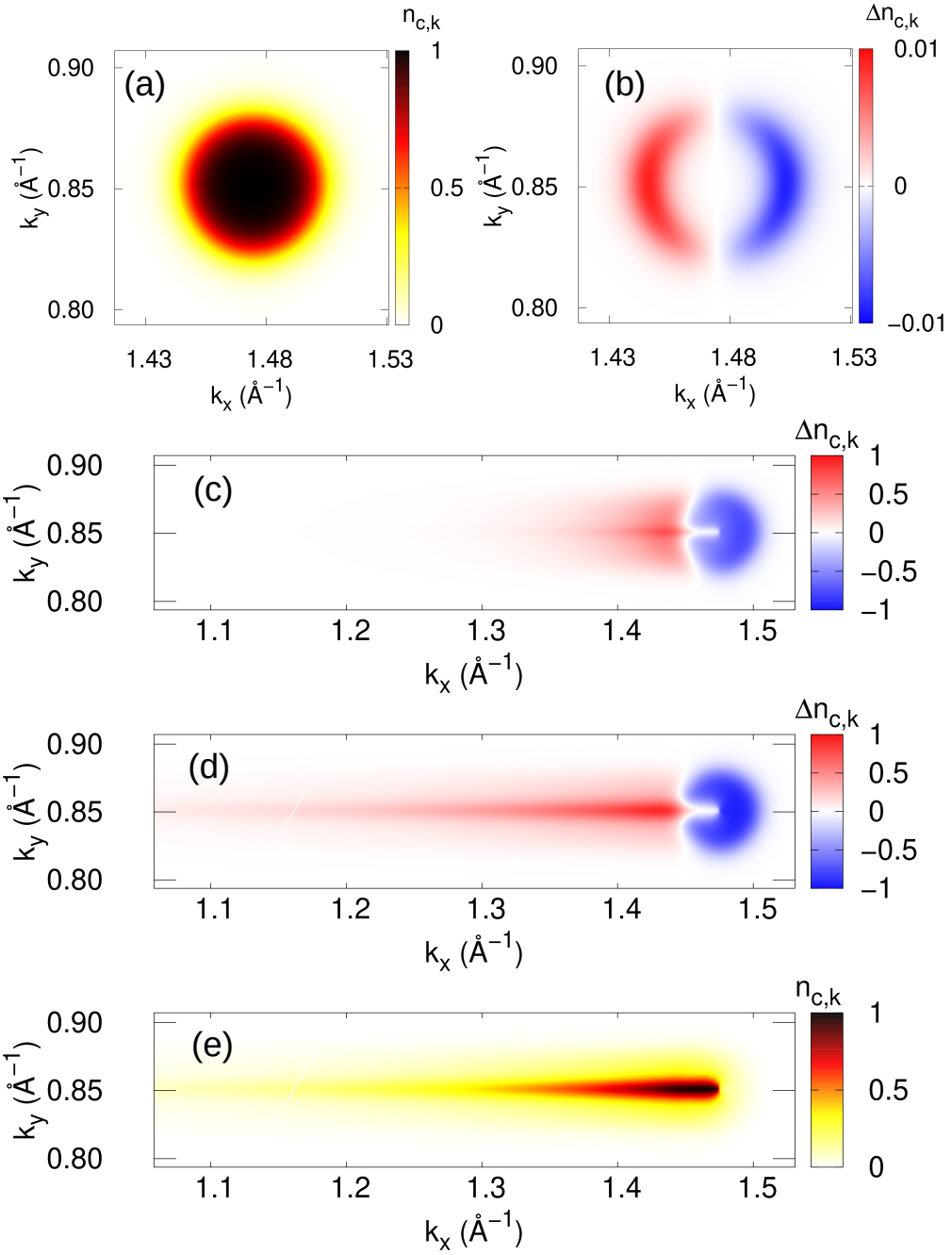

Figure 4.8: (a) The equlibrium population distribution in the conduction band $f^{\mathrm{FD}}(\epsilon_{c,\mathbf{k}})$. (b-d) The field induced conduction population change for different field strengths, (b) 0.01 MV/m, (c) 3 MV/m, and (d) 10 MV/m. (e) The population distribution in the conduction band in the nonequilibrium steady-state under a static field, $E_0 = 10$ MV/m. Panels are reproduced with permission from ref. ([113]). Copyright 2022, Phys. Rev. B.

ity $\sigma(E_0)$.

Examining Fig.4.7, it becomes evident that the conductivity shows strengthened sensitivity to the field strength, particularly emphasized for larger chemical potentials. This emphasized dependence manifests as a pronounced reduction in conductivity with increasing field strength. This observation supports the explanation of the strengthened HHG in Fig.4.2 accompanying a shift in chemical potential—attributed to the significant reduction in conductivity coincident with the amplified field strength.

In former investigations [108, 112], the interpretation of THz-induced HHG in graphene was fixed in the reduction of conductivity, although within the framework of the thermodynamic model [76]. To unravel the influence of nonequilibrium dynamics in the steady state, we shall investigate into the interrelation between the two models—the nonequilibrium steady-state model and the thermodynamic model—in the forthcoming section, Sec. 4.4.

Moving to the intraband current presented in Eq.(2.40), it is crucial to recognize its composition—encompassing the product of band velocity and population. Given the inherent invariance of band velocity under the presence of electric fields as an essential material property, the point of THz-induced current generation lies in the field-induced modulation of population. Furthermore, as explained earlier, the THz-induced current is predominantly governed by the intraband component. For an complex understanding of the THz-induced current at a microscopic level, we shall undertake an analysis of the population distribution within the Brillouin zone under the influence of the field. Figure4.8 (a) describes the equilibrium population distribution in the conduction band, denoted as $f^{\mathrm{FD}}(\epsilon_{c,\mathbf{k}})$, Eq. (2.37), around a Dirac point (K point) in graphene, specifically at $K = \frac{2\pi}{\sqrt{3}a}\left(1, \frac{1}{\sqrt{3}}\right)$. Here, the chemical potential μ is established at 170 meV. The equilibrium population shows a circular symmetry around the Dirac point, reflecting the partial filling of the Dirac cone by doped electrons.

We define the field-induced change in conduction population within a nonequilibrium steady state as:

$$\Delta n_{c,\mathbf{k}} = \left[n_{c,\mathbf{k}'+e\mathbf{A}(t)/\hbar}(t) - f^{FD}(\epsilon_{c,\mathbf{k}'+e\mathbf{A}(t)/\hbar})\right]_{\mathbf{k}'+e\mathbf{A}(t)/\hbar=\mathbf{k}} \tag{4.12}$$

Figures 4.8 (b-d) showcase the field-induced conduction population $\Delta nc, \mathbf{k}$ for varying field strengths: (b) 0.01MV/m, (c)3MV/m, and (d)10 MV/m.

As illustrated in Fig.4.8(b), the field-induced population modulation emerges along the ring-shaped contour defined by the single-particle energy $\epsilon_{b\mathbf{k}}$ and the Fermi energy $\epsilon_{\mathrm{F}} = \mu\big|_{T_e=0}$ as $\epsilon_{b\mathbf{k}} = \epsilon_{\mathrm{F}}$, specifically where $\epsilon_{b\mathbf{k}} = \epsilon_{\mathrm{F}}$. The modulation occurs near to the Fermi energy due to the mild field excitation, and the ring structure derives from the circular symmetry inherent in the Dirac cone. In the weak field regime, the increasing and decreasing in conduction population $\Delta n_{c,\mathbf{k}}$ show symmetric distribution along the field direction (x-axis). On the contrary, in the strong-field regime, the distribution becomes non-symmetric, as evident in Figs.4.8(c) and (d). Here, the red-colored region signifies an expanded range on the left side of the Dirac point, where population increase occurs, while the blue-colored region indicates a more confined area on the right side marked by population decrease. The population increase along the field direction may be construed as a consequence of the field-induced intraband acceleration within the Brillouin zone. Simultaneously, the localized population decrease around the Dirac point, as observed in Fig.4.8(a), can be attributed to the field-induced displacement of initially localized electrons enveloping the Dirac point.

In the previous study [90], the decrease in conductivity was a manifestation of the saturation of population imbalance surrounding the Dirac point. To examine this interpretation, we present the conduction population distribution:

$$n_{c,\mathbf{k}'+e\mathbf{A}(t)/\hbar}\big|_{\mathbf{k}'+e\mathbf{A}(t)/\hbar=\mathbf{k}} \tag{4.13}$$

in instead of the population change $\Delta n_{c,\mathbf{k}}$ in Fig.4.8(e), with the field strength E_0 set to 10MV/m. It is noteworthy that the summation of the density in Fig.4.8(a) and the density change in Fig.4.8(d) corresponds to the density in Fig.4.8 (e).

Examining Fig.4.8(e), a obviuos shift in the conduction population from the right to the left side of the Dirac cone is evident. This observation indicates that the population imbalance enveloping the Dirac cone is already near its maximum saturation point, where no further population can be transferred from the right side to the left side. Consequently, the population imbalance, a central determinant of the intraband current, reaches saturation in the strong-field regime,

preventing any substantial increase. This saturation, in turn, leads to the saturation of the intraband current—predominant in the nonequilibrium steady state—finally ultimating in the observed reduction in conductivity within the strong-field regime.

Our investigation reveals a substantial decrease in the effective conductivity of graphene in the strong-field regime, attributed to the saturation of population imbalance within the Brillouin zone. This reduction combines with the observed THz-induced transparency in graphene, as reported experimentally [109–111] and theoretically investigated in former studies [90]. Furthermore, we establish that this diminished conductivity leads to nonlinear current behavior in the strong-field regime, ultimating in high-order harmonic generation in graphene. Thus, the origin of high-order harmonic generation can be understood through the lens of saturation of population displacement within the Brillouin zone in the context of nonequilibrium electron dynamics.

4.4 Comparison with Thermodynamic Model

Having clarified the microscopic intricacies of THz-induced HHG in graphene within the framework of the none equilibrium steady-state, our focus now shifts to investigating the specific role played by the nonequilibrium nature of THz-induced electron dynamics. To accomplish this, we undertake a comparative analysis with the previously formulated thermodynamic model [76]. In contrast to the present nonequilibrium model, the thermodynamic model relies on the utilization of the thermal Fermi–Dirac distribution to delineate laser-excited electronic systems. This model operates under the assumption that electrons swiftly undergo thermalization, allowing them to be effectively treated as an equilibrium state characterized by a notably high electron temperature T_e.

Within the thermodynamic model, equilibrium states find characterization through the electron temperature T_e, while in the developed nonequilibrium model, nonequilibrium steady-states are essentialally defined by the applied field strength E_0, devoid of any reliance on temperature considerations. To ensure a equitable

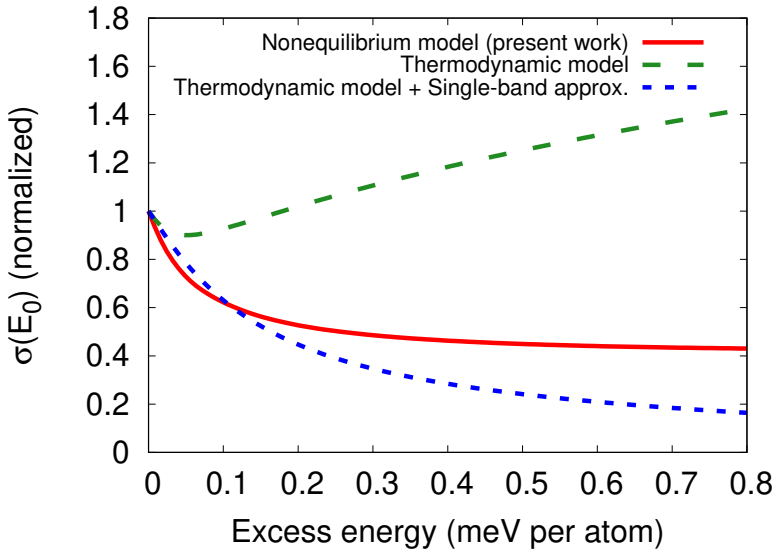

Figure 4.9: Computed effective conductivities are shown as a function of the excess energy. The results for the nonequilibrium steady-state (red-solid), the thermodynamic model (green-dashed), and the thermodynamic model plus the single-band approximation (blue-dotted) are shown. Figure is reproduced with permission from ref. ([113]). Copyright 2022, Phys. Rev. B.

comparison between the two models, it becomes imperative to establish a connection between the electron temperature T_e and the field strength E_0. This connection is promoted by the introduction of the field-induced excess energy for each model.

The total energy of the electronic system is formulated as:

$$E_{\text{tot}}(t) = \frac{2}{(2\pi)^2} \int d\mathbf{k} \text{Tr} \left[H_{\mathbf{k}+e\mathbf{A}(t)/\hbar} \rho_{\mathbf{k}}(t) \right]. \tag{4.14}$$

Subsequently, the field-induced excess energy of the nonequilibrium steady-state is defined as

$$\Delta E^{\text{NEQ}}_{\text{excess}}(E_0) = \lim_{t\to\infty} \left[E_{\text{tot}}(t) - E_{\text{tot}}(-t) \right], \tag{4.15}$$

Here, $\lim_{t\to\infty} E_{\text{tot}}(t)$ corresponds to the total energy in the nonequilibrium steady-state under the presence of the field E_0, while $\lim_{t\to\infty} E_{\text{tot}}(-t)$ corresponds to that of the equilibrium state without the field. Thus, the field-induced excess energy of the nonequilibrium model captures the energy difference between the

nonequilibrium steady-state under an external field E_0 and the field-free equilibrium state.

In contrast, the field-induced excess energy of the thermodynamic model is defined as the energy difference between finite temperature states at T_e and 300K, the initial temperature of the present nonequilibrium model:

$$\Delta E^{\text{TM}}_{\text{excess}} = \sum_{b=v,c} \frac{2}{(2\pi)^2} \int d\mathbf{k} \epsilon_{b\mathbf{k}} \times \left[f^{\text{FD}}\left(\epsilon_{b\mathbf{k}}, T_e, \mu\right) - f^{\text{FD}}\left(\epsilon_{b\mathbf{k}}, T_e = 300\ \text{K}, \mu\right) \right]. \tag{4.16}$$

Therefore, $\Delta E^{\text{TM}}_{\text{excess}}$ is expressed as a function of the electron temperature T_e.

By employing Eq.(4.15) and Eq.(4.16), we establish a link between the applied field strength E_0 characterizing the nonequilibrium steady-state and the electron temperature T_e inherent to the thermodynamic model through the concept of excess energy. This connection enables a comparative analysis of the effective conductivity $\sigma(E_0)$ in the nonequilibrium steady-state and the linear conductivity of the thermodynamic model.

Figure 4.9 presents the conductivities of the nonequilibrium steady-state (illustrated by the red-solid line) and the thermodynamic model (represented by the green-dashed line). The computations for the nonequilibrium steady-state consider a chemical potential μ set to 170 meV and an electron temperature T_e in the relaxation operator set to 300 K. In contrast, the linear conductivity of the thermodynamic model is evaluated under the influence of a weak field, ensuring the induced current combines with a linear response. The results for the thermodynamic model involve varying the electron temperature T_e while maintaining the total population constant, as expressed by:

$$N_{\text{tot}} = \frac{2}{(2\pi)^2} \sum_{b=v,c} \int d\mathbf{k} f^{FD}(\epsilon_{b\mathbf{k}}, T_e, \mu), \tag{4.17}$$

to the value at $T_e = 300$ K and $\mu = 170$ meV. Consequently, the chemical potential goes through adjustments with changes in the electron temperature.

Figure 4.9 illustrates that the conductivity of the thermodynamic model (represented by the green-dashed line) initially experiences a decrease with an in-

crease in the excess energy, followed by a notable upturn once the excess energy reaches a fairly large value. In contrast, the conductivity of the nonequilibrium steady-state (represented by the red-solid line) consistently decreases with the increase of the excess energy across the entire explored range. It's important to note that the conductivity of the nonequilibrium steady-state in Fig.4.9 combines with that in Fig.4.7 when considering the converted x-axis. The fundamental contrast between the conductivities of the nonequilibrium steady-state and the thermodynamic model arises from the interband excitation influenced by temperature. In the thermodynamic model, thermal excitation drives electrons from the valence band to the conduction band, enhancing effective carrier population and subsequently enhancing conductivity with elevated electron temperatures. In contrast, the nonequilibrium steady-state experiences a significant suppression of field-induced interband excitation due to Pauli blocking, moderating the artificial rise in effective carrier population and the resultant increase in conductivity.

In previous study by Mics in ref. [76], the authors investigated into the microscopic intricacies of THz-induced high-order harmonic generation and field-induced transparency in graphene using the thermodynamic model. Notably, the investigation adopted a single-band approximation in which only the conduction band was considered, while the valence band remained frozen. Surprisingly, this single-band approximation showed better agreement with experimental results than the two-band approximation, where both valence and conduction bands were considered [108]. Despite the instinctive expectation that the two-band approximation would offer greater accuracy, the results indicated that the single-band approximation provided a more accurate picture within the thermodynamic model.

To clarify the role of the single-band approximation in the thermodynamic model, we extended our comparison between the thermodynamic model and the nonequilibrium steady-state by considering the single-band approximation into our analysis. In this adaptation, we phenomenologically constrained the population in the valence band, while maintaining the use of the Fermi–Dirac distribution for the conduction band. This modification involved transforming the

Fermi–Dirac distribution as follows:

$$\tilde{f}^{\mathrm{MFD}}(\epsilon, T_e, \mu) = f^{\mathrm{FD}}(\epsilon, T_e, \mu)\Theta(\epsilon) + \Theta(-\epsilon), \tag{4.18}$$

where $\Theta(\epsilon)$ represents the Heaviside step function. By replacing the original Fermi–Dirac distribution (Eq.(2.37)) with the modified version (Eq.(4.18)), we conducted a comparative analysis of conductivity with the thermodynamic model. The results of the thermodynamic model considering the single-band approximation are illustrated by the blue-dotted line in Fig. 4.9. Remarkably, this modified thermodynamic model effectively reproduces the conductivity trend observed in the nonequilibrium steady-state, showcasing a consistent monotonic decrease with an increase in excess energy.

This interesting outcome suggests that the freezing of the valence band in the single-band approximation decreases the artificial interband excitation in the thermodynamic model, leading to a more accurate performance of conductivity. In contrast, the nonequilibrium steady-state, based on a fully dynamical model, naturally captures the suppression of interband excitation, providing an accurate representation of electron dynamics in graphene under THz fields without resorting to the freezing of the valence band.

Consequently, our findings indicate that the thermodynamic model shows an enhancement of the electric conductivity when subjected to intense THz fields, originating from interband transitions between the valence and conduction bands. To compare with former thermodynamic model[108], we introduced a single-band approximation, freezing the valence band to forbid interband excitation. Correspondingly, the computed conductivity in the thermodynamic framework, employing this single-band approximation, accurately reflects the anticipated decreasing trend under static field radiation. This trend combines with experimental observations of the field-induced transparency of graphene [109–111]. In contrast, the nonequilibrium model developed in this study effectively captures the decreasing trend in conductivity under static field irradiation without the need for artificially freezing the valence band. This emphasized the essential role of the nonequilibrium nature of electron dynamics in describing conductivity reduction under electric field irradiation and preventing interband excitation, as

evidenced in the comparison with the thermodynamic model.

Chapter 5

ENHANCEMENT OF MIR-INDUCED HHG BY COHERENT COUPLING WITH THZ FIELD

The discussion and results presented in this chapter ar an adaptation of the article by Ref. ([114]) [Wenwen Mao *et al.*, Enhancement of high-order harmonic generation in graphene by mid-infrared and terahertz fields. (2024) *Phys. Rev. B* 109 (4), 045421]

Following a detailed exploration of the phenomenon of dc-current injection and the generation of population imbalance through the application of two-color linearly polarized laser fields in Chapter 2, it is also interesting to explore the enhance or suppress the efficiency of solid-state HHG by 2-field coupling for the development of innovative HHG-based light sources and spectroscopies. Recent investigations have indicated the potential enhancement of HHG from graphene using two-color laser fields explained various mechanisms [21, 115, 116], involving the interaction of electron-hole pair creation induced by high-frequency pump light and the subsequent acceleration of these created pairs by low-frequency light. Mrudul *et al.* looked into HHG from graphene under bicircular fields, showcasing the ability to control valley polarization[21]. Additionally, Avetissian *et al.* explored HHG from graphene under linearly polarized light and its second

harmonics. They demonstrated that, when the two-color fields are perpendicularly polarized, stronger harmonics can be induced compared to parallel polarization [116]. Recently, HHG from graphene has garnered experimental attention in the mid-infrared (MIR)[117, 118] and terahertz (THz)[119, 120] regimes, revealing distinctive ellipticity dependence and remarkable efficiency. Similar to our previous work on HHG from graphene in the THz regimes in Chapter 4, based on a quantum master equation, this theoretical methodology has been adeptly applied in the MIR region [121] for the clarification of experimental results [117, 118].

Furthermore, in the MIR regime, the coupling between field-induced intraband and interband transitions unfolds crucial channels for HHG, leading to enhanced HHG with finite ellipticity [121]. Real-time electron dynamics simulations in the THz regime have highlightd the significance of considering the nonequilibrium steady-state, resulting from the delicate balance between field-driving and relaxation. This approach exceeds the limits of the equilibrium thermodynamic framework and provides a more comprehensive understanding of HHG from graphene [113].

Based on all the experimental development by THz and MIR field induced HHG in grahene, the potential application on enhancement or suppression by the coupling of two fields haven't been studied yet. In this chapter, we look into the prospect of adding a THz field to adjust MIR-induced HHG in graphene, drawing insights from our collective results from previous chapters. We first build a strong non-equilibrium steady field by a intensed THz field under quasi-static approximation, then we look into the HHG induced by MIR field in this imbalanced stated with inversion symmetry breaking by the THz field grahene. With same implementation in Chapter. (4), we employ a quantum master equation to investigate electron dynamics under both MIR and THz fields, subsequently assessing the induced harmonicpectra. The outcomes from fully dynamical calculations are compared with thermodynamic model that incorporates the equilibrium Fermi–Dirac distribution. Additionally, a nonequilibrium population model is considered, justifying a population distribution in a nonequilibrium steady-state. Through our analysis, we reveal the central role played by coupling induced coherence via THz and MIR fields in enhancing MIR-induced HHG. This

clarification highlights the significance of field-induced coherence, extending beyond mere population effects.

5.1 MIR-induced HHG in Graphene under THz Fields

We use the same theoretical model as Chapter. (4) by solving quantum master equation as equation of motion shown in Eq. (2.32). In our analysis of HHG induced by a MIR laser pulse in the presence of THz fields, we adopt a practical form for the MIR pulse, expressed as follows:

$$\mathbf{A}_{MIR}(t) = -\frac{E_{MIR}}{\omega_{MIR}}\mathbf{e}_{MIR}\sin(\omega_{MIR}t)\cos^4\left(\frac{\pi}{T_{MIR}}t\right) \tag{5.1}$$

This pulse is defined in the domain $-T_{MIR}/2 < t < T_{MIR}/2$ and is zero outside this range. Here, E_{MIR} represents the peak strength of the MIR field, ω_{MIR} is the mean frequency, $\mathbf{e}_{MIR}$ is a unit vector indicating the polarization direction of light, and T_{MIR} is the pulse duration. Specifically, we set the pulse duration T_{MIR} to 0.4 ps and the mean frequency ω_{MIR} to 0.35424 eV/$\hbar$ for this study, while other parameters are varied in our computation.

First, we investigate HHG in graphene only with the MIR fields. For practical analysis, the direction of the angle 0° is fixed to the Γ–M axis (the $x-$axis in our setup), and the peak field strength of the MIR field E_{MIR} is fixed at 6.5 MV/cm. The induced harmonics are investigated by manipulating the polarization direction of the MIR field, $\mathbf{e}_{MIR}$.

To analyze the HHG efficiency, we compute the signal intensity of the induced harmonics from Eq (4.2)at each order by integrating the power spectrum within a finite energy range as the integrated intensity of the induced nth harmonic $I^{n\text{th}}_{\text{total}}$:

$$I^{n\text{th}}_{\text{total}} = \int_{(n-\frac{1}{2})\omega_{MIR}}^{(n+\frac{1}{2})\omega_{MIR}} d\omega I_{\text{HHG}}(\omega). \tag{5.2}$$

Figures 5.1 illustrate the computed angular dependence of the induced harmonic $I^{n\text{th}}_{\text{total}}$ using only the MIR field. The induced harmonics show a six-fold symmetry, reflecting the hexagonal lattice symmetry of graphene. As showned

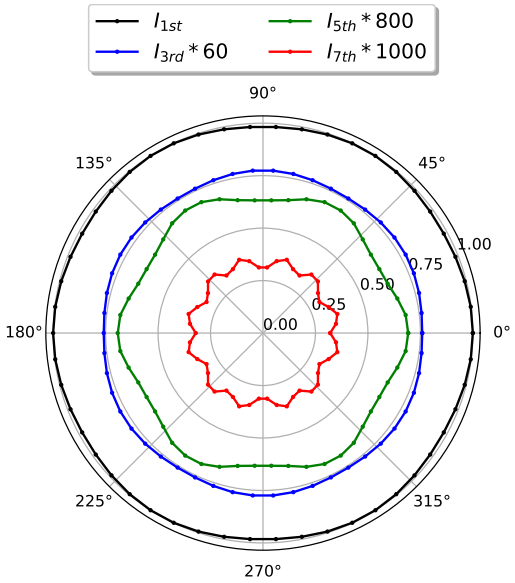

Figure 5.1: The angular dependence of the harmonic obtained from the electron dynamics calculations in the presence of the MIR field. The third, fifth, and seventh harmonic are scaled by factors of 60, 800, and 1000, respectively. Figure is reproduced with permission from ref. ([122]). Copyright 2024, Phys. Rev. B.

in Fig. 5.1, the lower-order harmonics display an almost circular angular dependence, pointing to the circular symmetry in Dirac cones. In contrast, the higher-order harmonics demonstrate a more complicated six-fold symmetry in their angular dependence, owing to the variation of the electronic structure of graphene from a simple Dirac cone when a single-particle energy is distant from the Dirac point. Similarly, we adopt the subsequent expression for the THz pulse:

$$\mathbf{A}_{THz}(t) = -\frac{E_{THz}}{\omega_{THz}}\mathbf{e}THz\sin(\omega THzt)\cos^4\left(\frac{\pi}{T_{THz}}t\right) \tag{5.3}$$

within the period $-T_{THz}/2 < t < T_{THz}/2$, and zero outside this range. Here, E_{THz} denotes the peak strength of the THz field, ω_{THz} is the mean frequency, $\mathbf{e}_{THz}$ represents a unit vector along the polarization direction, and T_{THz} stands for the pulse duration. In our investigation, the pulse duration T_{THz} is fixed at 40 ps, and the mean frequency ω_{THz} is set to 1.2407 meV/$\hbar$. The time profile of the applied THz electric field is showned in Fig.5.2(a).

To illustrate the complexity of THz-assisted MIR-induced HHG in graphene, we conduct an electron dynamics calculation in the presence of both THz and MIR fields, denoted as $\mathbf{E}_{THz}(t) + \mathbf{E}_{MIR}(t)$. Here, we set E_{MIR} to 6.5 MV/cm and E_{THz}

to 0.5 MV/cm. It is appropriate to note that experimentally available intense THz pulses can show amplitudes exceeding 1 MV/cm [123]. The polarization direction of the THz field $\mathbf{e}_{THz}$ is Γ–M direction (the x-direction in our setup), while the polarization direction of the MIR field $\mathbf{e}_{MIR}$ is considered as a tunable parameter. Figures 5.2(a) and (b) illustrate the computed current $\mathbf{J}(t)$ induced by $\mathbf{E}_{THz}(t) + \mathbf{E}_{MIR}(t)$ as a function of time. The result for the parallel configuration ($\mathbf{e}_{MIR} = \mathbf{e}_x = \mathbf{e}_{THz}$) is presented in Fig.5.2(a), while the result for the perpendicular configuration ($\mathbf{e}_{MIR} = \mathbf{e}_y \perp \mathbf{e}_{THz}$) is shown in Fig.5.2(b). The x and y components are represented by blue and red lines, respectively. Evidently, Figs.5.2 (a) and (b) illustrate that the THz field induces a current on the picosecond time scale, whereas the MIR field induces a current on a much shorter time scale.

To look into MIR-induced HHG with the presence of THz fields, we investigate the current induced by the MIR field under the influence of the THz field. For this analysis, we compute two types of currents. Firstly, we denote the current induced by both the THz and MIR fields as $\mathbf{J}^{THz+MIR}(t)$. Secondly, we denote the current induced solely by the THz field as $\mathbf{J}^{THz}(t)$. Defining the current induced by the MIR field in the presence of the THz field as $\mathbf{J}^{eff}(t) = \mathbf{J}^{THz+MIR}(t) - \mathbf{J}^{THz}(t)$, we subject it to Fourier transformation, followed by computation of the power spectrum of the induced harmonics using Eq.(4.2). The solid line in Fig.5.2(e) shows the power spectrum computed using the current $\mathbf{J}(t)$ showned in Fig.5.2(a), where the polarization directions of the THz and MIR fields are parallel. On the other hand, the solid line in Fig.5.2(f) shows the power spectrum computed employing the current $\mathbf{J}(t)$ illustrated in Fig.5.2(b), where the polarization directions of the two fields are perpendicular. Notably, Fig.5.2(e) illustrates the generation of second and higher even-order harmonics next to odd-order harmonics, attributed to the local breakdown of the system's inversion symmetry induced by the THz field. This phenomenon, known as electric-field-induced second-harmonic generation (EFISH) or THz-induced second-harmonic generation (TFISH), has been extensively studied both exp and theoretically [124–127]. Similarly, even-order harmonics are generated in the perpendicular configuration ($\mathbf{e}_{MIR} \perp \mathbf{e}_{THz}$), as showned in Fig.5.2(f).

Including the THz pulse in the electron dynamics computation extends the propagation time (42 ps in the current situation), as illustrated in Figs.5.2(a) and

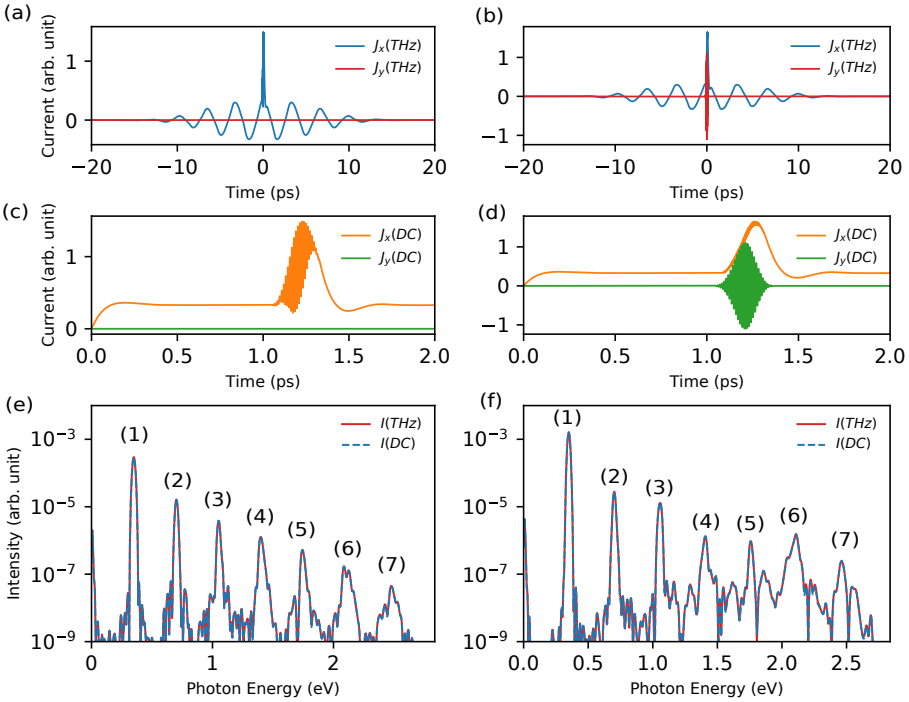

Figure 5.2: (a, b) The current $\mathbf{J}(t)$ induced by THz and MIR fields, $\mathbf{E}_{THz}(t) + \mathbf{E}_{MIR}(t)$. The x-component of the current is shown as the blue line, whereas the y-component is shown as the red line. Panel (a) shows the time profile of the applied THz field. (c, d) The current $\mathbf{J}(t)$ induced by the static and MIR fields, $\mathbf{E}_{dc}(t) + \mathbf{E}_{MIR}(t - \tau_{MIR})$. The x component of the current is shown as the orange line, whereas the y-component is shown as the green line. In the panels (a) and (c), the polarization of all the fields is parallel to the Γ–M direction (the x-direction in the present setup) as $\mathbf{e}_{THz} = \mathbf{e}_{dc} = \mathbf{e}_{MIR} = \mathbf{e}_x$. In the panels (b) and (d), the polarization of THz and static fields is parallel to the x-direction as $\mathbf{e}_{THz} = \mathbf{e}_{dc} = \mathbf{e}_{MIR} = \mathbf{e}_x$, while that of the MIR field is perpendicular as $\mathbf{e}_{MIR} = \mathbf{e}_y$. (e) The power spectra $I_{\text{HHG}}(\omega)$ computed using the current in (a) and (c). (f) The power spectra $I_{\text{HHG}}(\omega)$ computed using the current in (b) and (d). Panels are reproduced with permission from ref. ([122]). Copyright 2024, Phys. Rev. B.

(b). Consequently, performing electron dynamics calculations with the obvious inclusion of THz pulses involves a substantial computational trouble. To alleviate the computational overhead associated with modeling MIR-induced HHG in graphene under a THz field, we adopt a static field approximation based on the quasi-static approximation described in Chapter 4.

For practical analysis, we conduct two simulations. In the first simulation, electron dynamics are computed under a static field $\mathbf{E}_{dc}(t) = \mathbf{e}_{dc} E_{dc} \Theta(t)$, suddenly initiated at $t = 0$. Here, $\mathbf{e}_{dc}$ represents the unit vector along the polarization direction of the static field, and E_{dc} denotes the field strength. Upon the

sudden activation of the static field, the induced electron dynamics prompt a current. Following a sufficiently long time of propagation, the driven system attains a steady state, and the current stabilizes over time. We designate the current induced solely by $\mathbf{E}_{dc}(t)$ as $\mathbf{J}^{dc}(t)$.

In the second simulation, electron dynamics are computed under both the MIR and static fields, $\mathbf{E}_{dc}(t) + \mathbf{E}_{MIR}(t - \tau_{MIR})$, where the pulse center of the MIR field is shifted by τ_{MIR}. We denote the current induced by $\mathbf{E}_{dc}(t) + \mathbf{E}_{MIR}(t - \tau_{MIR})$ as $\mathbf{J}^{dc+MIR}(t)$. The shift τ_{MIR} can be made sufficiently large to investigate the MIR-induced electron dynamics for a full nonequilibrium steady state realized by the static field $\mathbf{E}_{dc}(t)$. Subsequently, the MIR-induced current can be extracted as $\mathbf{J}^{eff}(t) = \mathbf{J}^{dc+MIR}(t) - \mathbf{J}^{dc}(t)$ to analyze MIR-induced HHG in the presence of the static field.

Figures 5.2(c) and (d) illustrate the current $\mathbf{J}^{dc+MIR}(t)$ induced by both the static and MIR fields. The orange and green lines represent the x and y components of the current, respectively. Here, the static field along the Γ–M direction (the x-direction in our setup), and its strength E_{dc} matches the peak strength of the THz field, $E_{dc} = E_{THz} = 0.5$MV/cm. In Fig.5.2(c), the MIR field aligns parallel to the static field, while in Fig.5.2(d), it is perpendicular to the static field. To incorporate the MIR field into the nonequilibrium steady-state under the static field, we set the time delay τ_{MIR} of the MIR field to 1 ps, exceeding the relaxation time scales of the quantum master equation, T_1 and T_2.

To investigate HHG in the presence of the static field $\mathbf{E}_{dc}(t)$, we extract the current $\mathbf{J}^{eff}(t)$ induced by the MIR field in the presence of the static field by subtracting $\mathbf{J}^{dc}(t)$ from $\mathbf{J}^{dc+MIR}(t)$: $\mathbf{J}^{eff}(t) = \mathbf{J}^{dc+MIR}(t) - \mathbf{J}^{dc}(t)$. The dashed lines in Figs 5.2(e) and (f) represent the HHG spectra computed using the current shown in Figs5.2(c) and (d), respectively. Remarkably, the results obtained through the quasi-static approximation with a static field align perfectly with those computed by obviously including the THz pulse. This consistency highlights the validity of the quasi-static approximation for analyzing HHG under MIR and THz fields. Additionally, we verified the consistency of the quasi-static approximation across various static field strengths (refer to Figure 5.1). Hereafter, we employ the static field within the quasi-static approximation rather than obviously including the THz pulse.

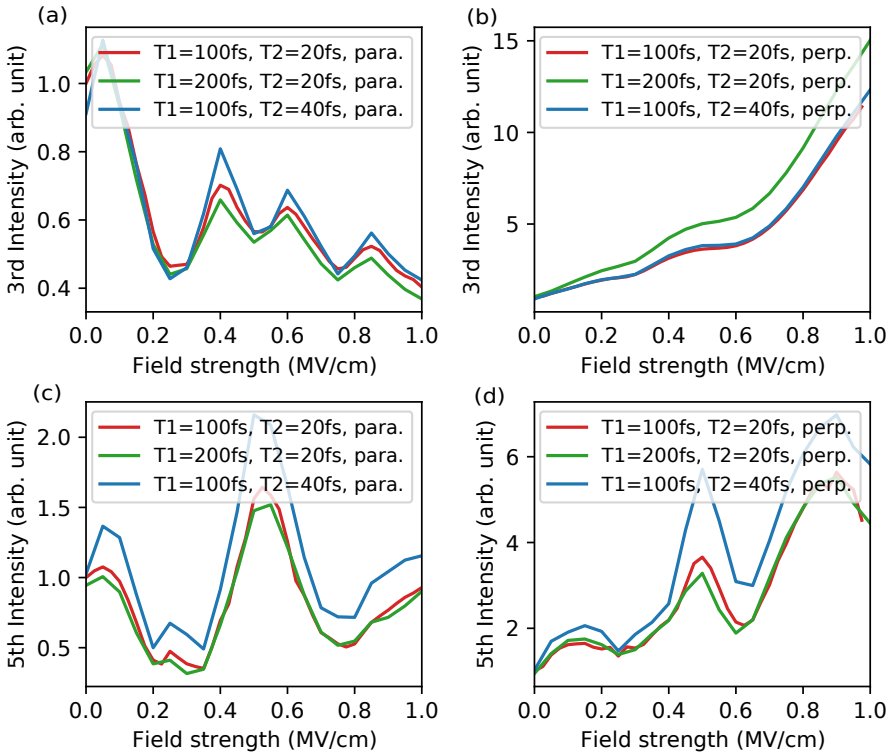

Figure 5.3: The harmonic are shown as a function of the static field strength E_{dc}. In each panel, the results obtained using the different relaxation times, T_1 and T_2, are compared. The results of the third harmonics are shown in the panels (a) and (b), whereas those of the fifth harmonics are shown in the panels (c) and (d). The results obtained using the parallel configuration ($\mathbf{e}_{MIR} = \mathbf{e}_x = \mathbf{e}_{THz}$) are shown in the panels (a) and (c), whereas those obtained using the perpendicular configuration ($\mathbf{e}_{MIR} = \mathbf{e}_y \perp \mathbf{e}_{THz}$) are shown in the panels (b) and (d). Panels are reproduced with permission from ref. ([122]). Copyright 2024, Phys. Rev. B.

We further investigate the influence of relaxation times, T_1 and T_2, on HHG in the presence of THz and MIR fields. Employing the methods outlined in Section. 2.3.2, we compute the intensity of third- and fifth-order harmonics under varying relaxation times. The results, showned in Fig.5.3, show consistent qualitative trends in HHG enhancement with THz field irradiation across different relaxation times. Thus, the specific choice of relaxation times does not substantially change the enhancement phenomenon.

Relaxation times are determined by diverse scattering mechanisms, including electron-electron, electron-phonon, and electron-impurity interactions. Consequently, the actual relaxation times in practical settings depend on experimental conditions. Nonetheless, the findings presented in Fig. 5.3 suggest that HHG en-

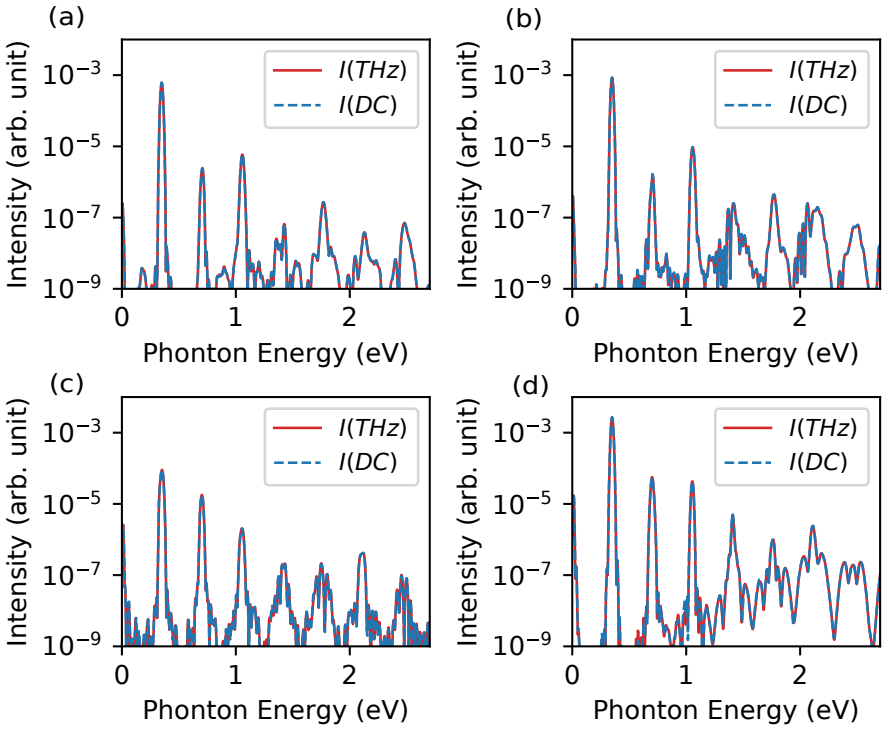

Figure 5.4: The power spectra of induced harmonics, $I_{HHG}(\omega)$, are shown. The results obtained using a weak THz field ($E_{THz} = 0.1$ MV/cm) are shown in the panels (a) and (b), while those obtained using a strong THz field ($E_{THz} = 1.0$ MV/cm) are shown in the panels (c) and (d). The results obtained using the parallel configuration ($\mathbf{e}_{MIR} = \mathbf{e}_x = \mathbf{e}_{THz}$) are shown in the panels (a) and (c), whereas those obtained using the perpendicular configuration ($\mathbf{e}_{MIR} = \mathbf{e}_y \perp \mathbf{e}_{THz}$) are shown in the panels (b) and (d). Panels are reproduced with permission from ref. ([122]). Copyright 2024, Phys. Rev. B.

hancement via THz field irradiation can present as a robust phenomenon across a broad spectrum of experimental situations.

We extend our investigation to validate the quasi-static approximation across varying strengths of the THz field. We repeat the analyses presented in Figs.5.2(e) and (f) while changeing the THz field strength. Results obtained under a weak THz field ($E_{THz} = 0.1$MV/cm) are showned in Figs.5.4(a) and (b), while those under a strong THz field ($E_{THz} = 1.0$MV/cm) are shown in Figs.5.4(c) and (d). As observed from the figures, the outcomes of the quasi-static approximation closely reflect those obtained from calculations with THz laser pulses across all investigated field strengths and polarization directions. Hence, we affirm the efficacy of the quasi-static approximation in accurately describing electron dynamics in graphene under THz and MIR fields, encompassing both weak and strong field

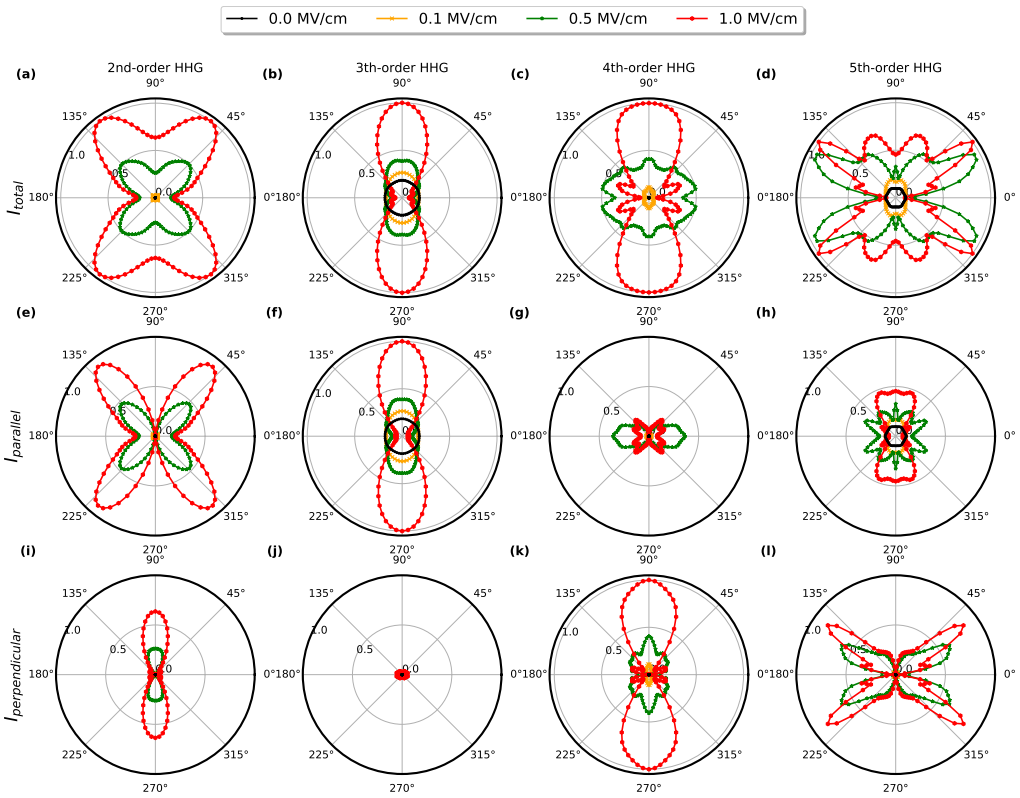

Figure 5.5: The angular dependence of the harmonic in the nonequilibrium steady-states under a static field along the Γ–M direction is shown for different static field strengths, E_{dc}. The angle θ denotes the relative angle between the static field and the MIR field. (a–d) The total intensity $I^{n\text{th}}_{\text{total}}$ is shown for the second, third, fourth, and fifth harmonics. (e-h) The component of the intensity parallel to $\mathbf{e}_{MIR}$ is shown for each harmonic. (i-l) The component of the intensity perpendicular to $\mathbf{e}_{MIR}$ is shown for each harmonic. The results are normalized by the maximum total intensity $I^{n\text{th}}_{\text{total}}$ for each harmonic. Panels are reproduced with permission from ref. ([122]). Copyright 2024, Phys. Rev. B.

regimes. This agreement between the quasi-static approximation and the obvious inclusion of the THz pulse highlights the central role played by the nonequilibrium steady state under the static field in MIR-induced HHG in graphene in the presence of a THz field.

5.2 Orientational Dependence of HHG

We explore high-harmonic generation (HHG) in graphene within the quasi-static approximation, varying the relative angle between the static and MIR fields. For our analysis, we maintain the direction of the static field $\mathbf{e}_{dc}$ along the Γ–M axis

(the x-axis in our setup) and set the peak field strength of the MIR field E_{MIR} to 6.5 MV/cm. We investigate the induced harmonics by manipulating the polarization direction of the MIR field, $\mathbf{e}_{MIR}$, and adjusting the strength of the static field, E_{dc}.

Figures 5.5(a–d) illustrate the angular dependence of the induced harmonic $I^{n\text{th}}$ for various harmonic orders. Here, θ represents the relative angle between the MIR and static fields. In Fig.5.5(a), absence of a static field results in no second harmonic generation, given the inversion symmetry of graphene. However, with the introduction of a static field, second harmonics emerge due to the breakdown of this symmetry. Notably, for a static field strength of 0.5MV/cm, the induced second-harmonic intensity peaks at approximately 45° relative angle.

In Fig.5.5(b), the third-harmonic appears nearly isotropic (showned by the black line) in the absence of a static field, reflecting the rotational symmetry of the Dirac cone (refer also to Figure 5.1). On the other hand, under the influence of a strong static field ($E_{dc} = 1.0$MV/cm), the third-harmonic intensity shows significant angular dependence: it is notably enhanced when the static and MIR fields are perpendicular to each other, whereas it is suppressed for parallel field orientations. This enhancement for the perpendicular configuration can be attributed to the coupling between the intraband transition induced by the static field and the interband transition induced by the MIR field, as previously suggested[121].

The angular dependence of higher-order harmonics becomes more complicated under a static field, as showned in Figs.5.5(c) and (d). Notably, the fifth-order harmonic emission shows significant enhancement in the presence of either static or THz fields (Fig.5.5(d)). For instance, applying a static field of 0.5MV/cm boosts the fifth-order harmonic intensity by more than tenfold compared to that induced solely by the MIR field (indicated by the green line in Fig.5.5(d)). This enhancement ratio surpasses that observed for the third-order harmonic, suggesting a greater potential for field-induced enhancement in higher-order harmonics. Indeed, the seventh-order harmonichows a 25-fold enhancement with a static field strength of 0.5MV/cm (refer to Figure 5.1).

To further illustrate the angular dependence of HHG in graphene, we decompose the harmonic intensity $I_{\text{HHG}}(\omega)$ into parallel and perpendicular components

with respect to the polarization of the driving MIR field. The parallel component of the HHG intensity is defined as

$$I_{\text{HHG}}^{\text{para}}(\omega) \sim \omega^2 \left| \int_{-\infty}^{\infty} dt \mathbf{e}_{MIR} \cdot \mathbf{J}(t) e^{i\omega t} \right|^2, \tag{5.4}$$

where $\mathbf{e}_{MIR}$ is the unit vector along the polarization direction of the MIR field. Likewise, the perpendicular component is defined as

$$I_{\text{HHG}}^{\text{perp}}(\omega) \sim \omega^2 \left| \int_{-\infty}^{\infty} dt \bar{\mathbf{e}}_{MIR} \cdot \mathbf{J}(t) e^{i\omega t} \right|^2, \tag{5.5}$$

where $\bar{\mathbf{e}}_{MIR}$ is a unit vector perpendicular to $\mathbf{e}_{MIR}$, i.e., $\bar{\mathbf{e}}_{MIR} \cdot \mathbf{e}_{MIR} = 0$. The total intensity I_{HHG} in Eq. (4.2) is reproduced by the sum of $I_{\text{HHG}}^{\text{para}}(\omega)$ and $I_{\text{HHG}}^{\text{perp}}(\omega)$ as $I_{\text{HHG}}(\omega) = I_{\text{HHG}}^{\text{para}}(\omega) + I_{\text{HHG}}^{\text{perp}}(\omega)$.

Equations (5.4) and (5.5) are used to separate the induced harmonic intensity into parallel and perpendicular components. Figures 5.5 (e–h) and (i–l) illustrate the angular dependence of the parallel and perpendicular components of the harmonic intensity, respectively, for different orders.

In Figs.5.5(a), (e), and (i), the parallel component of the second harmonic under the static field peaks around 45°, constituting the dominant contribution to the total second-harmonic intensity at this orientation. On the other hand, the maximum perpendicular component is consistently achieved when the MIR and static fields are orthogonal to each other. In Figs.5.5(b), (f), and (j), the third harmonic is predominantly governed by its parallel component across all angles and static field strengths examined. Notably, for both second- and third-harmonic generation, the parallel components prevail when the induced harmonic intensity is maximized.

Qualitative distinctions emerge between the lower-order harmonics (second and third) and the higher-order ones (fourth and fifth). In Fig.5.5(c), the fourth harmonic peaks at an angle θ of 90° under the strongest applied static field, $E_{dc} = 1.0$MV/cm. A comparison of Figs.5.5(g) and (k) reveals the predominance of the perpendicular component in the induced harmonic intensity under these conditions. On the other hand, as showned in Figs.5.5(d), (h), and (l), the induced fifth

harmonic at the most efficient angle is primarily governed by the perpendicular component, despite the dominance of the parallel component at all angles in the absence of a static field. Hence, the emission pathways associated with the perpendicular components are expected to play a crucial role in enhancing MIR-induced HHG by a THz field. This trend persists for higher-order harmonics as well (see Figure5.6): The angular dependency of the 6th(Figures5.6(a)) and 7th (Figures5.6(b)) HHG is analyzed similarly to the approach used in Fig.5.5. Further examination reveals in Figs.5.6(c) and (e) the decomposition of the sixth-harmonic signal into parallel and perpendicular components, while the same analysis is conducted for the seventh-order harmonic in Figs.5.6(d) and (f). In accordance with the findings for the fourth and fifth harmonics illustrated in Fig.5.5, it is evident from Fig. 5.6 that the perpendicular components play a significant role in the enhancement of mid-infrared (MIR)-induced high harmonic generation (HHG) by a terahertz (THz) field.

5.3 Comparison of Nonequilibrium Steady State and Thermodynamic Model

In this investigation, we look into the role of nonequilibrium steady states in high harmonic generation (HHG) by comparing the outcomes of the quasi-static approximation with those derived from the thermodynamic model [76], a framework previously used in studying HHG in graphene under THz fields [119, 120]. The quasi-static approximation replaces the THz pulse with a static field to describe the electronic system's behavior under THz irradiation, whereas the thermodynamic model approximates the system's response to a THz pulse as a high-temperature thermal state [76]. The difference between these models illustrates the influence of nonequilibrium distributions.

As explained in Chapter. (4), the quasi-static approximation is characterized by the static field strength, E_{dc}, while the thermodynamic model relies on the electron temperature T_e. To enable a direct comparison between these models, we introduce the concept of excess energy [113] as a common metric of excitation intensity. We use the same excess energy under the quasi-static approxima-

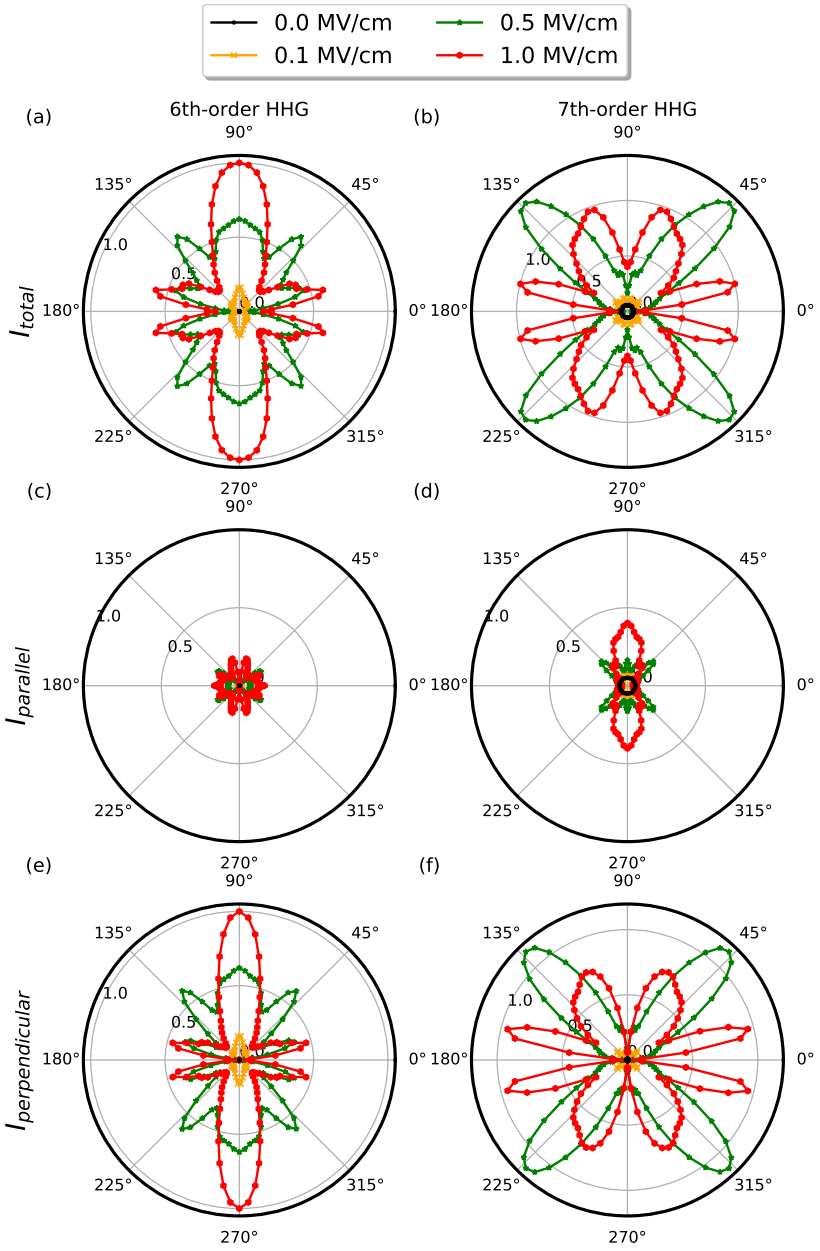

Figure 5.6: The angular dependence of the harmonic yields in the nonequilibrium steady state under a static field along the Γ–M direction is shown. The angle θ denotes the relative angle between the static field and the MIR field. (a and b) The total intensity $I^{n\text{th}}_{\text{total}}$ for the sixth and seventh harmonics is shown, respectively. (c and d) The component of the intensity parallel to e_{MIR} is shown for each harmonic. (e and h) Th component of the intensity perpendicular to e_{MIR} is shown for each harmonic. The results are normalized by the maximum total intensity $I^{n\text{th}}_{\text{total}}$ of each harmonic. Panels are reproduced with permission from ref. ([122]). Copyright 2024, Phys. Rev. B.

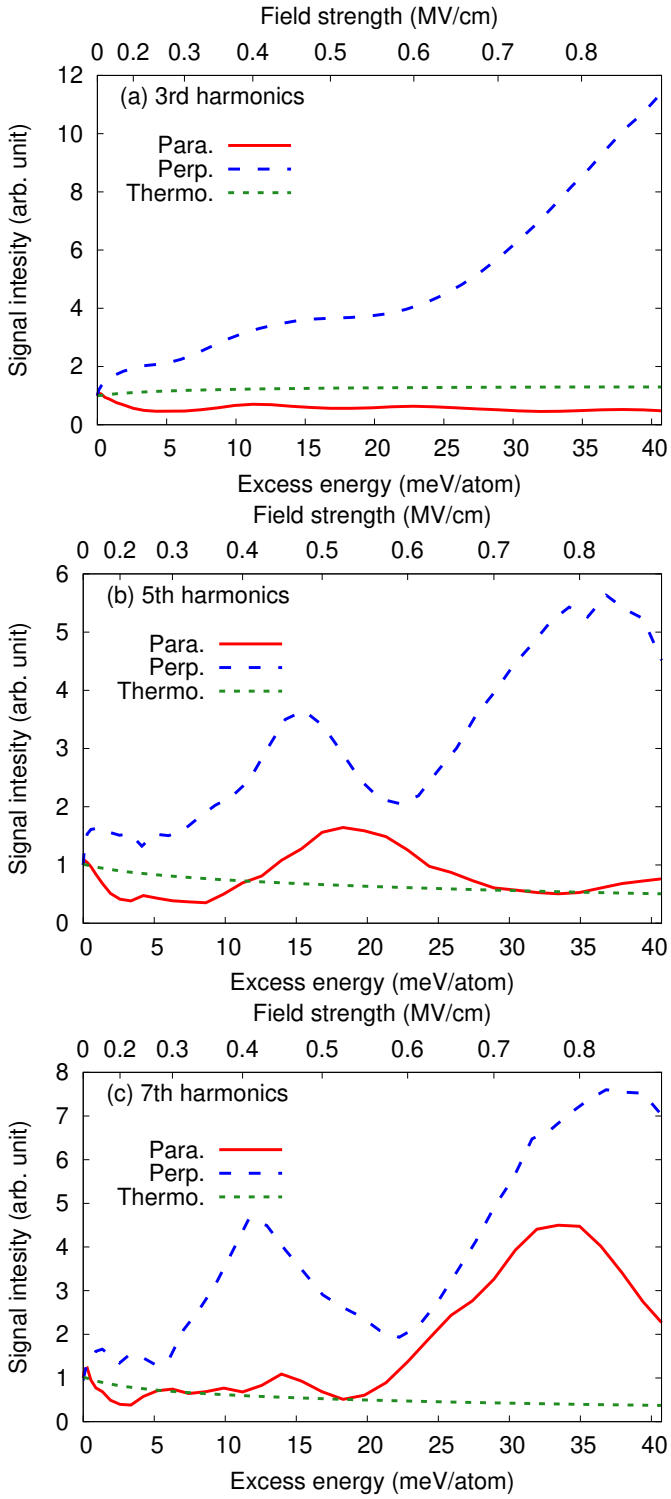

Figure 5.7: The induced light intensity, I^{nth}, is shown as a function of the excess energy for (a) third (b) fifth, and (c) seventh harmonics. The results for the nonequilibrium steady-states induced by a static field parallel (red solid line) and perpendicular (blue dashed line) to the MIR field are compared with the thermodynamic model (green dotted line). In each panel, the field strength of the static field parallel to the MIR field is shown as the secondary axis. Panels are reproduced with permission from ref. ([122]). Copyright 2024, Phys. Rev. B. Panels are reproduced with permission from ref. ([122]). Copyright 2024, Phys. Rev. B.

tion, denoted as $\Delta E^{\text{non-eq}}\text{excess}(Edc)$, quantifies the change in total energy due to the static field $\mathbf{E}_{dc}(t)$. On the other hand, the excess energy within the thermodynamic model, $\Delta E^{\text{thermo}}_{\text{excess}}(T_e)$, measures the energy change arising from an increase in electron temperature from room temperature ($T_e = 300$ K).

Figure 5.7 illustrates the comparison between the results obtained from the quasi-static approximation and the thermodynamic model. Setting the MIR field strength to 6.5 MV/cm and its polarization direction to the Γ–M direction (the x-axis), we observe distinct behaviors in odd-order harmonics between the two models. Figure 5.7(a) shows the substantial enhancement and suppression of the MIR-induced third harmonic under the quasi-static approximation for parallel and perpendicular configurations, respectively. In contrast, the thermodynamic model s nearly constant results. Figures5.7 (b) and (c) further reveal significant enhancements in the fifth- and seventh-harmonic under a static field within the quasi-static approximation, while the thermodynamic model shows small variations in harmonic with increasing electron temperature. Consequently, the observed HHG enhancement cannot be solely attributed to the simple heating of electronic systems within the thermodynamic model, underscoring the crucial role of non-equilibrium electronic dynamics induced by the field. The minimal changes in harmonic within the thermodynamic model relative to those predicted by the nonequilibrium steady-state model suggest that modifications in the population distribution around the Fermi level use insignificant influence on HHG spectra.

5.4 Contribution of Nonequilibrium Population

In our exploration of the coherent coupling between the MIR and THz fields, beyond the population contribution induced by the THz field, we introduce a nonequilibrium population distribution model as an extension of the thermodynamic model.

Within the thermodynamic model, the THz field's contribution is represented by adjusting the population distribution via an increased electronic temperature

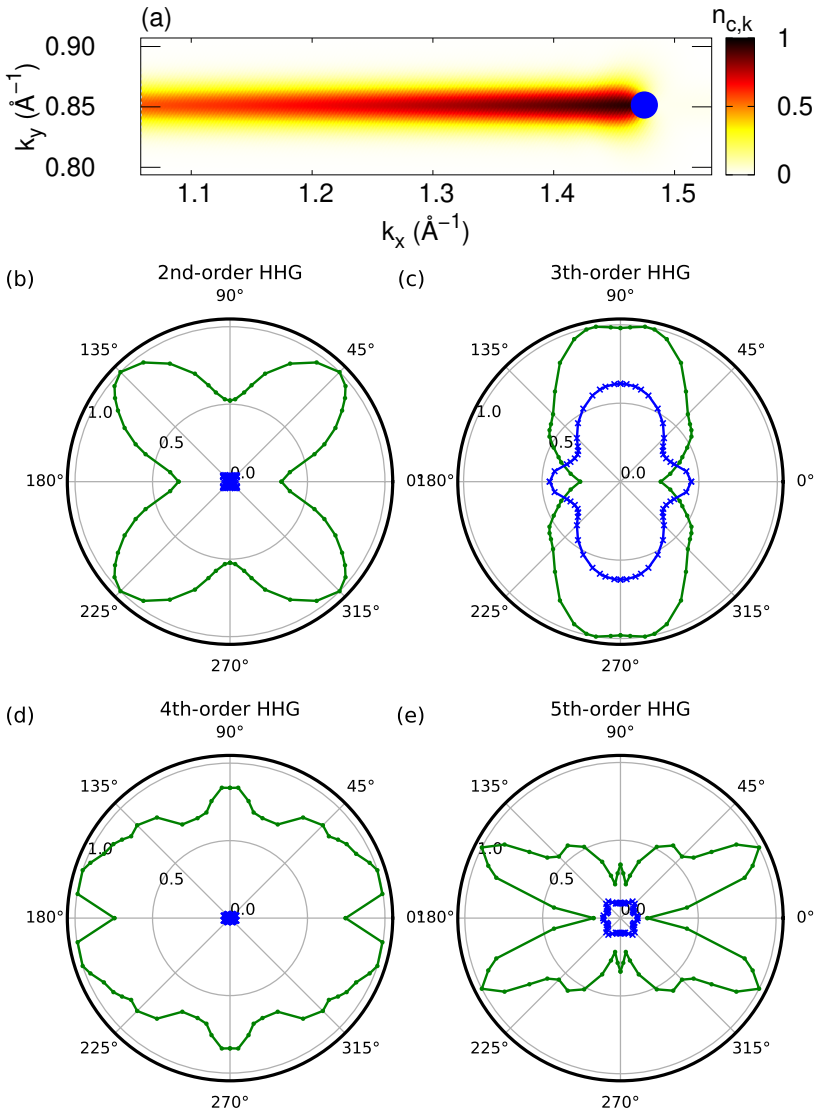

Figure 5.8: (a) The calculated conduction population distribution, $n_{c\mathbf{k}}^{\mathrm{neq-steady}}$ for the nonequilibrium steady-state is shown. Here, the Dirac point is indicated by the blue circle. (b–e) The angular dependence of the induced harmonic intensity is shown for the (b) second, (c) third, (d) fourth, and (e) fifth harmonics. The results obtained using the nonequilibrium population model and the nonequilibrium steady-state are shown by the blue and green solid lines, respectively. Panels are reproduced with permission from ref. ([122]). Copyright 2024, Phys. Rev. B.

in the reference Fermi–Dirac distribution. This model captures only the population contribution, corresponding to the diagonal elements of the density matrix, based on the thermal distribution.

To look into the coherent coupling contribution, we extend the thermodynamic model by substituting the reference Fermi–Dirac distribution in the relaxation operator (Eq. (2.36)) with the population distribution of the nonequilibrium steady state under a static field. This extension incorporates the population contribution, signified by diagonal elements of the density matrix, while omitting THz-induced coherence, represented by the off-diagonal elements of the density matrix.

By comparing the nonequilibrium population model with the fully dynamical model, which includes both population and coherence effects, we can distinguish the role of coherent coupling between the THz and MIR fields. This comparative analysis helps illustrate the distinct contributions of population and coherence effects to HHG, providing valuable insights into the underlying mechanisms governing this phenomenon. To formulate the nonequilibrium population model, we first analyze the population distribution in the nonequilibrium steady state under a static field. The population distribution in the Brillouin zone can be expressed as

$$\begin{aligned} n_{b\mathbf{k}}(t) &= \int d\mathbf{k}'\delta(\mathbf{k}-\mathbf{K}'(t))\mathrm{Tr}\left[|u^H_{b\mathbf{k}'}(t)\rangle\langle u^H_{b\mathbf{k}'}(t)|\rho_{\mathbf{k}'}(t)\right] \\ &= \langle u^H_{b,\mathbf{k}-e\mathbf{A}(t)}(t)|\rho_{\mathbf{k}-e\mathbf{A}(t)}(t)|u^H_{b,\mathbf{k}-e\mathbf{A}(t)}(t)\rangle, \end{aligned} \tag{5.6}$$

where $\mathbf{K}'(t)$ is the accelerated wavevector in accordance with the acceleration theorem, $\mathbf{K}'(t) = \mathbf{k}' + e\mathbf{A}(t)$. The population distribution in the nonequilibrium steady state can be evaluated in the long-time propagation limit under a static field $\mathbf{A}(t) = -\mathbf{E}_{dc}t$,

$$n^{\mathrm{neq-steady}}_{b\mathbf{k}} = \lim_{t\to\infty} n_{b\mathbf{k}}(t). \tag{5.7}$$

In Fig.5.8(a), we illustrate the population distribution in the conduction band for the nonequilibrium steady-state under a static field with a strength of $E_{dc} =$

0.5 MV/cm. The static field is set along the Γ–M direction (x-axis), and the blue circle marks the Dirac point (K point).

In this illustrateion, the region to the left of the Dirac point is predominantly occupied by the field-induced population in the nonequilibrium steady-state, while the region to the right of the Dirac point appears nearly empty. This asymmetry disrupts the inversion symmetry of the system. We use this nonequilibrium population distribution as the reference distribution of the relaxation operator in Eq. (2.36) instead of the Fermi–Dirac distribution to establish the nonequilibrium population model.

In Fig.5.8(b), we present the angular dependence of the second-harmonic under a static field with a strength of $E_{dc} = 0.5$MV/cm. The corresponding angular dependences of the third, fourth, and fifth harmonics are showned in Figs.5.8(c–e), respectively. Each panel displays results obtained using the nonequilibrium population model as the blue solid line, compared with results derived from the quasi-static approximation, showned as the green solid line, which matches the result shown in Fig.5.5.

Figs 5.8 (b) and (d) highlight that even-order harmonics computed with the nonequilibrium population model are notably weaker compared to those calculated using the fully dynamical approach based on the quasi-static approximation. This difference indicates that under the charge-neutral condition ($\mu = 0$) examined here, the resonant effects of the MIR field at two- and four-photon resonances are significantly distant from the Fermi level. Consequently, modifications to the population near the Fermi surface minor contributions to even-order harmonic generation. In contrast, the fully dynamical calculation reveals that the THz field can coherently couple with the MIR field via off-diagonal elements of the density matrix, enabling coherent coupling not only around the Fermi level but also across the Brillouin zone wherever dipole transitions are permitted. Thus, the coherent coupling component may strengthen even-order harmonic generation by enhancing contributions from resonant quantum pathways.

Fig.5.8(c) demonstrates that the third-harmonic computed using the fully dynamical model is 1.57 times stronger than that obtained using the nonequilibrium population model when the fields are perpendicular. This result suggests that the

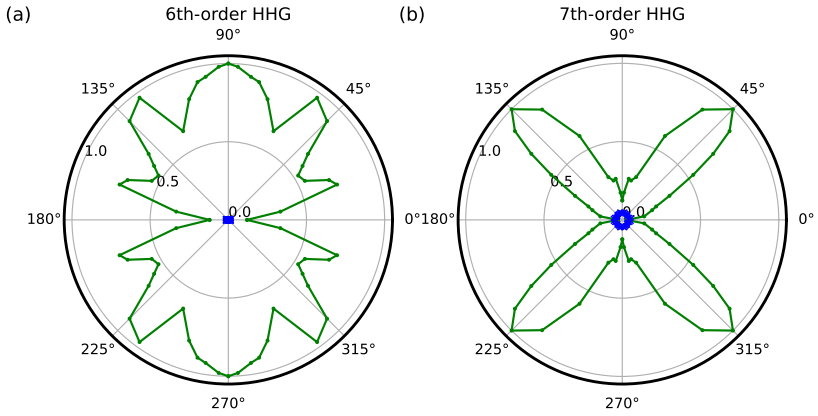

Figure 5.9: The angular dependence of the emitted harmonic intensity for the (a) sixth and (b) seventh harmonics are shown. The results obtained using the nonequilibrium population model and the nonequilibrium steady-state are shown by the blue and green solid lines, respectively. Figure is reproduced with permission from ref. ([122]). Copyright 2024, Phys. Rev. B.

THz field enhances third-harmonic generation for the perpendicular configuration, with both coherent coupling and incoherent population playing crucial roles in this THz-assisted enhancement mechanism. On the other hand, when the fields are parallel, the third-harmonic calculated using the fully dynamical approach is 0.57 times weaker than that computed using the nonequilibrium population model. This finding indicates that contributions from coherent coupling and incoherent population act against each other, subsidingthe overall signal. Thus, both coherent coupling and incoherent population influence third-harmonic generation depending on the relative angle θ between the THz and MIR fields.

In Fig.5.8(e), we observe that the fifth-order harmonic computed using the fully dynamical model is significantly higher than that obtained using the nonequilibrium population model, except when the MIR and THz fields are parallel. This observation suggests that coherent coupling predominantly contributes to the enhancement of fifth-harmonic generation for most angles, although both coherent coupling and incoherent population effects are relevant when the fields are parallel. These consistent results are similarly observed for higher-order harmonics in Figure. (5.9):

We contrasted the outcomes for the sixth and seventh harmonics utilizing both the nonequilibrium population model and the nonequilibrium steady state. In Figures 5.9 (a) and (b), we illustrate the angular dependency of the sixth- and

seventh-harmonic yields under a static field strength of $E_{dc} = 0.5$MV/cm, respectively. In agreement with the analysis depicted in Fig.5.8, the coherent interaction between the MIR and THz fields significantly enhances the high harmonic generation (HHG), surpassing mere field-induced population effects. In summary, when only a MIR field is applied to graphene, the induced HHG is attributed to interference between multiple excitation pathways involving nonlinear coupling between MIR-induced intraband and interband transitions. On the other hand, the substantial enhancement of HHG observed in the presence of THz fields indicates the activation of an additional nonlinear coupling mechanism. This mechanism arises from coherent coupling between MIR- and THz-induced transitions, suggesting its predominance over other processes in contributing to overall harmonic .

The comparison between the results obtained using the fully dynamical calculation and the nonequilibrium population distribution model has provided valuable insights into the roles of coherent coupling between the MIR and THz fields. The dominance of coherent coupling in generating THz-induced even-order harmonics and enhancing high-order harmonics suggests its crucial role in driving nonlinear optical processes in solids. On the other hand, the enhancement of third harmonics under a THz field is influenced by both coherent coupling and the nonequilibrium population. Furthermore, coherent coupling appears to predominantly contribute to the enhancement of higher-order harmonics.

Importantly, these enhancement mechanisms are not limited to specific laser parameters but can be realized under more general conditions. Therefore, effective control of both coherent coupling and population dynamics becomes essential for increasing HHG from solids using multicolor laser fields.

Furthermore, the significance of coherent coupling extends across various orders of harmonic generation, as evidenced by the coherent coupling mechanism's influence on low-order harmonic phenomena (see Fig. 5.8). This highlights the research necessity of field-induced coherence in nonlinear optical effects more broadly. Consequently, these findings hint at the potential for efficiently controlling electron and spin dynamics through coherent coupling, adding multi-color lasers. Such capabilities would exceed mere frequency conversion of light, opening ways for the advancement of ultrafast optoelectronics and optospintronics.

This page is intentionally left blank.

Chapter 6

CONCLUSION AND OUTLOOK

This thesis offers a comprehensive examination of nonlinear optical phenomena, focusing on the injection of photocarriers and the generation of high-order harmonics, in 2D systems all analyzed through the lens of microscopic electron dynamics. It begins by establishing the theoretical groundwork for understanding time-dependent quantum dynamics induced by light in solid systems, encompassing the light and matter interactions. We emphasize the theoretical nonequilibrium framework by presented tight-binding approach in this thesis for analyzing nonlinear optical phenomena in materials, particularly in microscopic details and conducting dissipative non-equilibrium analyses. By synthesizing these discoveries, the thesis contributes to the advancement of our comprehension of nonlinear optical phenomena in 2D materials, highlighting the importance of nonequilibrium quantum dynamics in modeling complex behaviors:

Chapter (2) introduces the tight-binding model, illustrating its application to typical hexagonal lattice nanostructures in 2D materials. The theoretical framework of the time-dependent Schrödinger equation (TDSE) and quantum master equation are introduced for simulating dynamical evolution. Through theoretical exploration, the thesis investigates the injection of dc-current and the emergence of population imbalances under two-color linearly polarized laser fields with frequencies ω and 2ω.

In Chapter (3), the focus shifts to the light-induced electron dynamics in a prototypical two-dimensional insulator, h-BN, employing a simplified tight-binding

approximation within a perturbative resonant regime. Surprisingly, even under deeply off-resonant conditions, the thesis reveals the induction of ballistic current by two-color linearly polarized light, showing a possibility for efficient electron population control without necessitating elliptical light polarization.

Chapter (4) delves into the mechanism of THz-induced high-order harmonic generation (HHG) and nonlinear electric transport in graphene. Utilizing the quantum master equation with the relaxation time approximation, the thesis provides a comprehensive understanding of these phenomena. Emphasis is placed on the pivotal role of nonequilibrium electron dynamics in conductivity reduction and the prevention of interband excitation.

In Chapter (5), the thesis explores strategies to enhance or suppress the efficiency of solid-state HHG, aiming to advance innovative HHG-based light sources and spectroscopies. Employing the quantum master equation, electron dynamics under both mid-infrared (MIR) and THz fields are analyzed, revealing the central role of coupling-induced coherence in enhancing MIR-induced HHG. This sheds light on the significance of field-induced coherence, transcending traditional population effects, and paving the way for future advancements in quantum dynamics and optoelectronic applications.

Based on our discussion, we demonstrate that the tight-binding model is a valid approach with computational efficiency in studying electronic and nonlinear optical response properties of materials. While it provides a simple and intuitive description of electronic band structures, its accuracy may be limited due to its semi-empirical nature and reliance on fitting parameters. However, ab initio Density Functional Theory (DFT) serves as a foundation for improving the tight-binding model. By approximating first principles models derived from DFT, the tight-binding model benefits from the accuracy of DFT while achieving computational efficiency through reduced Hilbert space size. This approximation acknowledges the underlying first principles modeling and maintains close ties to exact results, enhancing its applicability in predicting electronic properties of materials.

The tight-binding model introduced in this thesis only considering the basic nearest hopping and only two bands (one valence band and one conduction

band), which can be expanded to more onsite interactions like next-nearest hopping and even more bands. Tight-binding model allows for the inclusion of various physical effects such as electron-electron interactions, electron-phonon interactions, and external fields. This flexibility enables researchers to tailor the model to specific material systems or phenomena of interest, making it suitable for studying a wide range of materials, including complex structures and heterostructures.

The tight-binding model also provides valuable insights into the microscopic electronic structure of materials, facilitating a deeper understanding of their behavior. By explicitly considering atomic interactions within a material, the model offers a more interpretable description of electronic properties, making it easier to identify the underlying physical mechanisms governing electronic and optical phenomena. This interpretability enhances the model's utility in guiding experimental studies and device design, enabling researchers to make informed decisions based on fundamental principles.

As we mentioned in Section. (2.2), Wannierization acts as a vital link between Density Functional Theory (DFT) and tight-binding models. By transforming delocalized Bloch states from DFT calculations into localized Wannier functions, it simplifies the electronic structure representation while retaining accuracy. These Wannier functions parameterize the hopping integrals and on-site potentials in tight-binding models, reducing computational complexity while preserving essential physics. This integration facilitates seamless transitions from first principles calculations to computationally efficient models, enabling deeper insights into material properties and enhancing connections between theory and experiment.

Overall, our work advances the theoretical framework for studying nonlinear optics in 2D materials and provides guidance for future experimental studies and device design by solving quantum dynamics based on tight-binding model, which holds promising prospects for advancing nonlinear optical technology and ultrafast techniques, offering practical applications and avenues for further exploration:

- While we introduce the topological phase and Berry curvature in Chap-

ter. (2) for 2D topological insulators, we also expand Houston states into dynamicl phase and geometric phase under adibiatic approximation, we did not go further for the time-dependent perturbation analysis by considering the contribution from geometric phase. The light-induced topological phase transition and the Berry curvature effects can be further studied in the future both analytically and numerically.

- The relaxation approximation we introduced in Chapter. (2) is a simple and effective method to consider the dissipative effects in the quantum master equation. We can further explore the non-Markovian effects in the relaxation approximation to consider the memory effects in the dissipative dynamics. Also, the relaxation time T_1 and T_2 are chosen artificially in the model, we can consider more realistic relaxation time from the experiments or from first principles calculations.

- Exploring new materials: Building upon the comprehensive examination of nonlinear optical phenomena in hexagonal boron nitride and graphene, future research could extend our tight-binding model to bilayer, trilayer systems with stackling discussion; in addition, to other materials such as transition metal dichalcogenides (TMDs) and black phosphorus and also 3D bulks. More validation models can be constructed by Wannierization from DFT as we introduced, we can study the nonlinear optical response on Moiré systems by the construction of continuum models for twisted systems which can be more efficient in computation than TDDFT.

- Integrating external stimuli: Investigating how other stimuli, like cavity or magnetic fields, influence nonlinear optical responses in 2D materials, with a focus on experimental validation to complement theoretical predictions. Quantum Electrodynamics Density Functional Theory (QEDFT) provides a suitable theoretical framework for investigating such processes. QEDFT combines the principles of quantum mechanics and electrodynamics, allowing for the accurate description of the interactions between electrons and electromagnetic fields. The tight-binding model can be integrated with QEDFT to provide a more comprehensive understanding of the system's response to external stimuli.

- Experimental validation: Experimental validation of theoretical predictions is crucial for advancing our understanding of nonlinear optical phenomena in 2D materials. By employing advanced spectroscopic techniques and ultrafast laser spectroscopy, we can directly probe these phenomena under controlled conditions for the validate theoretical predictions in the experiments such as: Transient Absorption Spectroscopy, Second Harmonic Generation (SHG) Spectroscopy, Pump-Probe Spectroscopy like Angle-resolved photoemission spectroscopy (ARPES), and attosecond ultrafast techniques.
- Integrate with Wannierization interface: As we introduced before, with the interface of Wannierization, the tight-binding model can be further improved by incorporating more realistic electronic structures and interactions. This enhancement will enable the model to capture a wider range of physical effects and provide more accurate predictions of material properties by connecting mature ab initio packages like VASP, QE with Wannier90, even allow us to do topological anaylsis by WannierTools. This interface might also help adding dissipation effect for real space real time quantum dynamical evolution simulation in the open system, expexted to be conducted in TDDFT package like OCTOPUS from a reduced Hilbert space.

Through these interconnected research directions, our future work can advance understanding and utilization of nonlinear optical phenomena not only in 2D materials, but also offer unprecedented opportunities for theoretical prediction, innovation, and scientific discovery across various material systems, paving the way for transformative advancements in optoelectronics and beyond, to material science and ultrafast techniques developments.

This page is intentionally left blank.

Appendix A

ADIABATIC BASIS REPRESENTATION

To study the mechanism behinde the nonlinear injection of photocarriers in solids from an analytical perspective, we initially present the equation of motion within the adiabatic basis framework. Within this framework, we can effectively distinguish between intraband and interband transitions, the dynamic phase factor, and the geometric phase factor. To establish this framework, we start by considering the following one-body Schrödinger equation for a k-point same as Eq. (2.21):

$$i\frac{d}{dt}|\psi_{\mathbf{k}}(t)\rangle = H\left[\mathbf{k}+\mathbf{A}(t)\right]|\psi_{\mathbf{k}}(t)\rangle, \tag{A.1}$$

Here, $A(t)$ represents an external vector potential, which correlates with the external electric field as $E(t) = -dA(t)/dt$. Throughout this discussion, we presume that the vector potential remains zero for negative times, i.e., $A(t \leq 0) = 0$.

In the adiabatic basis representation, we define the instantaneous eigenstates of the Hamiltonian:

$$H\left[k+A(t)\right]|u_{b,k+A(t)}\rangle = \epsilon_{b,k+A(t)}|u_{b,k+A(t)}\rangle, \tag{A.2}$$

Here, b denotes the band index. For simplicity, we consider a two-band system comprising the valence band ($b = v$) and the conduction band ($b = c$). Nonethe-

less, this formulation can be straightforwardly extended to encompass general systems.

We can do the following expansion of wavefunction based on the instantaneous eigenstates defined by Eq. (A.2), which following the same expasion of the single-particle orbital in terms of Houston states [85, 86, 128]:

$$|\psi_{\mathbf{k}}(t)\rangle = c_{v,\mathbf{k}}(t)e^{-i\int_0^t dt' \epsilon_{v,\mathbf{k}+\mathbf{A}(t')}} e^{i\phi^g_{v,\mathbf{k}}(t)}|u_{v,\mathbf{k}+\mathbf{A}(t)}\rangle + c_{c,\mathbf{k}}(t)e^{-i\int_0^t dt' \epsilon_{c,\mathbf{k}+\mathbf{A}(t')}} e^{i\phi^g_{c,\mathbf{k}}(t)}|u_{c,\mathbf{k}+\mathbf{A}(t)}\rangle, \tag{A.3}$$

The expansion involves coefficients $c_{b,k}(t)$ for each band. Explicitly, we include the dynamical phase factor $e^{-i\int_0^t dt' \epsilon_{v,k+A(t')}}$ and introduce an additional phase factor $e^{i\phi^g_{b,k}(t)}$ as explained in Section. (3.1). The latter will be defined subsequently as the geometric phase factor following the analytical steps in Ref. ([128]).

Inserting expansion Eq. (A.3) into Eq. (A.1), we have:

$$\begin{aligned}\left[i\frac{d}{dt} - H\left[\mathbf{k}+\mathbf{A}(t)\right]\right]|\psi_{\mathbf{k}}(t)\rangle &= i\dot{c}_{v,\mathbf{k}}(t)e^{-i\int_0^t dt' \epsilon_{v,\mathbf{k}+\mathbf{A}(t')}} e^{i\phi^g_{v,\mathbf{k}}(t)}|u_{v,\mathbf{k}+\mathbf{A}(t)}\rangle \\ &+ i\dot{c}_{c,\mathbf{k}}(t)e^{-i\int_0^t dt' \epsilon_{c,\mathbf{k}+\mathbf{A}(t')}} e^{i\phi^g_{c,\mathbf{k}}(t)}|u_{c,\mathbf{k}+\mathbf{A}(t)}\rangle \\ &- \dot{\phi}^g_{v,\mathbf{k}}(t)c_{v,\mathbf{k}}(t)e^{-i\int_0^t dt' \epsilon_{v,\mathbf{k}+\mathbf{A}(t')}} e^{i\phi^g_{v,\mathbf{k}}(t)}|u_{v,\mathbf{k}+\mathbf{A}(t)}\rangle \\ &- \dot{\phi}^g_{c,\mathbf{k}}(t)c_{c,\mathbf{k}}(t)e^{-i\int_0^t dt' \epsilon_{c,\mathbf{k}+\mathbf{A}(t')}} e^{i\phi^g_{c,\mathbf{k}}(t)}|u_{c,\mathbf{k}+\mathbf{A}(t)}\rangle \\ &- ic_{v,\mathbf{k}}(t)e^{-i\int_0^t dt' \epsilon_{v,\mathbf{k}+\mathbf{A}(t')}} e^{i\phi^g_{v,\mathbf{k}}(t)}\mathbf{E}(t)\cdot\frac{\partial|u_{v,\mathbf{k}+\mathbf{A}(t)}\rangle}{\partial\mathbf{k}} \\ &- ic_{c,\mathbf{k}}(t)e^{-i\int_0^t dt' \epsilon_{c,\mathbf{k}+\mathbf{A}(t')}} e^{i\phi^g_{c,\mathbf{k}}(t)}\mathbf{E}(t)\cdot\frac{\partial|u_{c,\mathbf{k}+\mathbf{A}(t)}\rangle}{\partial\mathbf{k}} = 0.\end{aligned} \tag{A.4}$$

By multiplying $e^{+i\int_0^t dt' \epsilon_{v,\mathbf{k}+\mathbf{A}(t')}} e^{-i\phi^g_{v,\mathbf{k}}(t)}\langle u_{v,\mathbf{k}+\mathbf{A}(t)}|$ to Eq. (A.4), we have:

$$\begin{aligned}&i\dot{c}_{v,\mathbf{k}}(t) - \dot{\phi}^g_{v,\mathbf{k}}(t)c_{v,\mathbf{k}}(t) - ic_{v,\mathbf{k}}(t)\mathbf{E}(t)\cdot\left\langle u_{v,\mathbf{k}+\mathbf{A}(t)}\middle|\frac{\partial u_{v,\mathbf{k}+\mathbf{A}(t)}}{\partial\mathbf{k}}\right\rangle \\ &- ic_{c,\mathbf{k}}(t)e^{-i\int_0^t dt' \epsilon_{c,\mathbf{k}+\mathbf{A}(t')-\epsilon_{v,\mathbf{k}+\mathbf{A}(t')}}} e^{i\left(\phi^g_{c,\mathbf{k}}(t)-\phi^g_{v,\mathbf{k}}(t)\right)}\mathbf{E}(t)\cdot\left\langle u_{v,\mathbf{k}+\mathbf{A}(t)}\middle|\frac{\partial u_{c,\mathbf{k}+\mathbf{A}(t)}}{\partial\mathbf{k}}\right\rangle \qquad \text{(A.5)} \\ &= 0. \qquad \text{(A.6)}\end{aligned}$$

Similarly, by multiplying $e^{+i\int_0^t dt' \epsilon_{c,\mathbf{k}+\mathbf{A}(t')}} e^{-i\phi^g_{c,\mathbf{k}}(t)} \langle u_{c,\mathbf{k}+\mathbf{A}(t)}|$ to Eq. (A.4), we have:

$$
\begin{aligned}
&i\dot{c}_{c,\mathbf{k}}(t) - \dot{\phi}^g_{c,\mathbf{k}}(t) c_{c,\mathbf{k}}(t) - i c_{c,\mathbf{k}}(t)\mathbf{E}(t)\cdot\left\langle u_{c,\mathbf{k}+\mathbf{A}(t)}\middle|\frac{\partial u_{c,\mathbf{k}+\mathbf{A}(t)}}{\partial \mathbf{k}}\right\rangle \\
&- i c_{v,\mathbf{k}}(t) e^{-i\int_0^t dt' \epsilon_{v,\mathbf{k}+\mathbf{A}(t')} - \epsilon_{c,\mathbf{k}+\mathbf{A}(t')}} e^{i\left(\phi^g_{v,\mathbf{k}}(t) - \phi^g_{c,\mathbf{k}}(t)\right)} \mathbf{E}(t)\cdot\left\langle u_{c,\mathbf{k}+\mathbf{A}(t)}\middle|\frac{\partial u_{v,\mathbf{k}+\mathbf{A}(t)}}{\partial \mathbf{k}}\right\rangle = 0.
\end{aligned}
\tag{A.7}
$$

We have the following matrix form for time-dependnt expansion coefficient vector combining Eq. (A.6) and Eq. (A.7):

$$
i\frac{d}{dt}\mathbf{c}_{\mathbf{k}}(t) = \begin{pmatrix} \dot{\phi}^g_{v,\mathbf{k}}(t) & 0 \\ 0 & \dot{\phi}^g_{c,\mathbf{k}}(t) \end{pmatrix} \mathbf{c}_{\mathbf{k}}(t) + i\mathbf{E}(t)\cdot \begin{pmatrix} M_{11} & M_{12} \\ M_{21} & M_{22} \end{pmatrix} \mathbf{c}_{\mathbf{k}}(t), \tag{A.8}
$$

$$
M_{11} = \left\langle u_{v,\mathbf{k}+\mathbf{A}(t)}\middle|\frac{\partial u_{v,\mathbf{k}+\mathbf{A}(t)}}{\partial \mathbf{k}}\right\rangle \tag{A.9}
$$

$$
M_{12} = e^{-i\int_0^t dt' \Delta\epsilon_{cv,\mathbf{k}+\mathbf{A}(t')} + i\Delta\phi^g_{cv,\mathbf{k}}(t)} \left\langle u_{v,\mathbf{k}+\mathbf{A}(t)}\middle|\frac{\partial u_{c,\mathbf{k}+\mathbf{A}(t)}}{\partial \mathbf{k}}\right\rangle \tag{A.10}
$$

$$
M_{21} = e^{-i\int_0^t dt' \Delta\epsilon_{vc,\mathbf{k}+\mathbf{A}(t')} + i\Delta\phi^g_{vc,\mathbf{k}}(t)} \left\langle u_{c,\mathbf{k}+\mathbf{A}(t)}\middle|\frac{\partial u_{v,\mathbf{k}+\mathbf{A}(t)}}{\partial \mathbf{k}}\right\rangle \tag{A.11}
$$

$$
M_{22} = \left\langle u_{v,\mathbf{k}+\mathbf{A}(t)}\middle|\frac{\partial u_{v,\mathbf{k}+\mathbf{A}(t)}}{\partial \mathbf{k}}\right\rangle \tag{A.12}
$$

The coefficient vector was defined as:

$$
\mathbf{c}_{\mathbf{k}}(t) = \begin{pmatrix} c_{v,\mathbf{k}}(t) \\ c_{c,\mathbf{k}}(t) \end{pmatrix}. \tag{A.13}
$$

where $\Delta\epsilon_{bb',\mathbf{k}+\mathbf{A}(t)}$ is defined by the difference of the single particle energies as $\epsilon_{b,\mathbf{k}+\mathbf{A}(t)} - \epsilon_{b',\mathbf{k}+\mathbf{A}(t)}$, and $\Delta\phi^g_{bb',\mathbf{k}}(t)$ is defined by the difference of the geometric phases as $\phi^g_{b,\mathbf{k}}(t) - \phi^g_{b',\mathbf{k}}(t)$.

Here, we define the geometric phases as

$$\begin{aligned}\phi^{g}_{b,\mathbf{k}}(t) &= -i\int_0^t dt'\mathbf{E}(t')\cdot\left\langle u_{b,\mathbf{k}+\mathbf{A}(t')}\middle|\frac{\partial u_{b,\mathbf{k}+\mathbf{A}(t')}}{\partial\mathbf{k}}\right\rangle \\ &= i\int_0^t dt'\frac{dA(t')}{dt'}\cdot\left\langle u_{b,\mathbf{k}+\mathbf{A}(t')}\middle|\frac{\partial u_{b,\mathbf{k}+\mathbf{A}(t')}}{\partial\mathbf{k}}\right\rangle \\ &= i\oint_{\mathbf{A}(0)}^{\mathbf{A}(t)} d\mathbf{A}\cdot\left\langle u_{b,\mathbf{k}+\mathbf{A}}\middle|\frac{\partial u_{b,\mathbf{k}+\mathbf{A}}}{\partial\mathbf{k}}\right\rangle . \end{aligned} \tag{A.14}$$

As observed in the final expression of Eq. (A.14), the phase $\phi^{g}_{b,k}$ only relies on the geometry of the integral path. For simplicity, we presume that contributions from the geometric phases, denoted as $\Delta\phi^{g}_{cv,k}(t)$, are negligible in the perturbation analysis in Section. (3.1). This assumption is valid for the two-band tight-binding model for hexagonal lattices under our discussion in the thesis, which have particle-hole symmetry.

With the expression of the geometric phases in Eq. (A.14), it becomes simplified to rewrite the equation of motion for the coefficient vector as:

$$i\frac{d}{dt}\mathbf{c}_{\mathbf{k}}(t) = \mathcal{H}(t)\mathbf{c}_{\mathbf{k}}(t). \tag{A.15}$$

$$\mathcal{H}(t) = i\mathbf{E}(t)\cdot\begin{pmatrix} 0 & M_{12} \\ M_{21} & 0 \end{pmatrix} \tag{A.16}$$

This equation is essentially the time-dependent Schrödinger equation within the adiabatic basis, closely linked to the Houston basis expansion [85, 86].

Bibliography

1. Franken, e. P., Hill, A. E., Peters, C. e. & Weinreich, G. Generation of optical harmonics. *Physical review letters* **7,** 118 (1961).
2. Brabec, T. & Krausz, F. Intense few-cycle laser fields: Frontiers of nonlinear optics. *Rev. Mod. Phys.* **72,** 545–591. https://link.aps.org/doi/10.1103/RevModPhys.72.545 (2 Apr. 2000).
3. Krausz, F. & Ivanov, M. Attosecond physics. *Rev. Mod. Phys.* **81,** 163–234. https://link.aps.org/doi/10.1103/RevModPhys.81.163 (1 Feb. 2009).
4. Mourou, G. *et al.* Exawatt-Zettawatt pulse generation and applications. *Optics Communications* **285,** 720–724. ISSN: 0030-4018. https://www.sciencedirect.com/science/article/pii/S0030401811012338 (2012).
5. Sipe, J. E. & Shkrebtii, A. I. Second-order optical response in semiconductors. *Phys. Rev. B* **61,** 5337–5352. https://link.aps.org/doi/10.1103/PhysRevB.61.5337 (8 Feb. 2000).
6. Seidel, J. *et al.* Efficient Photovoltaic Current Generation at Ferroelectric Domain Walls. *Phys. Rev. Lett.* **107,** 126805. https://link.aps.org/doi/10.1103/PhysRevLett.107.126805 (12 Sept. 2011).
7. Choi, T., Lee, S., Choi, Y. J., Kiryukhin, V. & Cheong, S.-W. Switchable Ferroelectric Diode and Photovoltaic Effect in BiFeO₃. *Science* **324,** 63–66. https://www.science.org/doi/abs/10.1126/science.1168636 (2009).
8. Yang, S. Y. *et al.* Above-bandgap voltages from ferroelectric photovoltaic devices. *Nature Nanotechnology* **5,** 143–147. ISSN: 1748-3395. https://doi.org/10.1038/nnano.2009.451 (Feb. 2010).
9. Dai, Z. & Rappe, A. M. Recent progress in the theory of bulk photovoltaic effect. *Chemical Physics Reviews* **4,** 011303. ISSN: 2688-4070. https://doi.org/10.1063/5.0101513 (Jan. 2023).
10. Sipe, J. & Shkrebtii, A. Second-order optical response in semiconductors. *Physical Review B* **61,** 5337 (2000).

11. Laman, N., Bieler, M. & Van Driel, H. Ultrafast shift and injection currents observed in wurtzite semiconductors via emitted terahertz radiation. *Journal of applied physics* **98,** 103507 (2005).

12. Laman, N., Shkrebtii, A. I., Sipe, J. E. & van Driel, H. M. Quantum interference control of currents in CdSe with a single optical beam. *Applied Physics Letters* **75,** 2581–2583. ISSN: 0003-6951. https://doi.org/10.1063/1.125084 (Oct. 1999).

13. Laman, N., Bieler, M. & van Driel, H. M. Ultrafast shift and injection currents observed in wurtzite semiconductors via emitted terahertz radiation. *Journal of Applied Physics* **98,** 103507. ISSN: 0021-8979. https://doi.org/10.1063/1.2131191 (Nov. 2005).

14. Schiffrin, A. *et al.* Optical-field-induced current in dielectrics. *Nature* **493,** 70–74. ISSN: 1476-4687. https://doi.org/10.1038/nature11567 (Jan. 2013).

15. Wachter, G. *et al.* Ab Initio Simulation of Electrical Currents Induced by Ultrafast Laser Excitation of Dielectric Materials. *Phys. Rev. Lett.* **113,** 087401. https://link.aps.org/doi/10.1103/PhysRevLett.113.087401 (8 Aug. 2014).

16. Lee, J. D., Yun, W. S. & Park, N. Rectifying the Optical-Field-Induced Current in Dielectrics: Petahertz Diode. *Phys. Rev. Lett.* **116,** 057401. https://link.aps.org/doi/10.1103/PhysRevLett.116.057401 (5 Feb. 2016).

17. Higuchi, T., Heide, C., Ullmann, K., Weber, H. B. & Hommelhoff, P. Light-field-driven currents in graphene. *Nature* **550,** 224–228. ISSN: 1476-4687. https://doi.org/10.1038/nature23900 (Oct. 2017).

18. Heide, C., Boolakee, T., Higuchi, T. & Hommelhoff, P. Sub-cycle temporal evolution of light-induced electron dynamics in hexagonal 2D materials. *Journal of Physics: Photonics* **2,** 024004. https://dx.doi.org/10.1088/2515-7647/ab7d82 (Apr. 2020).

19. Morimoto, Y., Shinohara, Y., Ishikawa, K. L. & Hommelhoff, P. Atomic real-space perspective of light-field-driven currents in graphene. *New Journal of Physics* **24,** 033051. https://dx.doi.org/10.1088/1367-2630/ac5c18 (Mar. 2022).

20. Jiménez-Galán, Á., Silva, R. E. F., Smirnova, O. & Ivanov, M. Lightwave control of topological properties in 2D materials for sub-cycle and non-resonant valley manipulation. *Nature Photonics* **14,** 728–732. ISSN: 1749-4893. https://doi.org/10.1038/s41566-020-00717-3 (Dec. 2020).

21. Mrudul, M. S., Jiménez-Galán, Á., Ivanov, M. & Dixit, G. Light-induced valleytronics in pristine graphene. *Optica* **8,** 422–427. https://opg.optica.org/optica/abstract.cfm?URI=optica-8-3-422 (Mar. 2021).

22. Neufeld, O., Tancogne-Dejean, N., De Giovannini, U., Hübener, H. & Rubio, A. Light-Driven Extremely Nonlinear Bulk Photogalvanic Currents. *Phys. Rev. Lett.* **127,** 126601. https://link.aps.org/doi/10.1103/PhysRevLett.127.126601 (12 Sept. 2021).

23. Gaumnitz, T. *et al.* Streaking of 43-attosecond soft-X-ray pulses generated by a passively CEP-stable mid-infrared driver. *Optics express* **25,** 27506–27518 (2017).

24. McPherson, A. *et al.* Studies of multiphoton production of vacuum-ultraviolet radiation in the rare gases. *J. Opt. Soc. Am. B* **4,** 595–601. https://opg.optica.org/josab/abstract.cfm?URI=josab-4-4-595 (Apr. 1987).

25. Ferray, M. *et al.* Multiple-harmonic conversion of 1064 nm radiation in rare gases. *Journal of Physics B: Atomic, Molecular and Optical Physics* **21,** L31. https://dx.doi.org/10.1088/0953-4075/21/3/001 (Feb. 1988).

26. Krause, J. L., Schafer, K. J. & Kulander, K. C. High-order harmonic generation from atoms and ions in the high intensity regime. *Phys. Rev. Lett.* **68,** 3535–3538. https://link.aps.org/doi/10.1103/PhysRevLett.68.3535 (24 June 1992).

27. Schafer, K. J., Yang, B., DiMauro, L. F. & Kulander, K. C. Above threshold ionization beyond the high harmonic cutoff. *Phys. Rev. Lett.* **70,** 1599–1602. https://link.aps.org/doi/10.1103/PhysRevLett.70.1599 (11 Mar. 1993).

28. Lewenstein, M., Balcou, P., Ivanov, M. Y., L'Huillier, A. & Corkum, P. B. Theory of high-harmonic generation by low-frequency laser fields. *Phys. Rev. A* **49,** 2117–2132. https://link.aps.org/doi/10.1103/PhysRevA.49.2117 (3 Mar. 1994).

29. Baltuška, A. *et al.* Attosecond control of electronic processes by intense light fields. *Nature* **421,** 611–615 (2003).

30. Goulielmakis, E. *et al.* Real-time observation of valence electron motion. *Nature* **466,** 739–743. ISSN: 1476-4687. https://doi.org/10.1038/nature09212 (Aug. 2010).

31. Schultze, M. *et al.* Attosecond band-gap dynamics in silicon. *Science* **346,** 1348–1352. https://www.science.org/doi/abs/10.1126/science.1260311 (2014).

32. Lucchini, M. *et al.* Attosecond dynamical Franz-Keldysh effect in polycrystalline diamond. *Science* **353,** 916–919. https://www.science.org/doi/abs/10.1126/science.aag1268 (2016).

33. Wang, H. *et al.* Attosecond Time-Resolved Autoionization of Argon. *Phys. Rev. Lett.* **105,** 143002. https://link.aps.org/doi/10.1103/PhysRevLett.105.143002 (14 Oct. 2010).

34. Holler, M., Schapper, F., Gallmann, L. & Keller, U. Attosecond Electron Wave-Packet Interference Observed by Transient Absorption. *Phys. Rev. Lett.* **106,** 123601. https://link.aps.org/doi/10.1103/PhysRevLett.106.123601 (12 Mar. 2011).

35. Warrick, E. R., Cao, W., Neumark, D. M. & Leone, S. R. Probing the Dynamics of Rydberg and Valence States of Molecular Nitrogen with Attosecond Transient Absorption Spectroscopy. *The Journal of Physical Chemistry A* **120,** 3165–3174. ISSN: 1089-5639. https://doi.org/10.1021/acs.jpca.5b11570 (May 2016).

36. Reduzzi, M. *et al.* Observation of autoionization dynamics and sub-cycle quantum beating in electronic molecular wave packets. *Journal of Physics B: Atomic, Molecular and Optical Physics* **49,** 065102. https://doi.org/10.1088/0953-4075/49/6/065102 (Feb. 2016).

37. Saito, N. *et al.* Attosecond electronic dynamics of core-excited states of N_2O in the soft x-ray region. *Phys. Rev. Res.* **3,** 043222. https://link.aps.org/doi/10.1103/PhysRevResearch.3.043222 (4 Dec. 2021).

38. Mashiko, H., Oguri, K., Yamaguchi, T., Suda, A. & Gotoh, H. Petahertz optical drive with wide-bandgap semiconductor. *Nature Physics* **12,** 741–745. ISSN: 1745-2481. https://doi.org/10.1038/nphys3711 (Aug. 2016).

39. Siegrist, F. *et al.* Light-wave dynamic control of magnetism. *Nature* **571,** 240–244. ISSN: 1476-4687. https://doi.org/10.1038/s41586-019-1333-x (July 2019).

40. Vampa, G. & Brabec, T. Merge of high harmonic generation from gases and solids and its implications for attosecond science. *Journal of Physics B: Atomic, Molecular and Optical Physics* **50,** 083001 (2017).

41. Ghimire, S. *et al.* Observation of high-order harmonic generation in a bulk crystal. *Nature Physics* **7,** 138–141. ISSN: 1745-2481. https://doi.org/10.1038/nphys1847 (Feb. 2011).

42. Ghimire, S. & Reis, D. A. High-harmonic generation from solids. *Nature Physics* **15,** 10–16. ISSN: 1745-2481. https://doi.org/10.1038/s41567-018-0315-5 (Jan. 2019).

43. Silva, R. E. F., Jiménez-Galán, Á., Amorim, B., Smirnova, O. & Ivanov, M. Topological strong-field physics on sub-laser-cycle timescale. *Nature Photonics* **13,** 849–854. ISSN: 1749-4893. https://doi.org/10.1038/s41566-019-0516-1 (Dec. 2019).

44. Nakagawa, K. *et al.* Size-controlled quantum dots reveal the impact of intraband transitions on high-order harmonic generation in solids. *Nature Physics* **18,** 874–878. ISSN: 1745-2481. https://doi.org/10.1038/s41567-022-01639-3 (Aug. 2022).

45. Gorlach, A. *et al. High harmonic generation driven by quantum light* 2022. arXiv: 2211.03188 [physics.optics].

46. Neufeld, O., Tancogne-Dejean, N., Hübener, H., De Giovannini, U. & Rubio, A. Are There Universal Signatures of Topological Phases in High-Harmonic Generation? Probably Not. *Physical Review X* **13,** 031011 (2023).

47. Corkum, P. B. Plasma perspective on strong field multiphoton ionization. *Physical review letters* **71,** 1994 (1993).

48. Lewenstein, M., Balcou, P., Ivanov, M. Y., L'huillier, A. & Corkum, P. B. Theory of high-harmonic generation by low-frequency laser fields. *Physical Review A* **49,** 2117 (1994).

49. Wu, M., Ghimire, S., Reis, D. A., Schafer, K. J. & Gaarde, M. B. High-harmonic generation from Bloch electrons in solids. *Physical Review A* **91,** 043839 (2015).

50. Wu, M. *et al.* Orientation dependence of temporal and spectral properties of high-order harmonics in solids. *Physical Review A* **96,** 063412 (2017).

51. Plaja, L. & Roso-Franco, L. High-order harmonic generation in a crystalline solid. *Physical Review B* **45,** 8334 (1992).

52. Hawkins, P. G., Ivanov, M. Y. & Yakovlev, V. S. Effect of multiple conduction bands on high-harmonic emission from dielectrics. *Physical Review A* **91,** 013405 (2015).

53. Ndabashimiye, G. *et al.* Solid-state harmonics beyond the atomic limit. *Nature* **534,** 520–523 (2016).

54. Wu, M., Browne, D. A., Schafer, K. J. & Gaarde, M. B. Multilevel perspective on high-order harmonic generation in solids. *Physical Review A* **94,** 063403 (2016).

55. Guan, Z., Zhou, X.-X. & Bian, X.-B. High-order-harmonic generation from periodic potentials driven by few-cycle laser pulses. *Physical Review A* **93,** 033852 (2016).

56. Jin, J.-Z. *et al.* High-order harmonic generation from a two-dimensional band structure. *Physical Review A* **97,** 043420 (2018).

57. Du, T.-Y., Huang, X.-H. & Bian, X.-B. High-order-harmonic generation from solids: The contributions of the Bloch wave packets moving at the group and phase velocities. *Physical Review A* **97,** 013403 (2018).

58. Hohenleutner, M. *et al.* Real-time observation of interfering crystal electrons in high-harmonic generation. *Nature* **523,** 572–575 (2015).

59. Schubert, O. *et al.* Sub-cycle control of terahertz high-harmonic generation by dynamical Bloch oscillations. *Nature photonics* **8,** 119–123 (2014).

60. Langer, F. *et al.* Lightwave-driven quasiparticle collisions on a subcycle timescale. *Nature* **533,** 225–229 (2016).

61. Vampa, G. *et al.* Theoretical analysis of high-harmonic generation in solids. *Physical review letters* **113,** 073901 (2014).

62. McDonald, C., Amin, K., Aalmalki, S. & Brabec, T. Enhancing high harmonic output in solids through quantum confinement. *Physical Review Letters* **119,** 183902 (2017).

63. Yu, C. *et al.* Two-dimensional imaging of energy bands from crystal orientation dependent higher-order harmonic spectra in h- BN. *Physical Review B* **98,** 085439 (2018).

64. Luu, T. T. & Wörner, H. J. High-order harmonic generation in solids: A unifying approach. *Physical Review B* **94,** 115164 (2016).

65. Golde, D., Meier, T. & Koch, S. W. High harmonics generated in semiconductor nanostructures by the coupled dynamics of optical inter-and intraband excitations. *Physical Review B* **77,** 075330 (2008).

66. Jiang, S. *et al.* Role of the transition dipole amplitude and phase on the generation of odd and even high-order harmonics in crystals. *Physical review letters* **120,** 253201 (2018).

67. Vampa, G., McDonald, C., Orlando, G., Corkum, P. & Brabec, T. Semiclassical analysis of high harmonic generation in bulk crystals. *Physical Review B* **91,** 064302 (2015).

68. Tamaya, T., Ishikawa, A., Ogawa, T. & Tanaka, K. Diabatic mechanisms of higher-order harmonic generation in solid-state materials under high-intensity electric fields. *Physical review letters* **116,** 016601 (2016).

69. Tancogne-Dejean, N., Mücke, O. D., Kärtner, F. X. & Rubio, A. Impact of the electronic band structure in high-harmonic generation spectra of solids. *Physical review letters* **118,** 087403 (2017).

70. Tancogne-Dejean, N., Sentef, M. A. & Rubio, A. Ultrafast modification of Hubbard U in a strongly correlated material: ab initio high-harmonic generation in NiO. *Physical review letters* **121,** 097402 (2018).

71. Tancogne-Dejean, N., Mücke, O. D., Kärtner, F. X. & Rubio, A. Ellipticity dependence of high-harmonic generation in solids originating from coupled intraband and interband dynamics. *Nature communications* **8,** 745 (2017).

72. Hansen, K. K., Deffge, T. & Bauer, D. High-order harmonic generation in solid slabs beyond the single-active-electron approximation. *Physical Review A* **96,** 053418 (2017).

73. Meng-Xue, G., Chao, L. & Sheng, M. Real-time time dependent density functional theory with numerical atomic orbital basis set: methodology and applications. *Acta Physica Sinica* **67** (2018).

74. Floss, I. *et al.* Ab initio multiscale simulation of high-order harmonic generation in solids. *Physical Review A* **97,** 011401 (2018).

75. Bauer, D. & Hansen, K. K. High-harmonic generation in solids with and without topological edge states. *Physical review letters* **120,** 177401 (2018).

76. Mics, Z. *et al.* Thermodynamic picture of ultrafast charge transport in graphene. *Nature Communications* **6,** 7655. ISSN: 2041-1723. https://doi.org/10.1038/ncomms8655 (July 2015).

77. Kennes, D. M. *et al.* Moiré heterostructures as a condensed-matter quantum simulator. *Nature Physics* **17,** 155–163 (2021).

78. Sarma, S. D., Adam, S., Hwang, E. & Rossi, E. Electronic transport in two-dimensional graphene. *Reviews of modern physics* **83,** 407 (2011).

79. Sławi ńska, J., Zasada, I. & Klusek, Z. Energy gap tuning in graphene on hexagonal boron nitride bilayer system. *Phys. Rev. B* **81,** 155433. https://link.aps.org/doi/10.1103/PhysRevB.81.155433 (15 Apr. 2010).

80. Blase, X., Rubio, A., Louie, S. G. & Cohen, M. L. Quasiparticle band structure of bulk hexagonal boron nitride and related systems. *Phys. Rev. B* **51,** 6868–6875. https://link.aps.org/doi/10.1103/PhysRevB.51.6868 (11 Mar. 1995).

81. Thouless, D. J., Kohmoto, M., Nightingale, M. P. & den Nijs, M. Quantized Hall conductance in a two-dimensional periodic potential. *Physical review letters* **49,** 405 (1982).

82. Berry, M. V. Quantal phase factors accompanying adiabatic changes. *Proceedings of the Royal Society of London. A. Mathematical and Physical Sciences* **392,** 45–57 (1984).

83. Xiao, D., Chang, M.-C. & Niu, Q. Berry phase effects on electronic properties. *Reviews of modern physics* **82,** 1959 (2010).

84. Hofstadter, D. R. Energy levels and wave functions of Bloch electrons in rational and irrational magnetic fields. *Phys. Rev. B* **14,** 2239–2249. https://link.aps.org/doi/10.1103/PhysRevB.14.2239 (6 Sept. 1976).

85. Houston, W. V. Acceleration of Electrons in a Crystal Lattice. *Phys. Rev.* **57,** 184–186. https://link.aps.org/doi/10.1103/PhysRev.57.184 (3 Feb. 1940).

86. Krieger, J. B. & Iafrate, G. J. Time evolution of Bloch electrons in a homogeneous electric field. *Phys. Rev. B* **33,** 5494–5500. https://link.aps.org/doi/10.1103/PhysRevB.33.5494 (8 Apr. 1986).

87. Sato, S. A. *et al.* Light-induced anomalous Hall effect in massless Dirac fermion systems and topological insulators with dissipation. *New Journal of Physics* **21,** 093005. https://doi.org/10.1088/1367-2630/ab3acf (Sept. 2019).

88. Sato, S. A. *et al.* Microscopic theory for the light-induced anomalous Hall effect in graphene. *Phys. Rev. B* **99,** 214302. https://link.aps.org/doi/10.1103/PhysRevB.99.214302 (21 June 2019).

89. Sato, S. A., Hirori, H., Sanari, Y., Kanemitsu, Y. & Rubio, A. High-order harmonic generation in graphene: Nonlinear coupling of intraband and interband transitions. *Phys. Rev. B* **103,** L041408. https://link.aps.org/doi/10.1103/PhysRevB.103.L041408 (4 Jan. 2021).

90. Sato, S. A. & Rubio, A. Nonlinear electric conductivity and THz-induced charge transport in graphene. *New Journal of Physics* **23,** 063047. https://doi.org/10.1088/1367-2630/ac03d0 (June 2021).

91. Meier, T., von Plessen, G., Thomas, P. & Koch, S. W. Coherent Electric-Field Effects in Semiconductors. *Phys. Rev. Lett.* **73,** 902–905. https://link.aps.org/doi/10.1103/PhysRevLett.73.902 (6 Aug. 1994).

92. Sato, S. A. *et al.* Microscopic theory for the light-induced anomalous Hall effect in graphene. *Phys. Rev. B* **99,** 214302. https://link.aps.org/doi/10.1103/PhysRevB.99.214302 (21 June 2019).

93. Dupont, E., Corkum, P. B., Liu, H. C., Buchanan, M. & Wasilewski, Z. R. Phase-Controlled Currents in Semiconductors. *Phys. Rev. Lett.* **74,** 3596–3599. https://link.aps.org/doi/10.1103/PhysRevLett.74.3596 (18 May 1995).

94. Atanasov, R., Haché, A., Hughes, J. L. P., van Driel, H. M. & Sipe, J. E. Coherent Control of Photocurrent Generation in Bulk Semiconductors. *Phys. Rev. Lett.* **76,** 1703–1706. https://link.aps.org/doi/10.1103/PhysRevLett.76.1703 (10 Mar. 1996).

95. Haché, A. *et al.* Observation of Coherently Controlled Photocurrent in Unbiased, Bulk GaAs. *Phys. Rev. Lett.* **78,** 306–309. https://link.aps.org/doi/10.1103/PhysRevLett.78.306 (2 Jan. 1997).

96. Sun, D. *et al.* Coherent Control of Ballistic Photocurrents in Multilayer Epitaxial Graphene Using Quantum Interference. *Nano Letters* **10,** 1293–1296. ISSN: 1530-6984. https://doi.org/10.1021/nl9040737 (Apr. 2010).

97. Muniz, R. A., Salazar, C., Wang, K., Cundiff, S. T. & Sipe, J. E. Quantum interference control of carriers and currents in zinc blende semiconductors based on nonlinear absorption processes. *Phys. Rev. B* **100,** 075202. https://link.aps.org/doi/10.1103/PhysRevB.100.075202 (7 Aug. 2019).

98. Heide, C., Boolakee, T., Eckstein, T. & Hommelhoff, P. *Nanophotonics* **10,** 3701–3707. https://doi.org/10.1515/nanoph-2021-0236 (2021).

99. Wang, K., Muniz, R. A., Sipe, J. E. & Cundiff, S. T. Quantum Interference Control of Photocurrents in Semiconductors by Nonlinear Optical Absorption Processes. *Phys. Rev. Lett.* **123,** 067402. https://link.aps.org/doi/10.1103/PhysRevLett.123.067402 (6 Aug. 2019).

100. Roos, P. A., Quraishi, Q., Cundiff, S. T., Bhat, R. D. & Sipe, J. E. Characterization of quantum interference control of injected currents in LT-GaAs for carrier-envelope phase measurements. *Optics Express* **11,** 2081–2090 (2003).

101. Sato, S. A. & Rubio, A. *Limitations of mean-field approximations in describing shift-current and injection-current in materials* 2023. arXiv: 2310.08875 [cond-mat.mtrl-sci].

102. Sato, S. A. *et al.* Role of intraband transitions in photocarrier generation. *Phys. Rev. B* **98,** 035202. https://link.aps.org/doi/10.1103/PhysRevB.98.035202 (3 July 2018).

103. Galler, A., Rubio, A. & Neufeld, O. *Mapping light-dressed Floquet bands by highly nonlinear optical excitations and valley polarization* 2023. arXiv: 2303.15055 [physics.optics].

104. Tyulnev, I. *et al. Valleytronics in bulk MoS_2 by optical control of parity and time symmetries* 2023. arXiv: 2302.12564 [cond-mat.mtrl-sci].

105. Mao, W., Rubio, A. & Sato, S. A. Terahertz-induced high-order harmonic generation and nonlinear charge transport in graphene. *Physical Review B* **106,** 024313 (2022).

106. Yoshikawa, N., Tamaya, T. & Tanaka, K. High-harmonic generation in graphene enhanced by elliptically polarized light excitation. *Science* **356,** 736–738. https://www.science.org/doi/abs/10.1126/science.aam8861 (2017).

107. Hafez, H. A. *et al.* Nonlinear transmission of an intense terahertz field through monolayer graphene. *AIP Advances* **4,** 117118. https://doi.org/10.1063/1.4902096 (2014).

108. Kovalev, S. *et al.* Electrical tunability of terahertz nonlinearity in graphene. *Science Advances* **7,** eabf9809. https://www.science.org/doi/abs/10.1126/sciadv.abf9809 (2021).

109. Hwang, H. Y. *et al.* Nonlinear THz Conductivity Dynamics in P-Type CVD-Grown Graphene. *The Journal of Physical Chemistry B* **117,** 15819–15824. ISSN: 1520-6106. https://doi.org/10.1021/jp407548a (Dec. 2013).

110. Paul, M. J. *et al.* High-field terahertz response of graphene. *New Journal of Physics* **15,** 085019. https://doi.org/10.1088/1367-2630/15/8/085019 (Aug. 2013).

111. Paul, M. J. *et al.* Terahertz induced transparency in single-layer graphene. *Applied Physics Letters* **105,** 221107. https://doi.org/10.1063/1.4902999 (2014).

112. Hafez, H. A. *et al.* Extremely efficient terahertz high-harmonic generation in graphene by hot Dirac fermions. *Nature* **561,** 507–511. ISSN: 1476-4687. https://doi.org/10.1038/s41586-018-0508-1 (Sept. 2018).

113. Mao, W., Rubio, A. & Sato, S. A. Terahertz-induced high-order harmonic generation and nonlinear charge transport in graphene. *Phys. Rev. B* **106,** 024313. https://link.aps.org/doi/10.1103/PhysRevB.106.024313 (2 July 2022).

114. Mao, W., Rubio, A. & Sato, S. A. Enhancement of high-order harmonic generation in graphene by mid-infrared and terahertz fields. *Physical Review B* **109,** 045421 (2024).

115. Avetissian, H. K., Avetissian, A. K., Avchyan, B. R. & Mkrtchian, G. F. Wave mixing and high harmonic generation at two-color multiphoton excitation in two-dimensional hexagonal nanostructures. *Phys. Rev. B* **100,** 035434. https://link.aps.org/doi/10.1103/PhysRevB.100.035434 (3 July 2019).

116. Avetissian, H. K., Mkrtchian, G. F. & Knorr, A. Efficient high-harmonic generation in graphene with two-color laser field at orthogonal polarization. *Phys. Rev. B* **105,** 195405. https://link.aps.org/doi/10.1103/PhysRevB.105.195405 (19 May 2022).

117. Yoshikawa, N., Tamaya, T. & Tanaka, K. High-harmonic generation in graphene enhanced by elliptically polarized light excitation. *Science* **356,** 736–738. https://www.science.org/doi/abs/10.1126/science.aam8861 (2017).

118. Cha, S. *et al.* Gate-tunable quantum pathways of high harmonic generation in graphene. *Nature Communications* **13,** 6630 (2022).

119. Hafez, H. A. *et al.* Extremely efficient terahertz high-harmonic generation in graphene by hot Dirac fermions. *Nature* **561,** 507–511. ISSN: 1476-4687. https://doi.org/10.1038/s41586-018-0508-1 (Sept. 2018).

120. Kovalev, S. *et al.* Electrical tunability of terahertz nonlinearity in graphene. *Science Advances* **7,** eabf9809. https://www.science.org/doi/abs/10.1126/sciadv.abf9809 (2021).

121. Sato, S. A., Hirori, H., Sanari, Y., Kanemitsu, Y. & Rubio, A. High-order harmonic generation in graphene: Nonlinear coupling of intraband and interband transitions. *Phys. Rev. B* **103,** L041408. https://link.aps.org/doi/10.1103/PhysRevB.103.L041408 (4 Jan. 2021).

122. Mao, W., Rubio, A. & Sato, S. A. Enhancement of high-order harmonic generation in graphene by mid-infrared and terahertz fields. *Phys. Rev. B* **109,** 045421. https://link.aps.org/doi/10.1103/PhysRevB.109.045421 (4 Jan. 2024).

123. Hirori, H., Doi, A., Blanchard, F. & Tanaka, K. Single-cycle terahertz pulses with amplitudes exceeding 1 MV/cm generated by optical rectification in LiNbO3. *Applied Physics Letters* **98,** 091106. ISSN: 0003-6951. https://doi.org/10.1063/1.3560062 (Mar. 2011).

124. Terhune, R. W., Maker, P. D. & Savage, C. M. Optical Harmonic Generation in Calcite. *Phys. Rev. Lett.* **8,** 404–406. https://link.aps.org/doi/10.1103/PhysRevLett.8.404 (10 May 1962).

125. Maker, P. D. & Terhune, R. W. Study of Optical Effects Due to an Induced Polarization Third Order in the Electric Field Strength. *Phys. Rev.* **137,** A801–A818. https://link.aps.org/doi/10.1103/PhysRev.137.A801 (3A Feb. 1965).

126. Nahata, A. & Heinz, T. F. Detection of freely propagating terahertz radiation by use of optical second-harmonic generation. *Opt. Lett.* **23,** 67–69. https://opg.optica.org/ol/abstract.cfm?URI=ol-23-1-67 (Jan. 1998).

127. Cook, D., Chen, J., Morlino, E. & Hochstrasser, R. Terahertz-field-induced second-harmonic generation measurements of liquid dynamics. *Chemical Physics Letters* **309,** 221–228. ISSN: 0009-2614. https://www.sciencedirect.com/science/article/pii/S0009261499006685 (1999).

128. Hirori, H., Sato, S. A. & Kanemitsu, Y. High-Order Harmonic Generation in Solids: The Role of Intraband Transitions in Extreme Nonlinear Optics. *The Journal of Physical Chemistry Letters* **15,** 2184–2192 (2024).